UNIVERSITÀ DEGLI STUDI DI PADOVA

Dipartimento di Fisica e Astronomia "Galileo Galilei"

Corso di Laurea Magistrale in Fisica

Tesi di Laurea

Excitation of Alfvén waves in magnetized plasmas: the reversed-field pinch configuration case

Relatore

Dr. Matteo Zuin

Correlatore

Dr. Daniele Bonfiglio

Laureando

Artur Kryzhanovskyy

Anno Accademico 2017/2018

Thanks to my family's support

Abstract

The nuclear fusion reactions are among the most important processes in the universe, representing the phenomenon that allows the stars to shine and a source of energy potentially inexhaustible for humanity. The attempt to collect the energy obtained from it has led to the study of the confining technique of plasmas called magnetic confinement, which exploits the tendency of charged particles to follow the lines of the magnetic field. In this context the reversed-field pinch (RFP) is one of the possible toroidal configurations, together with the tokamak and the stellarator, for the magnetic confinement of thermonuclear fusion plasmas. The largest experiment in the world based on the RFP configuration is called RFX-mod, and is located in Padua, Italy.

In order to make a fusion reaction in an experimental device like RFX-mod, the reactants (ionized hydrogen isotopes) must be magnetically confined in a high-density high-temperature regime for a sufficiently long time, in order to overcome the Coulomb barrier between them. The magnetic confinement can however be disrupted by magnetic fluctuations within the plasma, called Alfvén waves. They can provide an additional heat transport mechanism resulting in the degradation of the confinement properties of fusion plasmas. Energetic particles, such as alpha particles, can also resonantly destabilise the Alfvén waves, with two negative effects: energy transfer from alpha particles to the Alfvén waves and a loss of alpha particles due to the resulting Alfvénic fluctuations. All of these detrimental effects can compromise the stability of the plasma and its performance. Hence the study of those waves is extremely important for the research field of thermonuclear controlled fusion.

The importance of Alfvén waves is not limited to fusion plasmas, indeed they have been theoretically predicted and studied for the first time in the context of space and solar plasmas. In particular, Alfvén waves are thought to play a fundamental role in the heating of the solar corona, a physical process which is still not fully understood.

The goal of this Thesis is to contribute to the physical understanding of Alfvén waves stimulation, features and dynamics in magnetised fusion plasmas, in particular in the case of the RFP magnetic configuration, by the means of the analysis and interpretation of numerical simulations based on the nonlinear 3D magnetohydrodynamics (MHD) model. The main results of this study are a possible explanation of the physical origin of the experimentally observed Alfvén waves in RFX-mod plasma discharges, and the theoretical identification as Alfvén eigenmodes of the coherent peaks experimentally observed in the power spectrum of the magnetic fluctuations at the plasma edge of RFX-mod.

The investigation presented in this Thesis was carried out through a systematic numer-

ical analysis and theoretical interpretation of different magnetic field and density configurations, with increasing level of complexity. After reviewing the theoretical models, based on the ideal MHD model in cylindrical geometry, for different Alfvénic modes and related phenomena encountered during the analysis, the first analysed configuration (the simplest one) was an equilibrium configuration with uniform axial magnetic field, considered first with an uniform density profile, then with a variable one. The first case was used as a verification ground, since it is the only one for which an exact analytical solution for different Alfvénic modes (namely the shear Alfvén wave, SAW, and compressional Alfvén eigenmodes, CAEs) can be obtained from the theoretical models. Then more complicated cases with non-uniform density, and slightly non-uniform magnetic fields (Tokamak-like configuration), were analysed and theoretically interpreted employing techniques such as the Wentzel–Kramers–Brillouin (WKB) approximation. Compared to the previous case new phenomena were observed, like the phase mixing phenomenon, a damping mechanism for the continuous Alfvén waves, and a coupling between different Alfvén modes. The second step was the analysis of a simplified RFP-like equilibrium configuration of the magnetic fields, first with uniform and then with different variable densities. This case provided a first look at a more realistic representation of Alfvénic activity in an RFP plasma and was used as a bridge to simulations with time-evolving mean magnetic field, analysed afterwards. A new phenomenon was observed in this case, the resonance absorption, which is another damping mechanism for Alfvén waves, specifically for the compressional modes (CAEs) under certain conditions. In addition, a new discrete mode was observed, called the Global Alfvén Eigenmode (GAE). At last a time-dependent mean magnetic field in a realistic RFP dynamical configuration was analysed, with both uniform and variable density profiles. These simulations display a self-consistent MHD dynamics characterised by periodic magnetic reconnection events, a phenomenon also encountered in the real RFX-mod discharges, featuring an abrupt conversion of magnetic energy into kinetic one. Magnetic reconnection events were identified as the fundamental physical phenomenon that excites Alfvén waves in RFP plasmas. Thus, in the end, the realistic simulation case was used for the qualitative comparison and explanation of the experimentally observed Alfvén waves in the RFX-mod device.

This Thesis contains many elements of originality, both in the employed methods and in the achieved results. Concerning methods, the nonlinear approach of the performed numerical analysis (that allows to follow the temporal evolution of Alfvén waves) is rather original since most of the relevant literature uses the linear approach that can only provide the spectrum but not the dynamics of Alfvén waves. Regarding results, for the first time in this Thesis it was shown the importance of compressional modes for the RFP (such modes are usually disregarded because in the tokamak the main role is played by shear Alfvén waves) and the fact that magnetic reconnection can excite Alfvén waves in the RFP. Moreover, the qualitative comparison with respect to experimental measurements in RFX-mod provided a first theoretical interpretation of the experimentally observed coherent modes.

The results obtained in this Thesis and the employed methods form a solid basis for a future more refined modelling study, with the inclusion of kinetic and toroidal effects, of Alfvénic modes in the RFP configuration.

The Thesis is organized as follows:

Part I: Introduction

In *Chapter 1* a definition of magnetized plasmas is given. Then we give a short and intuitive description of Alfvén waves, namely the shear Alfvén wave (SAW) and the compressional Alfvén wave (CAW), and their main features in the context of the ideal MHD model.

In *Chapter 2* the concept of thermonuclear fusion is introduced. The need to confine the fusion reactants, which are in the plasma state due to the high fusion temperature, leads to the study of the magnetic plasma confinement. After a summary about the general properties of the magnetically confined plasmas, we discuss two of the main devices for magnetic confinement, the tokamak configuration, which is the most exploited worldwide, and in deeper details the reversed-field pinch (RFP) configuration, which is another promising configuration and the one investigated in this Thesis.

In *Chapter 3* the main features of the RFX-mod device are introduced. RFX-mod was the first experimental device to show and investigate improved confinement RFP states, the so-called QSH states, for which a brief overview is given. Then experimental observations of Alfvén waves in the RFX-mod discharges, characterised by periodic magnetic reconnection events, are presented.

Part II: Theoretical models and numerical tools

In *Chapter 4* the MagnetoHydroDynamics (MHD) model is described. The MHD model is then used to describe plasma equilibrium state and its stability properties: ideal instabilities and resistive instabilities. Then a brief description of magnetic reconnection is given. In the end we give a rigorous analytical description of Alfvén waves in cartesian geometry, SAW and CAE modes, employing the MHD model in the ideal approximation.

In *Chapter 5* the numerical tool used for solving the MHD model equations will be presented. This numerical tool, called SpeCyl, provided the numerical simulations, of increasing complexity, employed for the analysis of Alfvén waves in different magnetic and density configurations. In particular, we will present the results of a modeling study, based on RFP simulations performed with the SpeCyl code, which shows a systematic repetition of QSH states in between the reconnection events. The same simulations from this study will be used in the final Chapter to characterize the Alfvén waves in the most realistic RFP conditions presently achievable with the SpeCyl code.

Part III: Performed analysis

In *Chapter 6* we will compute the equations of Alfvén waves in cylindrical geometry employing the ideal MHD model. In particular we will consider waves in a straight periodic cylinder with both uniform and non-uniform plasma (with non uniform density and/or magnetic field). The non-uniform case, compared to the uniform one (characterised only by the shear and the compressional modes), will be characterised by a new Alfvén mode, the Global Alfvén Eigenmode (GAE),

and new phenomena like phase mixing and Alfvén resonance absorption. All the theoretical formulas derived in this Chapter will be then used in the following chapters to compute the theoretically expected frequency spectra for the different mean-field configurations, to be compared with numerical spectra from nonlinear MHD simulations.

In *Chapter 7* we list all the analysed configurations, with the respective expected frequency spectra. We considered configurations with increasing complexity: from a purely axial uniform magnetic field, through a non-uniform RFP-like field, up to a "realistic" RFP configuration with time-varying, zero-order magnetic field in the presence of magnetic reconnection events.

In *Chapter 8*, finally, we analyse, one by one, all the nonlinear MHD simulations using the configurations listed in the previous chapter. For each simulation case, the spectrum of Alfvén waves is computed by performing a Fourier analysis in time windows much smaller than the total simulation time. Then, the features of the computed numerical spectrum are discussed, including its temporal evolution, and a physical interpretation based on the expected theoretical spectrum is provided. In the end we make a qualitative comparison of numerical results for the RFP configuration with the experimental observations on the RFX-mod device.

Part IV: Summary and conclusions

In this Part, the results described in the Thesis are summarized and the final conclusions are drawn.

Part V: Appendices

In this final Part some Appendices, which clarify important details and give useful informations not included in the body of the thesis, are found. A relevant bibliography is also provided at the end of this Part.

Prefazione

Le reazioni di fusione nucleare sono tra i processi più importanti dell'universo, rappresentano il fenomeno che consente alle stelle di brillare e una fonte di energia potenzialmente inesauribile per l'umanità. Il tentativo di raccogliere l'energia ottenibile da questi processi ha portato allo studio della tecnica di confinamento dei plasmi chiamata confinamento magnetico, che sfrutta la tendenza delle particelle cariche a seguire le linee del campo magnetico. In questo contesto il reversed-field pinch (RFP) è una delle possibili configurazioni toroidali, insieme al tokamak e allo stellarator, per il confinamento magnetico dei plasmi da fusione termonucleare. Il più grande esperimento al mondo basato sulla configurazione RFP si chiama RFX-mod e si trova a Padova, in Italia.

Per realizzare una reazione di fusione in un dispositivo sperimentale come RFX-mod, i reagenti (isotopi di idrogeno ionizzato) devono essere confinati magneticamente in un regime ad alta temperatura e densità per un tempo sufficientemente lungo, al fine di superare la barriera Coulombiana tra loro. Il confinamento magnetico può tuttavia essere disturbato da fluttuazioni magnetiche all'interno del plasma, chiamate onde di Alfvén. Queste possono fornire un ulteriore meccanismo di trasporto del calore con conseguente degradazione delle proprietà di confinamento dei plasmi da fusione. Le particelle energetiche, come le particelle alfa, possono anche destabilizzare in modo risonante le onde di Alfvén, con due effetti negativi: il trasferimento di energia dalle particelle alfa alle onde di Alfvén e una perdita di particelle alfa dovuta alle risultanti fluttuazioni Alfvéniche. Tutti questi effetti dannosi possono compromettere la stabilità del plasma e le sue prestazioni. Quindi lo studio di queste onde è estremamente importante per il campo di ricerca della fusione termonucleare controllata.

L'importanza delle onde di Alfvén non si limita ai plasmi da fusione, anzi sono stati teoricamente predetti e studiati per la prima volta nel contesto dello spazio e del plasma solare. In particolare, si ritiene che le onde di Alfvén svolgano un ruolo fondamentale nel riscaldamento della corona solare, un processo fisico che non è ancora stato completamente compreso.

L'obiettivo di questa tesi è di contribuire alla comprensione fisica delle stimolazioni, delle caratteristiche e delle dinamiche delle onde di Alfvén nei plasmi magnetizzati da fusione, in particolare nel caso della configurazione magnetica RFP, mediante l'analisi e l'interpretazione di simulazioni numeriche basate sul modello magnetoidrodinamico 3D non lineare. I principali risultati di questo studio sono una possibile spiegazione dell'origine fisica delle onde di Alfvén osservate sperimentalmente nelle scariche di RFX-mod e l'identificazione teorica come autostati Alfvénici dei picchi coerenti osservati

sperimentalmente nello spettro di potenza delle fluttuazioni magnetiche al bordo del plasma del RFX-mod.

Lo studio presentato in questa Tesi è stato condotto attraverso un'analisi numerica sistematica e un'interpretazione teorica di diverse configurazioni di campo magnetico e densità, con un livello crescente di complessità. Dopo aver revisionato i modelli teorici, basati sul modello MHD ideale in geometria cilindrica, per i diversi modi Alfvénici e i fenomeni, ad essi legati, incontrati durante l'analisi, la prima configurazione analizzata (la più semplice) era una configurazione di equilibrio con campo magnetico assiale uniforme, considerato prima con un profilo di densità uniforme, e poi con uno variabile. Il primo caso è stato utilizzato come una verifica, poiché è l'unico per il quale è possibile ottenere una soluzione analitica esatta per i diversi modi Alfvénici (vale a dire la shear Alfvén wave, SAW e gli compressional Alfvén eigenmodes, CAEs) dai modelli teorici. In seguito sono stati analizzati casi più complicati con densità non uniforme e campi magnetici leggermente non uniformi (configurazione stile tokamak), e quindi teoricamente interpretati utilizzando tecniche come l'approssimazione Wentzel-Kramers-Brillouin (WKB). Rispetto al caso precedente sono stati osservati nuovi fenomeni, come il phase mixing, un meccanismo di smorzamento per le shear Alfvén waves, e un accoppiamento tra i diversi modi Alfvénici. Il secondo passo è stato l'analisi di una configurazione di equilibrio semplificata, simile a RFP, dei campi magnetici, dapprima con un profilo di densità uniforme e poi con diversi profili variabili. Questo caso ha fornito un primo sguardo ad una rappresentazione più realistica dell'attività Alfvénica in un plasma RFP e ha fatto da ponte per le simulazioni con il campo magnetico medio che evolve nel tempo, analizzato in seguito. In questo caso è stato osservato un nuovo fenomeno, il resonance absorption, che è un altro meccanismo di smorzamento per le onde di Alfvén, in particolare per i compressional modes (CAEs) in determinate condizioni. Inoltre, è stato osservato un nuovo modo discreto, denominato Global Alfvén Eigenmode (GAE). Alla fine è stato analizzato un campo magnetico medio dipendente dal tempo in una configurazione realistica e dinamica del RFP, dapprima con un profilo di densità uniforme e poi con uno variabile. Queste simulazioni mostrano una dinamica MHD auto-consistente caratterizzata da periodici eventi di riconnessione magnetica, un fenomeno che si verifica anche nelle reali scariche del RFX-mod con una brusca conversione dell'energia magnetica in quella cinetica. Gli eventi di riconnessione magnetica sono stati identificati come il principale fenomeno fisico che eccita le onde di Alfvén nei plasmi RFP. Quindi, alla fine, la simulazione realistica è stata utilizzata per il confronto qualitativo e la spiegazione delle onde di Alfvén osservate sperimentalmente in RFX-mod.

Questa Tesi contiene molti elementi di originalità, sia nei metodi impiegati che nei risultati raggiunti. Per quanto riguarda i metodi, l'approccio non lineare dell'analisi numerica (che consente di seguire l'evoluzione temporale delle onde di Alfvén) è piuttosto originale poiché la maggior parte della letteratura pertinente utilizza l'approccio lineare che può fornire solo lo spettro ma non la dinamica delle onde di Alfvén. Per quanto riguarda i risultati, per la prima volta in questa Tesi è stata mostrata l'importanza dei modi compressional per l'RFP (tali modi sono solitamente ignorati perché nel tokamak il ruolo principale è ricoperto dalle shear Alfvén waves) e il fatto che la riconnessione magnetica può eccitare onde di Alfvén nell'RFP. Inoltre, il confronto qualitativo con le

misure sperimentali in RFX-mod ha fornito una prima interpretazione teorica dei modi coerenti osservati sperimentalmente.

I risultati ottenuti in questa tesi e i metodi impiegati costituiscono una solida base per un futuro studio di modellazione più raffinato, con l'inclusione di effetti cinetici e toroidali, dei modi Alfvénici nella configurazione RFP.

La Tesi è organizzata come segue:

Parte I: Introduzione

Nel *Capitolo 1* viene fornita una definizione di plasma magnetizzato. In seguito diamo una breve descrizione intuitiva delle onde Alfvén, in particolare la shear Alfvén wave (SAW) e la compressional Alfvén wave (CAW), e le loro principali caratteristiche nel contesto del modello MHD ideale.

Nel *Capitolo 2* viene introdotto il concetto di fusione termonucleare. La necessità di confinare i reagenti di fusione, che si trovano nello stato di plasma a causa dell'elevata temperatura, porta allo studio del confinamento magnetico del plasma. Dopo una sintesi sulle proprietà generali dei plasmi magneticamente confinati, discutiamo due dei principali dispositivi per il confinamento magnetico, la configurazione tokamak, che è la più studiata a livello mondiale, e in modo più approfondito la configurazione di reversed-field pinch (RFP), che è un'altra configurazione promettente ed è quella studiata in questa tesi.

Nel *Capitolo 3* vengono introdotte le principali caratteristiche del dispositivo RFX-mod. RFX-mod è stato il primo dispositivo sperimentale a mostrare e ad investigare stati di confinamento migliorati nell'RFP, i cosiddetti stati QSH, per i quali viene fornita una breve panoramica. Vengono quindi presentate osservazioni sperimentali delle onde di Alfvén nelle scariche di RFX-mod, caratterizzate da eventi periodici di riconnessione magnetica.

Parte II: Modelli teorici e strumenti numerici

Nel *Capitolo 4* è descritto il modello magnetoidrodinamico (MHD). Il modello MHD viene quindi utilizzato per descrivere lo stato di equilibrio del plasma e le sue proprietà di stabilità: instabilità ideali e instabilità resistive. Quindi viene fornita una breve descrizione della riconnessione magnetica. Alla fine diamo una descrizione analitica rigorosa delle onde di Alfvén nella geometria cartesiana, in particolare dei modi SAW e CAE, impiegando il modello MHD nell'approssimazione ideale.

Nel *Capitolo 5* verrà descritto lo strumento numerico utilizzato per risolvere le equazioni del modello MHD. Questo strumento numerico, chiamato SpeCyl, forniva le simulazioni numeriche, di crescente complessità, impiegate per l'analisi delle onde di Alfvén in diverse configurazioni di campo magnetico e di densità. In particolare, presenteremo i risultati di uno studio di modellazione, basato su simulazioni RFP eseguite con il codice SpeCyl, che mostra una ripetizione sistematica degli stati QSH tra gli eventi di riconnessione. Le stesse simulazioni di questo studio saranno utilizzate nell'ultimo capitolo per caratterizzare le onde di Alfvén nelle condizioni di RFP più realistiche attualmente ottenibili con il codice SpeCyl.

Parte III: Analisi sviluppate

Nel *Capitolo 6* calcoleremo le equazioni delle onde di Alfvén nella geometria cilindrica utilizzando il modello MHD ideale. In particolare considereremo le onde in un cilindro rettilineo periodico con sia plasma uniforme e non uniforme (con densità e/o campo magnetico non uniforme). Il caso non uniforme, rispetto a quello uniforme (caratterizzato solo dalla shear e dalla compressional), sarà caratterizzato da un nuovo modo Alfvénico, il Global Alfvén Eigenmode (GAE), e nuovi fenomeni come il phase mixing e Alfvén resonance absorption. Tutte le formule analitiche derivate in questo capitolo saranno quindi utilizzate nei seguenti capitoli per calcolare gli spettri di frequenza teoricamente attesi per le diverse configurazioni di campo medio, che verrano poi confrontati con gli spettri numerici delle simulazioni MHD non lineari.

Nel *Capitolo 7* vengono elencate tutte le configurazioni analizzate, con i rispettivi spettri di frequenza attesi. Abbiamo considerato configurazioni con di crescente complessità: da un campo magnetico puramente assiale e uniforme, passando per un campo non uniforme simile all'RFP, fino a una configurazione RFP "realistica" con campo magnetico variabile nel tempo e in presenza di eventi di riconnessione magnetica.

Nel *Capitolo 8*, infine, analizziamo, una per una, tutte le simulazioni MHD non lineari utilizzando le configurazioni elencate nel capitolo precedente. Per ogni simulazione, lo spettro delle onde di Alfvén viene calcolato eseguendo un'analisi di Fourier in finestre temporali molto più piccole del tempo totale di simulazione. Quindi, vengono discusse le caratteristiche dello spettro numerico calcolato, inclusa la sua evoluzione temporale, e viene fornita un'interpretazione fisica basata sullo spettro teorico previsto. Alla fine facciamo un confronto qualitativo dei risultati numerici per la configurazione RFP con le osservazioni sperimentali ottenute sul RFX-mod.

Parte IV: Riassunto e conclusioni

In questa Parte, si riassumono i risultati descritti nella Tesi e si traggono le conclusioni finali.

Parte V: Appendici

In questa Parte finale sono state raccolte alcune Appendici, che chiariscono dettagli importanti e forniscono informazioni utili non incluse nel corpo della tesi. Alla fine di questa Parte è inoltre fornita la bibliografia.

Contents

Part I

Introduction

Chapter 1

Magnetized plasmas and Alfvén waves

At the beginning of the 20th century it was discovered that low-frequency electromagnetic waves are able to propagate in conducting fluids, such as plasmas, even though they cannot propagate in rigid conductors. Hannes Alfvén, in 1942, investigated the properties of plasmas, assuming the plasma medium to be a highly conducting, magnetized and incompressible fluid. He found that a distinctive wave mode arises in the fluid, propagating along the magnetic field direction. This wave is now called the shear or torsional Alfvén wave. The existence of this wave, in the conducting fluid mercury, was experimentally verified by Lundquist in 1949. The importance of the waves discovered by Alfvén for space and astrophysical plasmas was soon realized, and the compressible plasma case, which leads to the fast and slow magnetoacoustic waves in addition to the shear Alfvén wave, was treated by Herlofsen in 1950.

The shear Alfvén and magnetoacoustic waves, which are the basic low-frequency wave modes of magnetized plasmas, have been the subject of intense study in the last decades. The main reason for the great interest in these waves is that they play important roles in the heating and energy transport in laboratory, space and astrophysical plasmas. The "Alfvén wave heating" scheme has been investigated theoretically and experimentally as a supplementary heating mechanism of the solar and stellar coronae. Alfvén waves are believed to underlie the transport of magnetic energy in the solar and stellar winds, transfer angular momentum in interstellar molecular clouds during star formation, play roles in magnetic pulsations in the Earth's magnetosphere, and provide scattering mechanisms for the acceleration of cosmic rays in astrophysical shock waves. These and many other applications of these waves may be found in the laboratory, space physics and astrophysics literature.

In realistic physical problems in all plasma environments, shear Alfvén and magnetoacoustic waves propagate in nonuniform plasmas. As a result, the waves may be reflected, transmitted or absorbed. It is also believed that Alfvén's waves provide a means of transport for the internal heat of magnetically confined plasmas. This phenomenon of transport covers an important role in the propagation of heat from the center of the fusion

plasmas to their edges resulting in the degradation of their confinement, and therefore in a loss of fusion alpha particles which are needed to provide the required energy input to keep the plasma in steady state (known as *ignition* condition, see Section 2.2). Energetic particles, such as alpha particles, can also resonantly destabilise the Alfvén waves, with two negative effects: energy transfer from alpha particles to the Alfvén waves and a loss of alpha particles due to the resulting Alfvénic fluctuations. The practical question of the heating to high temperatures of laboratory fusion plasmas that are contained in a vessel, and are therefore necessarily nonuniform, involves such processes. Hence the study of those waves is extremely important for the research field of thermonuclear controlled fusion as it involves a toroidally confined plasma by a powerful magnetic field. This field of research is of strong interest as it is one of the most promising energy sources for the future, since it is intrinsically safe and the reactants are practically unlimited.

In this chapter we give a definition of magnetized plasmas and a very short and intuitive description of Alfvén waves and their main features.

1.1 The concept of plasma

At the temperature values required to trigger fusion reactions, the matter is in the plasma state. A plasma can be defined as an *almost neutral ionized gas that exhibits collective behaviour*.

Plasmas make up 99 % of the observable universe, and can vary in a wide spectrum of density, temperature and size. In plasma physics, density is generally indicated in terms of particles per unit volume (m^{-3}) and temperature, T, in elettronvolt (eV). In particular, in this Thesis, we are interested in magnetized thermonuclear plasma, characterized by density of particles of the order of $n \approx 10^{19} \div 10^{20}$ m^{-3} and temperatures of the order of $T \approx 0.1 \div 10$ keV.

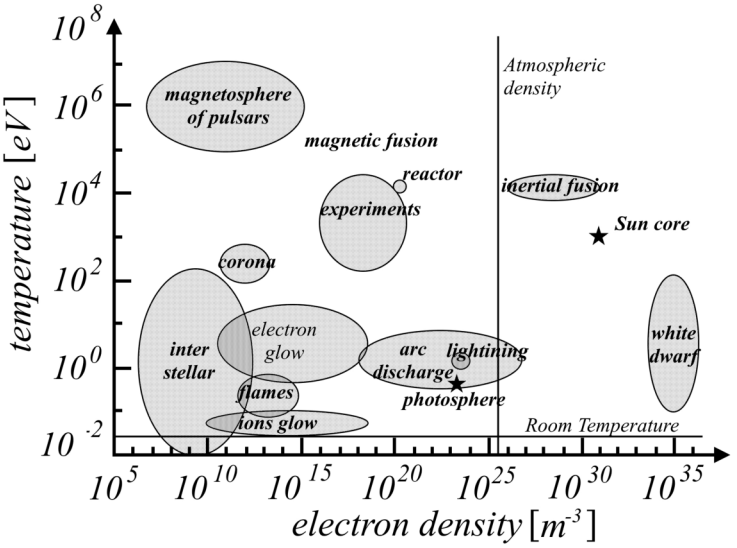

Figure 1.1: Position of various types of plasmas in the temperature-density graph. The conditions necessary for an ionized gas to behave like a plasma are fulfilled in a wide range of parameters.

Plasma dynamics is dominated by a collective behavior, which means that the dynamics of a single charged particle of the plasma depends on long-range interactions with other charged particles, interactions that tend to balance any spatial charge dishomogeneity, resulting in the screening of electrostatic potential. The approximate thickness of such screening effect is represented by the so-called *Debye length* λ_D, which measures the maximum distance where the charge inhomogeneities can take place and is defined as

$$\lambda_D = \sqrt{\frac{\epsilon_0 K T_e}{n_e e^2}}, \tag{1.1}$$

where T_e is the electron temperature and n_e the electron (number) density. On spatial scales larger than Debye's length, plasma is globally neutral, that is, neutral enough so that one can take, over length-scales much larger than λ_D,

$$n_i \simeq n_e \simeq n, \tag{1.2}$$

where n_i is the ion (number) density and n is a common density called the *plasma density*. Anyway, the plasma is not so neutral that all interesting electrostatic effects vanish. Equation 1.2 is the *quasi-neutrality condition*. In addition, any concentrations of positive or negative charges are neutralized in a time scale given by the inverse of plasma frequency:

$$\omega_p = \sqrt{\frac{n_e e^2}{m_e \epsilon_0}}. \tag{1.3}$$

The typical size of Debye length λ_D for plasmas used to study the fusion phenomenon varies from micrometer to millimeter, while plasma frequency ω_p ranges from gigahertz to terahertz. The study of phenomena occurring on longer time scales than the inverse of plasma frequency and spatial scales larger than Debye length, which is the case for typical fusion plasmas, therefore allows to treat the plasma as a neutral fluid, as for example in the ideal magnetohydrodynamic model (MHD) that will be described in the next chapters.

1.2 Alfvén waves

Any wave in nature is driven by some restoring force which opposes displacements in the system. In the context of the MHD model (whose equations will be discussed in Chapter 4), two types of restoring forces are possible: one arising out of magnetic stresses; and the other arising out of pressure gradients. The ideal MHD theory can therefore support two basic types of magnetohydrodynamic waves, the Alfvén waves, called *Torsional Alfvén Wave* or *Shear Alfvén Wave* (SAW) and *Compressional Alfvén Wave* (CAW), also called *magnetoacoustic* or *magnetosonic* waves. The magnetoacoustic mode can be further split up into two distinct modes, the *fast* and *slow* magnetoacoustic waves. Below we give a short and intuitive description of Alfvén's shear and compressional waves features.

1.2.1 Shear Alfvén Wave

The MHD fluid undergoes a magnetic tension B^2/μ_0 along the field lines and an isotropic pressure $B^2/2\mu_0$. The magnetic field lines therefore act as strings under tension connected to masses (plasma particles are constrained to the field lines in ideal MHD, as we discuss in Appendix A). Whenever the magnetic field lines are distorted by a transverse perturbation, the magnetic tension tries to oppose the distortion. Just as a transverse wave can be started in a string by plucking it, similarly we have the transverse Alfvén wave moving along the field lines. The velocity of the transverse oscillations moving along a stretched string can be shown to be

$$v_A = \left(\frac{tension}{density}\right)^{1/2} = \left(\frac{B^2}{\mu_0 \rho}\right)^{1/2}. \tag{1.4}$$

This is the *Alfvén's velocity*. Figure 1.2(a) illustrates the transverse nature of fluid motion and the frozen magnetic field lines. There aren't density or pressure fluctuations associated with this wave, the magnetic tension being the only restoring force for it. Because of this characteristics this wave is called "torsional" or "shear" Alfvén's wave.

1.2.2 Compressional Alfvén Wave

By extending the analogy, we expect to observe longitudinal oscillations due to pressure fluctuations. Those are called "magnetoacoustic", or "magnetosonic" or more simply "compressional" waves involving compressions and rarefactions of the plasma and magnetic field lines. Such a wave propagates with a speed v_M so to satisfy the relation

$$\nabla\left(p + \frac{B^2}{2\mu_0}\right) = v_M^2 \nabla\rho, \tag{1.5}$$

which implies

$$v_M^2 = \frac{\mathrm{d}}{\mathrm{d}\rho}\left(p + \frac{B^2}{2\mu_0}\right)_{\rho_0} = c_S^2 + \frac{\mathrm{d}}{\mathrm{d}\rho}\left(\frac{B^2}{2\mu_0}\right)_{\rho_0}, \tag{1.6}$$

where $c_S^2 = \gamma p_0/\rho_0$ is the sound speed and p_0, ρ_0 are respectively the pressure and density of the unperturbed plasma. Note that we have included the magnetic pressure in the restoring force. Because the particles are constrained to the field lines, we have $B/\rho = B_0/\rho_0$ and therefore

$$v_M^2 = c_S^2 + \frac{\mathrm{d}}{\mathrm{d}\rho}\left(\frac{B_0^2\rho^2}{2\mu_0\rho_0^2}\right)_{\rho_0} = c_S^2 + v_A^2, \tag{1.7}$$

where v_A is Alfvén's speed defined above and B_0 is a uniform magnetic field. The nature of a magnetoacoustic wave is illustrated in Figure 1.2(b). This wave is a mixture of acoustic and magnetic waves, where both types of restoring forces are present. Furthermore it can be split up into two distinct modes, the fast and slow magnetoacoustic waves. For the first one of these modes, the pressure and magnetic restoring forces are roughly in phase, making the mode propagate fast, so it was called the fast mode. The other mode, for

which these restoring forces are roughly out of phase, is known as the slow mode. Any arbitrary disturbance in our system, described by ideal MHD theory, can be represented as a superposition of the Alfvén, fast and slow modes.

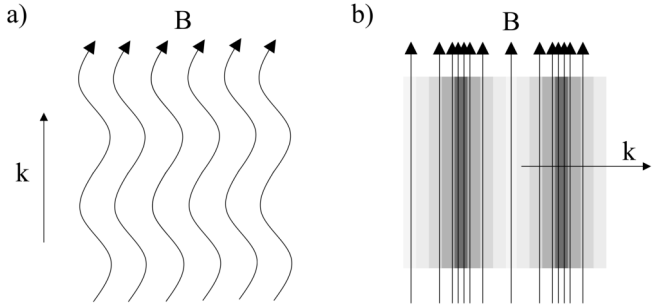

Figure 1.2: a) Shear Alfvén Wave. b) Compressional Alfvén Wave.

Chapter 2

Thermonuclear controlled fusion

Thermonuclear controlled fusion is one of the most promising energy source for the future, since it is intrinsically safe and the reactants are practically unlimited. In order to make a fusion reaction, the reactants (ionized hydrogen isotopes) must be confined in a high-density high-temperature regime for a sufficiently long time, in order to overcome the Coulomb barrier between them. In these conditions the burning gas, which is fully ionized due to the high fusion temperature, is found in the plasma state. The plasma can be confined by embedding it in a confining magnetic field. The most advanced device for magnetic plasma confinement is the tokamak, an axis-symmetric toroidal configuration. Other promising configurations are the stellarator and the reversed-field-pinch (RFP).

In this chapter we give a short introduction about thermonuclear controlled fusion, magnetic confinement and toroidal devices such as the tokamak and the RFP.

2.1 The fusion reaction

Nuclear fusion plays an important role in the Universe as it represents the process which powers the stars. The nuclear fusion reaction in the stars consists of a chain of reactions (called *pp-chain*) that from four protons creates an alpha particle, transforming the energy, resulting from mass defect between final products and initials reactants, in photons and kinetic energy of reaction products.

Other chain reactions are used in laboratory situations as the fusion of two protons to form deuterium, the first step of the *pp-chain*, is a process that involves weak interaction, hence characterized by a low cross section and therefore only possible in the stars, where the large amount of hydrogen allows to compensate for the low probability of reaction and to obtain anyway the deuterium needed to allow the faster successive steps.

In choosing alternative reactions to *pp-chain*, the use of light nuclei is mandatory, as well as their easier availability, for two additional reasons: the first is that the Coulombian repulsion, which we must overcome in order to bring the reactant nuclei within the range of the nuclear force, is proportional to the charge product of the nuclei involved, while the latter is due to the fact that when the particles involved have a smaller mass than that of ^{56}Fe (this isotope has the highest binding energy per nucleon, as shown in Figure 2.1),

the sum of the masses of the starting nuclei is higher than the final nuclei, and the mass defect, according to Einstein's equation $E = mc^2$, released as kinetic energy in the reaction products.

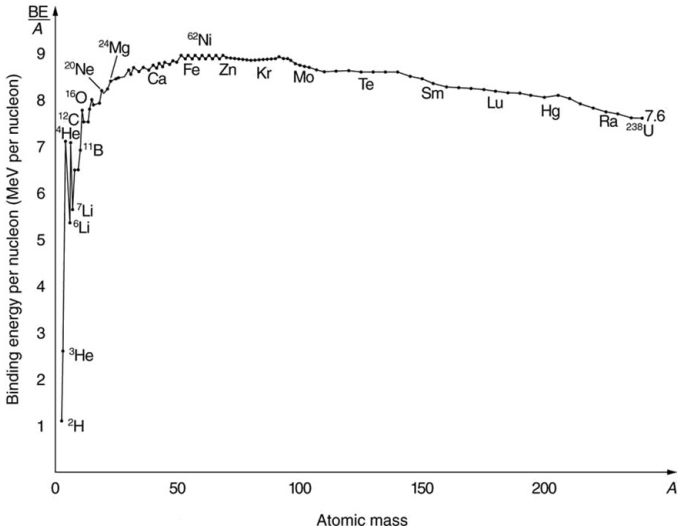

Figure 2.1: Average binding energy per nucleon as a function of atomic mass A.

In choosing the fusion reaction that best suits a laboratory plasma , it is also necessary to consider the trend of cross section with the energy of the reagents and the reaction rates, which impose strict limits on the choice of the energy range in which the reaction will occur.

Combining all these aspects the best candidate for the reaction is that between deuterium and tritium:

$$ {}^{2}_{1}\mathrm{D} + {}^{3}_{1}\mathrm{T} \rightarrow {}^{4}_{2}\mathrm{He}\ (3.5\ \mathrm{Mev}) + {}^{1}_{0}\mathrm{n}\ (14.1\ \mathrm{Mev}) \tag{2.1} $$

characterized by a cross section that at temperatures between 20 and 100 keV, the range in which a hypothetical thermonuclear fusion reactor must operate, is two orders of magnitude greater than that of other possible reactions, as can be seen in Figure 2.2.

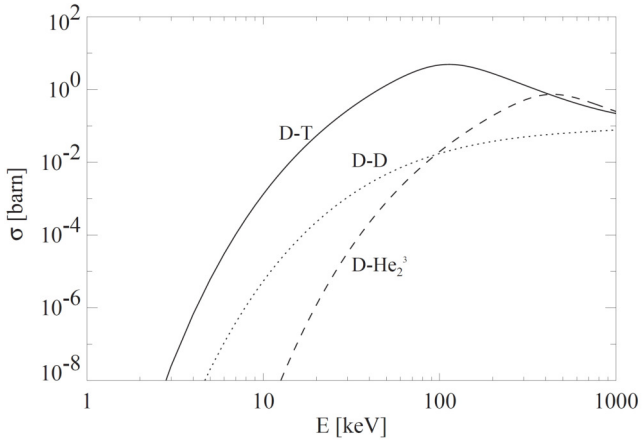

Figure 2.2: Cross section for typical fusion reactions: deuterium-tritium (D-T), deuterium-deuterium (D-D) and deuterium-helium (D-He^3_2). 1 barn = 10^{-24} cm^2.

Nevertheless, the optimal temperature of fusing nuclei is of ~ 10 keV, because the required reactions occur in the high energy tail of the Maxwellian distribution of the heated particles.

Considering the availability of reagents, it should be noted that since tritium is a radioactive element with an average life of about 12 years, it is not present in nature. It can however be obtained from the following lithium-engaging reaction:

$$ {}^6_3\mathrm{Li} + {}^1_0\mathrm{n} \rightarrow {}^4_2\mathrm{He}\ (2.1\ \mathrm{Mev}) + {}^3_1\mathrm{T}\ (2.7\ \mathrm{Mev}) \tag{2.2} $$

The natural resources needed to obtain energy from the nuclei are potentially inexhaustible since the deuterium can be obtained from ordinary water (about 33g from 1 ton), while current estimates of lithium reserves indicate that they are sufficient to meet the world's energy demand for a time of millions of years.

2.2 Thermonuclear ignition criteria

The aim of nuclear fusion research is to get more energy from the fusion processes than the energy required to trigger one and confine the plasma, having electron and ion density n and temperature T. Confinement of the plasma can never be absolute, as there are various causes of energy loss. The two main ones are given by bremsstrahlung, that is, the emission of radiation by accelerated charged particles and transport losses leading to plasma and energy confinement loss in a characteristic time τ_E.
It is therefore necessary to reinvest, to offset these losses, some of the energy provided by the fusion reactions. In a device that magnetically confines plasma, the alpha particles produced by the reaction (2.1), being charged, may be confined and thus represent the means to transfer part of the fusion energy to the plasma, the remaining part being stored in the neutrons, which cannot be confined and coming out of the confinement chamber are going to feed some system that converts heat into electricity. We can summarize this with the relation:

$$ \frac{\partial W}{\partial t} = P_{heat} + P_\alpha - P_{loss}, \tag{2.3} $$

where W is the plasma energy density, P_{heat} is the external heating power, P_{loss} the power losses and P_α the power given by the alpha particles.

The ignition criteria formalizes the energy balance in the situation where the reactor is self-sustaining thanks to the sole power supplied by alpha particles, providing a condition that links density n and confinement time τ_E of the energy of plasma for a given temperature T, given by:

$$ n\tau_E > 1.5 \cdot 10^{20}\,\mathrm{m^{-3}s}. \tag{2.4} $$

In Figure 2.3 a plot of the minimum value of the product $n\tau_E$ required to obtain ignition is shown as a function of the temperature T: this function exhibits a minimum at a value close to 20 keV.

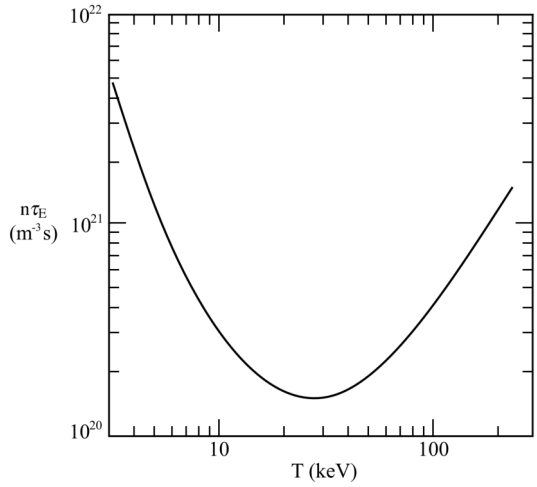

Figure 2.3: The minimum value of $n\tau_E$ required to obtain ignition, as a function of temperature.

A different more compact expression to define fusion conditions is the use of the so-called *fusion triple product*:

$$nT\tau_E > 3 \cdot 10^{21}\,\mathrm{m}^{-3}\mathrm{keVs}. \tag{2.5}$$

The previous condition does not allow complete freedom in the choice of parameter values. In particular, the presence of a material wall that cannot withstand too high power densities places a limit on the density of plasma, with $n \sim 10^{20}\,\mathrm{m}^{-3}$. The typical plasma temperature in a experiment, as seen in Figure 2.3 , need to have a value $T \sim 20\,\mathrm{keV}$, leading to confinement time of energy, the most critical parameter, to be $\tau \sim 1\,\mathrm{s}$.

We have seen that, in order to obtain thermonuclear fusion, the plasma must be kept in a regime of high temperature and high density for a sufficiently long time. This process is called *plasma confinement*. Two schemes of plasma confinement are presently studied:

Inertial Confinement. In this case spherical targets of deuterium and tritium are uniformly irradiated by sharp electromagnetic impulses in order to compress them and obtain conditions of temperature and density leading to a complete burn before thermal equilibrium.

Magnetic Confinement. Plasma is confined through magnetic fields, and heated with ohmic dissipation, radio frequency waves and neutral beams. In the following Sections we give a general introduction of this scheme.

2.3 Magnetic confinement: the toroidal configuration

One of the main confinement techniques is the magnetic one, which originates from the knowledge of the motion characteristics of a charged particle in a magnetic field.
In the presence of a uniform and static magnetic field B, the motion of a particle with

mass m and charge q can be decomposed in a uniform straight motion in the direction parallel to the field and in a uniform circular motion in a perpendicular direction, the latter characterized by a frequency said *cyclotronic frequency* and a radius said *Larmor's radius*, defined as:

$$\omega_c \equiv \frac{q|B|}{m} \qquad\qquad r_L \equiv \frac{v_\perp}{\omega_c} = \frac{mv_\perp}{q|B|}, \tag{2.6}$$

where $v_\perp$ is the velocity of the particle in the direction perpendicular to the magnetic field. For a thermonuclear fusion plasma the value of r_L range from fractions of millimeter for ions to microns for electrons, small compared to the size of the confinement chamber.
The fact that in the direction of the field the motion is straight and uniform, has led to the exclusion of configurations in which the magnetic field lines are not closed and to consider a toroidal type system.
The presence of drift motions due to the curvature and possible disomogeneities of the magnetic field lines in a toroidal configuration makes it more problematic to prevent the plasma from touching the wall of the vacuum chamber; the solution is to create a magnetic field characterized by a helical structure that appropriately compensates for such drift motions.
A torus can be more easily described considering the following frame of reference:

minor radius r which spans the region from the center of the plasma ($r = 0$) to the boundary ($r = a$);

poloidal angle θ which measures the angle on the shorter loop;

toroidal angle ϕ which measures the angle with respect to the toroidal axis, i.e. the longer loop.

The ratio between the major radius R_0 and the minor one a is called aspect ratio. This frame of reference is sketched in Figure 2.4, along with another possible choice, namely the (R, ϕ, Z) frame of reference, involving the radial coordinate R which measures the distance with respect to the toroidal axis and the coordinate Z along the axis itself.

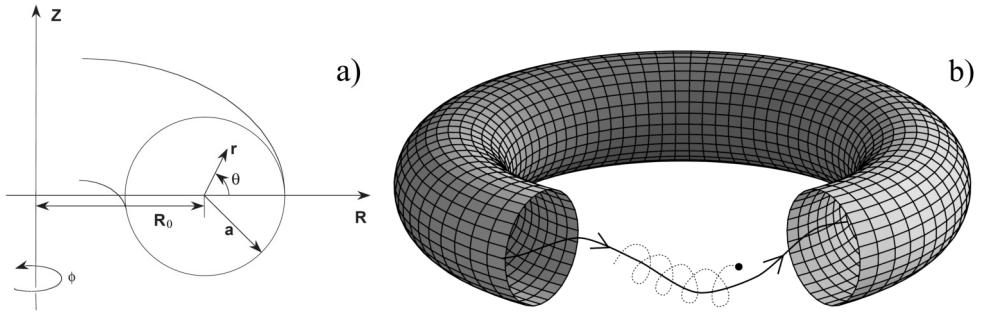

Figure 2.4: a) The toroidal system of reference (r, θ, ϕ) and the cylindrical coordinates (R, ϕ, Z). b) Motion of gyration of a charged particle around a force line of the magnetic field.

In toroidal geometry, a field can be expressed in normal modes as a Fourier expansion over the poloidal and toroidal angles. For instance, the magnetic field B can be written as

$$\mathrm{B}(r,\theta,\phi) = \sum_{m,n} \mathrm{B}_{mn}(r) e^{i(m\theta+n\phi)}, \tag{2.7}$$

where (m,n) is a pair of integer numbers and $\mathrm{B}_{mn}(r)$ is the Fourier component of the normal mode (m,n), whose (geometric) helicity h is hence defined as

$$h \equiv -\frac{n}{m}. \tag{2.8}$$

In particular, the $(0,0)$ Fourier component corresponds to the axis-symmetric part of the field $\mathbf{B}_0$, which does not depend on θ and ϕ:

$$\mathbf{B}_0 \equiv \mathbf{B}^{(0,0)}(r), \tag{2.9}$$

whereas the perturbation to $\mathbf{B}_0$ is referred as $\mathbf{B}_1$.

2.4 The main toroidal devices for magnetic confinement

The main toroidal devices for magnetic confinement of plasma are distinguished by their geometry and by different role of the magnetic field components. There are three different configurations: the stellarator, the tokamak and the reversed field pinch (RFP).

The stellarator belongs to the category of non-axisymmetric toroidal devices. The magnetic field is entirely produced by a complex helical arrangement of the coils around the plasma, designed to obtain a helical magnetic field in equilibrium. This implies that a stellarator configuration does not have a plasma current that would create additional magnetic fields than that generated by the coils.

Tokamak and RFP belong to the category of axisymmetric toroidal devices. The formation of plasma from the gas contained in the toroidal confinement chamber of a device such as tokamak or RFP occurs by inducing a toroidal electric field through the use of a transformer whose primary circuit consists of an iron or an air core and whose secondary is the plasma itself. The electric field thus produced ionizes the atoms of the gas thus becoming capable of supporting a plasma current I_p in the toroidal direction which, by the Ampère's law, produces a poloidal magnetic field. The toroidal component of the magnetic field is generated by an external coil system, in which the current flows in a poloidal direction, forming a solenoid-like device.

The sum of the two magnetic field components thus obtained leads to the formation of a magnetic field with lines helically wrapped on coaxial toroidal surfaces. Figure 2.5 shows a representation of all the external structures needed to create and maintain the plasma.

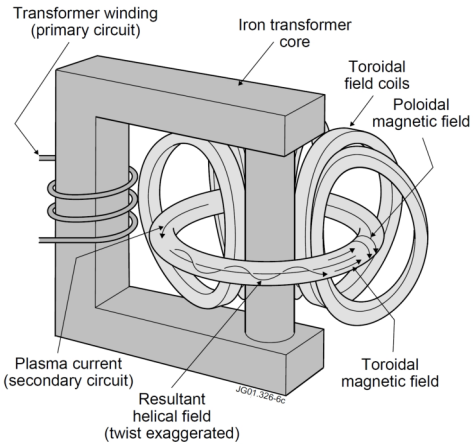

Figure 2.5: Main components of the plasma-forming circuit (transformer) and its confinement (external coils).

2.4.1 Tokamak configuration

In the tokamak the main component of the magnetic field is the toroidal, B_ϕ, generated by a series of external coils. The magnetic field component in the poloidal direction B_θ, created by the plasma current circulating in the torus, is typically one order of magnitude smaller.
An important parameter that regulates plasma dynamics in a device that magnetically confines plasma is the *safety factor*:

$$q(r) \equiv \frac{r}{R_0} \frac{B_\phi(r)}{B_\theta(r)}. \tag{2.10}$$

It can be interpreted as the number of toroidal turns for a single poloidal turn of field line, and in a tokamak, for stability reason, it is always greater than one. This results in a greater intensity of the field toroidal component than the poloidal component, as seen in Figure 2.6, which also schematizes the components of the magnetic field in the RFP configuration, which we discuss in the following section.

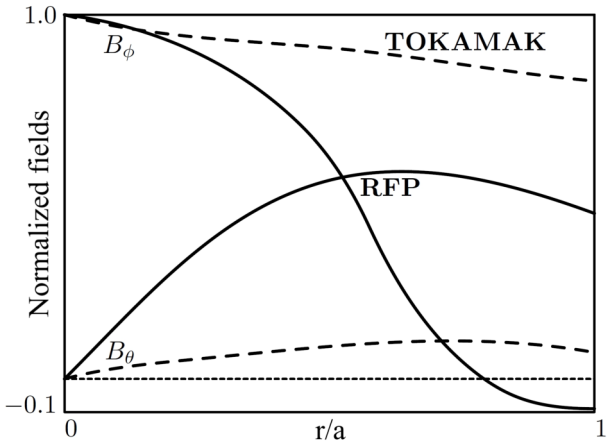

Figure 2.6: Radial profiles of the poloidal and toroidal components of the magnetic field in typical tokamak and RFP configurations. a represents the minor radius of the torus.

2.4.2 RFP configuration

The RFP configuration shares with the tokamak the main features, in particular the axial symmetrical toroidal structure and the fact that the circulating current in the plasma produces a component of the magnetic field further to that generated by the outer coils, which is crucial for plasma confinement.
The characteristics that distinguish the RFP from tokamak are primarily the intensity of the magnetic field generated by the coils external to the plasma, which in a tokamak experiment typically results in an order of magnitude greater than that in a RFP experiment, which also translates into a different energy cost for field creation (the energy associated with a magnetic field is proportional to the square of its intensity).
The two configurations are distinguished by the different ratio between the intensity of the toroidal and poloidal components of the magnetic field: these have on average the same order of magnitude in the RFP, as can be seen in Figure 2.7, unlike the tokamak in which the toroidal component dominates.
The peculiar feature of the RFP is then the reversal of the toroidal magnetic field that in the edge area of the confining chamber assumes a negative value, lesser in absolute value than that present in the axis of the torus. This is a technological advantage with respect to the tokamak, because the outer coils have to produce only the small and reversed magnetic field at the edge, while the field in the central region is mainly generated by currents circulating in the plasma itself. The poloidal component, which compresses and confines the plasma (squeezing "pinch" effect), has a higher value in RFP than tokamak, and is also created by the plasma current I_p circulating in the plasma: the fact that I_p is very high makes it possible to heat the plasma up to high temperatures with only ohmic heating, without the use of additional methods (radiofrequency heating and injection of neutral particles beam) that are required in a tokamak reactor.
From a technological point of view the fact of having to produce with external conductors

a much smaller magnetic field intensity in the RFP promises to overcome problems such as excessive strain on outer coils and the need of superconductor technology and related expensive cooling systems (a tokamak thermonuclear reactor will require magnetic fields greater than 10 T).

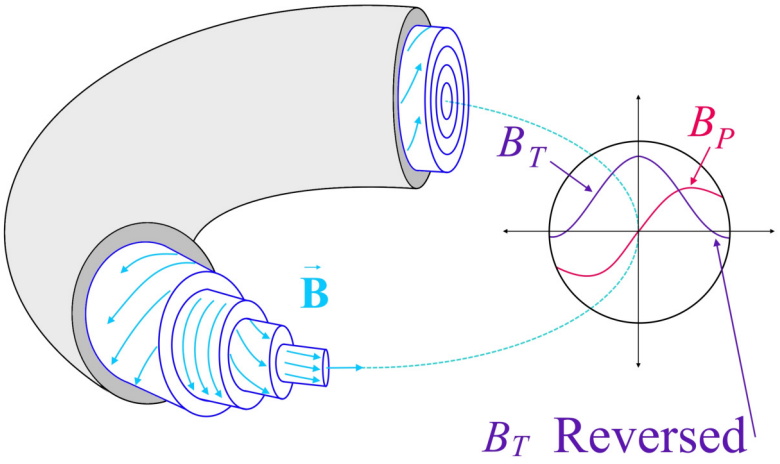

Figure 2.7: Radial profile of the poloidal and toroidal components of the magnetic field in RFP.

Another effect of reversal the toroidal field at the edge of the RFP is on the profile of the safety-factor q, defined in equation (2.10), which is quite different between the two configurations, as can be seen in Figure 2.8.

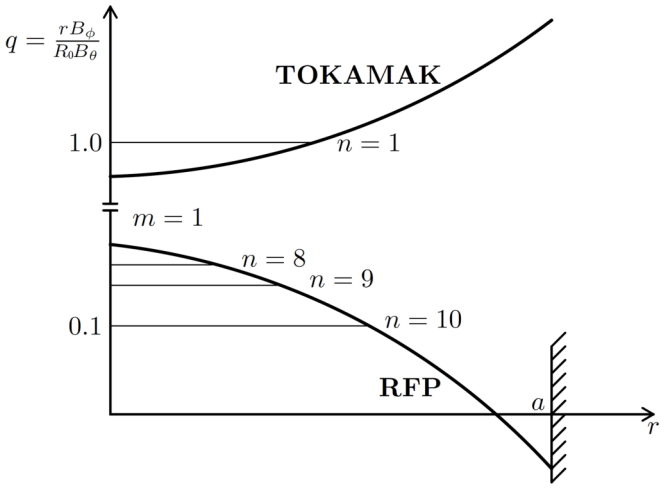

Figure 2.8: Typical radial profiles of the safety factor q for tokamak and the Reversed Field Pinch.

The reversal of the magnetic field is observed beyond a certain value of the *pinch parameter* defined as:

$$\Theta = \frac{B_\theta(a)}{< B_\phi >} = \frac{\mu_0 a I_P}{2\Phi}, \tag{2.11}$$

wherein a, I_P, Φ represent the radius of the plasma column, the plasma current and the toroidal flux of the magnetic field, B_θ and B_ϕ the poloidal and toroidal components of the magnetic field, $< \cdot >$ an average on a section at a fixed toroidal position. The parameter Θ represents substantially the relationship between the plasma current and toroidal flux of the magnetic field, and its typical value in the RFP configuration is greater than one, whereas in the tokamak case, in which the toroidal field is much more intense than the poloidal one, Θ assumes values lower then one.

Another useful parameter to describe how deep the reversal of the field at the edge is in the RFP configuration is given by:

$$F = \frac{B_\phi(a)}{< B_\phi >}, \tag{2.12}$$

said *reversal parameter*, which represents the normalized toroidal field at the edge.

Chapter 3

The RFX-mod device and experimental highlights

RFX-mod (Reversed Field eXperiment-modified) is the largest experiment in the world to investigate the magnetic confinement of hot plasmas in the RFP configuration, and is located in Padua, Italy.
RFX-mod was the first experimental device to show and investigate improved confinement RFP states, previously theoretically predicted using the MHD model. Such improved confinement RFP states are characterized by a dominant mode in the MHD spectrum, which impresses its helical symmetry to the plasma column, and are hence called quasi-single helicity (QSH) states. The RFX-mod experiment is also equipped with a system of saddle coils for the feedback control of MHD instabilities, and with a full set of diagnostics. In particular in-vessel magnetic probes make possible to measure and characterize Alfvénic oscillations, whose theoretical interpretation is provided in this Thesis.
Experimentally high-frequency magnetic activity has been detected at the edge region of the RFX-mod device. In particular a presence of five coherent peaks, in the form of Alfvén Waves (AW) in the power spectrum of the magnetic fluctuation, were measured at the edge of the plasma. While the first three peaks at lower frequency ($\leq$ 1MHz) are present only during the SHAx state, the two highest frequency peaks (around 1 MHz) are found during almost the full discharge duration. The Alfvénic nature of all the peaks were deduced by a linear relation between their frequency and the Alfvén velocity.

In this Chapter we will introduce the main features of the RFX-mod device, and we will briefly discuss the discovery of improved confinement QSH states and experimental observation of Alfvén Waves.

3.1 The RFX-mod device

RFX-mod (Reversed Field eXperiment-modified) is the largest experiment in the world that uses the RFP configuration and is located in Padua, Italy. Its main geometrical and physical features are shown in table 3.1.

R_0	2.00 m
a	0.459 m
I_P	$\leq$ 2.0 MA
B	$\leq$ 0.7 T
p_{vacuum}	$\sim 10^{-10}$ Pa
p_{plasma}	10^3 Pa
n_{plasma}	$5 \cdot 10^{19}$ m^{-3}
$T_{e,max}$	1.3 keV
t_{max}	0.5 s

Table 3.1: Main features of the RFX-mod experiment. R_0 and a represent the major radius and the minor radius of the torus, I_P represents the maximum achievable plasma current, B the maximum magnetic field strength that can be created by the coils and p_{vacuum} the pressure inside the confinement chamber before the gas is inserted, usually hydrogen or helium, whose ionization will form the plasma. p_{plasma} represents the typical pressure of the plasma, n_{plasma} the density of ions and electrons, $T_{e,max}$ the maximum electronic temperature obtained and t_{max} the maximum duration of a discharge.

The main components of the system for confinement and the creation of the magnetic field are described below (for further details see [Sonato et al., 2003]):

- The confinement chamber in toroidal geometry, with a major radius R_0 and a minor radius a, is characterized by an aspect ratio of 4.
- The inner surface of the confinement chamber is composed of 18 mm thick graphite plates, a material chosen because of the low Z value which reduces the effective value of the atomic number of ions present as impurities in the plasma.
- Outside the confinement chamber there is a copper toroidal structure (3 mm thick stabilizing shell) that contains it, its role is important in the control of the characteristics of balance and stability of the plasma contained in the vacuum chamber.
- The 48 poloidal coils that generate a toroidal magnetic field of maximum intensity equal to about 0.7 T.
- The magnetizing winding provides for the oscillation of the poloidal flux which causes the plasma current to grow up to 2 MA. It is composed of 200 windings that form 40 coils, each carrying a maximum current of 50 kA.
- The field shaping windings are formed by 16 coils that provide a vertical magnetic field that guarantees the correct positioning of the plasma in the vacuum chamber.
- A set of 192 coils for a feedback control of the magnetic field, they allow a good control of the external surface of the plasma avoiding excessive interactions between plasma and wall.

In Figure 3.1 are shown schematically the main components of the machine:

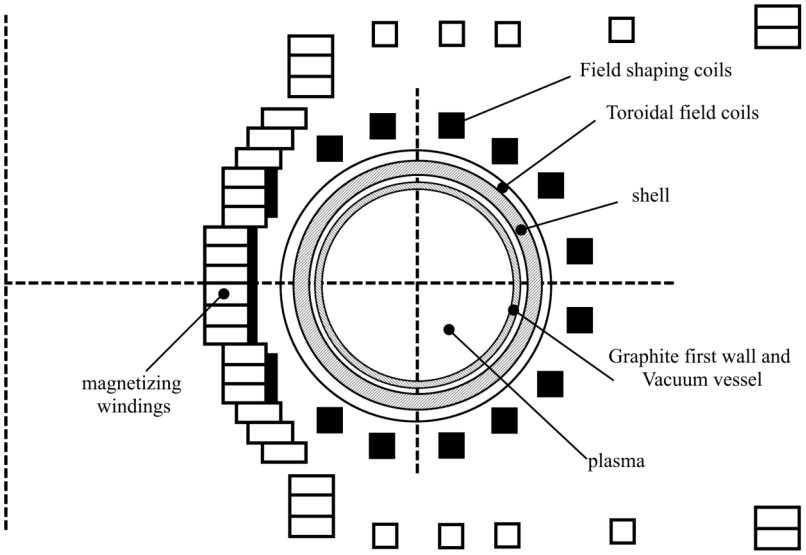

Figure 3.1: Schematic poloidal section of the RFX-mod machine.

3.2 Quasi Single Helicity RFP state

For several decades the RFP magnetized plasma has been observed in the Multiple Helicity (MH) state, characterized by high levels of magnetic fluctuations that led to reduced confinement levels. MH are states in which the non axis-symmetric perturbations are spectrally characterized by a wide range of the wave numbers m, n, in particular $m = 0$ and $m = 1$. The interaction of a broad spectrum of perturbed modes, that can be modelled using the magnetohydrodynamic model, leads to a turbulent behavior of the plasma. In particular, the magnetic field lines become chaotic and are free to move from the central region of the plasma to the edge one, which establishes a very fast transport mechanism of particles and energy, a mechanism that clearly degrades the confinement properties of the RFP plasma.

A strategy for the reduction of chaos in the RFP configuration was based on the theoretical prediction of the possible existence of the RFP in the so-called single helicity (SH) configuration, in which only one helical mode and its harmonics are present [Cappello and Paccagnella, 1992; Escande et al., 2000b].
Starting from the 2000s, first on the RFX experiment (previous to RFX-mod) and then on other RFP experiments scattered around the world, quasi-helical states with a spectrum called QSH (Quasi-Single-Helicity) have been observed, which approach the ideal SH states theoretically predicted, and which possess improved confinement thanks to the reduced level of magnetic chaos compared to the MH states [Martin et al., 2003]. The experimental results of the last few years on RFX-mod and on other operational RFPs showed, in particular through high current operations, a tendency of the RFP plasma to

move to the QSH regime. From the most recent experiments on RFX-mod it is observed that as the plasma current I_P increases, the system tends to spend a longer and longer time in the QSH state, moreover, always with increasing current, the QSH tends towards a state of SH equilibrium, in the sense that the amplitude of secondary modes decreases [Piovesan et al., 2009].
It is also observed that if the dominant perturbed mode reaches a width equal to about 4% of the poloidal field at the edge, a topological change takes place in the configuration of the magnetic field, as shown in Figure 3.2, that brings the plasma to achieve an almost stationary equilibrium with helical symmetry with a single magnetic axis (Single-Helical-Axis, SHAx, to distinguish it from the previous case with two different magnetic axis, double-helical-axis, DHAx) [Piovesan et al., 2009; Lorenzini et al., 2009a; Lorenzini et al., 2009b]. Improvement of RFP confinement properties ("chaos healing") following the expulsion of the magnetic separatrix of the dominant mode, DHAx-SHAx transition, was theoretically predicted in [Escande et al., 2000a]. This new state exhibits the presence of strong transport barriers, characterized by the presence of high temperature gradients of the electrons associated with the presence of regions of good confinement, as shown in Figure 3.3.

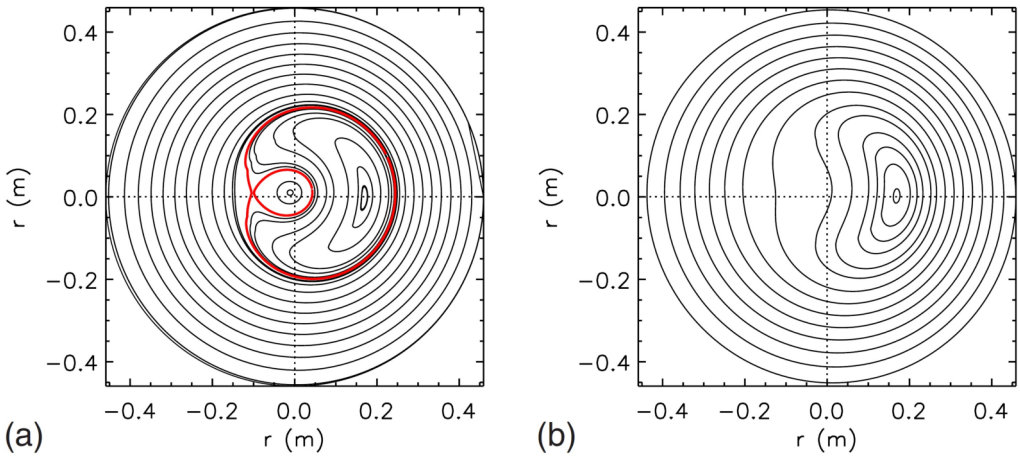

Figure 3.2: Magnetic topology reconstructed using only the axisymmetric fields and the eigenfunction of the dominant mode: (a) QSH with a magnetic island, (b) SHAx state. (from [Lorenzini et al., 2009a]).

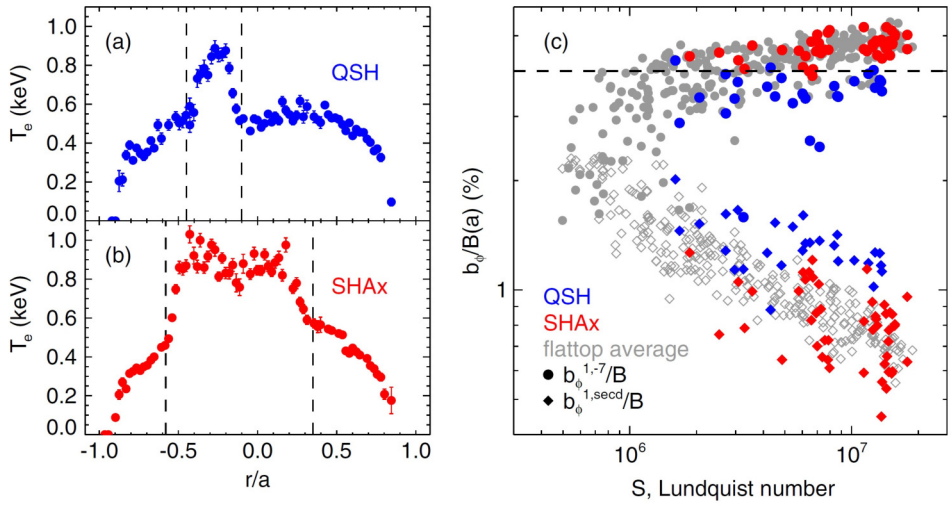

Figure 3.3: Electron temperature profiles measured by Thomson scattering during (a) a QSH state and (b) a SHAx state. (c) Relative amplitudes of the $n = -7$ mode (circles) and of the secondary modes (diamonds): flattop average (grey) and instantaneous values, when Thomson scattering data are available, during QSH (blue) and SHAx (red) (from [Piovesan et al., 2009]).

3.3 Experimental observation of Alfvén Waves in RFX-mod plasmas

High-frequency magnetic activity has been detected at the edge region of the RFX-mod reversed-field pinch (RFP) device [Spagnolo et al., 2011]. In particular, in this section, we will focus on the observation of coherent peaks in the power spectrum of the magnetic fluctuation measured at the plasma edge. These peaks are interpreted as Alfvén waves because their frequencies scale linearly with the Alfvén velocity of the plasma.

In Figure 3.4, taken from Ref. [Spagnolo et al., 2011], the color-coded spectrogram of a signal coming from a probe measuring the time derivative of the poloidal magnetic field ($\dot{b}_\theta$) fluctuation at $r/a = 1$ (where a is the minor radius of the torus) is shown, along with the time trace of the plasma current. Superimposed to the spectrogram, in red, is the time behavior of amplitude of the $(m, n) = (1, -7)$ mode (actually what is shown is the toroidal magnetic field component at the edge) to highlight the spontaneous transitions to the SHAx (Single Helical Axis) state. The vertical bright lines occurring during the crashes of the dominant mode are a sign of a global (i.e. at all frequencies) enhancement of the fluctuation level.

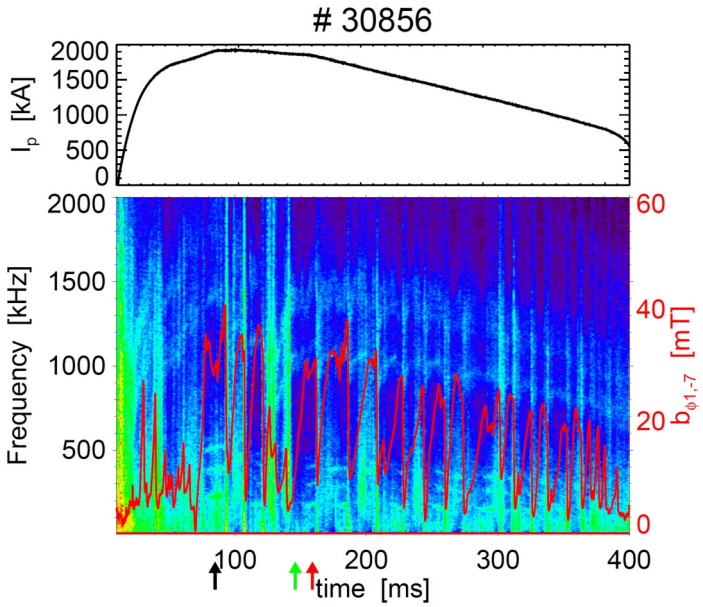

Figure 3.4: Top: plasma current I_p time trace; bottom: spectrogram of a $\dot{b}_\theta$ signal and (red line) amplitude of the dominant (m,n)=(1,-7) mode (y-axis on the right-hand side). The three arrows refer to the three time instants for the analysis in Figure 3.6 (from [Spagnolo et al., 2011]).

During the phases associated to large values of the dominant mode amplitude, a number of coherent modes (where coherent means in this case localized in frequency) are instead (hardly) visible, at values in the range $130 \div 500$ kHz. Indeed five distinct peaks, as more evident in Figure 3.5, where a frequency power spectrum evaluated during a single helical plasma is shown, are recognizable.

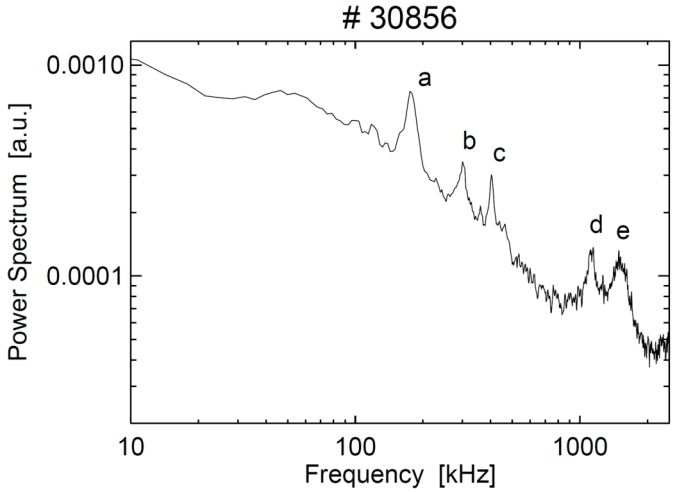

Figure 3.5: Power spectrum of a $\dot{b}_\theta$ signal evaluated during a SHAx state.

These peaks have been named a, b and c, d and e following the increase of their frequency (the amplitude associated to such coherent fluctuation is of the order of few tens of μT). While the first three peaks (a, b, c) are present only during the SHAx state, the two highest frequency peaks, d and e, (around 1 MHz) are found to exhibit different characteristics: they do not seem to be associated to any particular behavior of the dominant mode, being present during almost the full discharge duration.

To clarify this point, in Figure 3.6 three power spectra, evaluated in different time instants are plotted together. The time instants chosen for this analysis are those indicated by the three arrows in Figure 3.4. Two of the spectra shown (black and red ones) are associated to single helical axis states (it is worth to note the frequency shift associated to different plasma conditions), while the third one (green) is evaluated in an axis-symmetric RFP plasma. The three low frequency peaks are not present in the green spectrum, while the d and e ones seem not to be affected by the magnetic topology of the discharge.

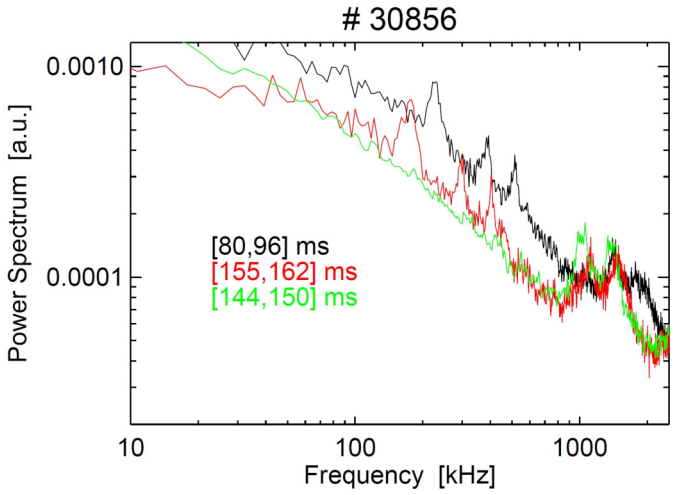

Figure 3.6: Power spectrum of a $\dot{b}_\theta$ signal evaluated during the three time instants indicated by the arrows of Figure 3.4: black and red lines refer to SHAx states, the green one to an axis-symmetric state.

The Alfvénic nature of all the peaks observed has been deduced by the linear relation between their frequency and the Alfvén velocity (evaluated by considering the poloidal magnetic field at the edge, and the electron density deduced by a central chord of the interferometer, and assuming $Z_{eff} = 1.5$ as a reasonable value for H discharges) in a number of discharges, as shown in Figure 3.7. In particular, in the shots analyzed the plasma current I_p was varied in the range 300 kA - 2 MA. The usual working gas is Hydrogen, but also Helium discharges have been considered. It is worth to note that, while the highest frequency modes (d and e) have been observed at almost all plasma current values, modes a, b and c, being associated to SHAx states, are present in the spectra only at the highest plasma currents, $I_p > 1.5$ MA.

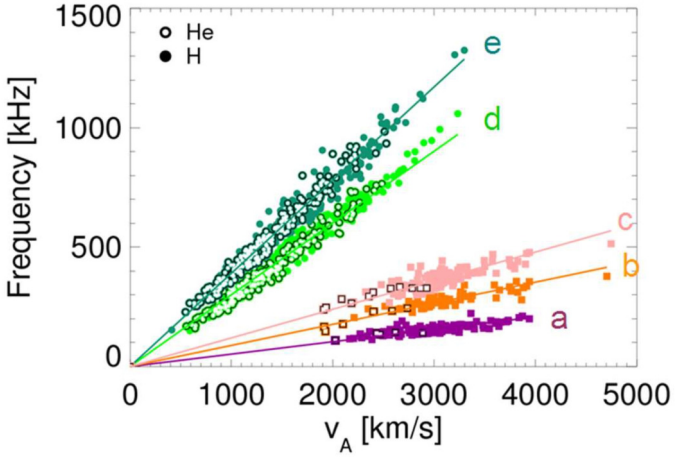

Figure 3.7: Relation between modes frequency and Alfvén velocity for a large database of H and He plasmas.

In the next chapters we will try to explain the above experimental observations from a theoretical point of view, through the analysis of frequency spectra from nonlinear MHD simulations with the SpeCyl code and the comparison with related analytical results deduced from ideal MHD model.

Part II

Theoretical models and numerical tools

Chapter 4

The magnetohydrodynamic model and Alfvén Waves

There are many physical models for the description of astrophysical and laboratory plasmas that differ in the level of complexity and the resulting physical phenomena they can describe.
There are two fundamental approaches: the microscopic-kinetic and the macroscopic-fluid one [Chen, 1984; Goldston and Rutherford, 1995].

The first , i.e. microscopic approach, deals with the description of a plasma as a system of many interacting bodies through long-range electromagnetic forces and works through the knowledge of the system configuration in phase space; this is done by determining the equations that describe the time evolution of the distribution function $f(r,v,t)$, which represents the density of particles in the phase space.

The second approach leads to describe the characteristics of plasma by macroscopic quantities that are a function of the three-dimensional position in space and of time, and through the relationships that determine the temporal evolution and the mutual relations. Modeling in terms of macroscopic quantities such as density, temperature, velocity and pressure is called the fluid approach.

The relationship between the two approaches is hierarchical because one can obtain the equations of the fluid model by starting from those that describe the distribution function, assuming that the frequency of the collisions between the components of the plasma is such as to bring the plasma close to thermodynamic equilibrium. In the process of derivation of a fluid model from a kinetic one some information is lost, which limits the field of application of the fluid model with respect to the kinetic one even if, within the limits of the approximations made, the macroscopic model describes a wide variety of phenomena in a much simpler way than its microscopic counterpart.

Macroscopic fluid models, in turn, can provide basically two levels of description: the description of a plasma as composed by two or more fluids of charged particles coupled together by the collisions and the Maxwell equations (for example, an electron fluid and an ion fluid), or the single-fluid MHD description, which is obtained through further approximations and will be analyzed and used in the following.

As we already stated previously, the MHD theory can support two basic types of magnetohydrodynamic waves, the Shear Alfvén Wave (SAW), also called torsional Alfvén wave, and the Compressional Alfvén Wave (CAW), also called magnetoacoustic or magnetosonic wave. The magnetoacoustic mode can be further divided into two distinct modes, the fast and slow magnetoacoustic waves. In this Chapter we will obtain the exact analytical solution for those waves, considering small amplitude linear waves in a spatially uniform plasma and in cartesian coordinates. This will provide a reference for the discussion in the following chapters of the waves in the nonuniform plasmas and cylindrical geometry. The waves will be assumed to have frequencies below the ion cyclotron frequency.

In this chapter we will introduce the magnetohydrodynamic model and its application limits. Then we will describe the waves in the MHD model: the Alfvén waves and their characteristics.

4.1 The single-fluid MHD model

The *single-fluid magnetohydrodynamics model*, also simply called MHD model, provides a description of a plasma as a conductive fluid in an electromagnetic field, with its own mass density ρ, velocity $\mathbf{v}$, and pressure p through a system of differential equations.
Appropriate algebraic manipulations of the two fluid model equations described in [Goldston and Rutherford, 1995] make possible to derive a system of single fluid differential equations in which unknown quantities such as ρ, $\mathbf{v}$ and p are defined as appropriate linear combinations of relative quantities for ions and electrons. The use of specific approximations, which will be described below, then allows to obtain the equations of the single-fluid magnetohydrodynamic model, which we will call MHD model for brevity, which are given by:

$$\nabla \cdot \mathbf{B} = 0 \qquad \text{No magnetic monopoles} \tag{4.1a}$$

$$\nabla \times \mathbf{E} = -\frac{\partial \mathbf{B}}{\partial t} \qquad \text{Faraday's law} \tag{4.1b}$$

$$\nabla \times \mathbf{B} = \mu_0 \mathbf{J} \qquad \text{Ampére's law} \tag{4.1c}$$

$$\mathbf{E} = \eta \mathbf{J} - \mathbf{v} \times \mathbf{B} \qquad \text{Ohm's law} \tag{4.1d}$$

$$\frac{\partial \rho}{\partial t} + \nabla \cdot (\rho \mathbf{v}) = 0 \qquad \text{Continuity equation} \tag{4.1e}$$

$$\rho \left[\frac{\partial \mathbf{v}}{\partial t} + (\mathbf{v} \cdot \nabla)\mathbf{v} \right] = \mathbf{J} \times \mathbf{B} - \nabla p + \rho \nu \nabla^2 \mathbf{v} \qquad \text{Equation of fluid motion} \tag{4.1f}$$

$$\frac{\mathrm{d}}{\mathrm{d}t}\left(\frac{p}{\rho^\gamma} \right) = 0 \qquad \text{Adiabatic equation of state} \tag{4.1g}$$

where $\mathbf{E}$ and $\mathbf{B}$ represent the electrical and magnetic field, $\mathbf{J}$ current density, γ represents the ratio between the specific heat at constant pressure and constant volume, and η and ν represent the electrical resistivity and the viscosity of the fluid.
This model can describe the equilibrium, stability and dynamical properties of a plasma in

a wide range of physical parameters, which encompass astrophysical, laboratory and fusion plasmas. From now on, our discussion will mainly focus to the field of thermonuclear fusion plasma, which is the subject of this Thesis.

Scope of validity and approximations

The scope of validity of the MHD model is determined by the approximations made to obtain equations (4.1), which essentially consist in limiting to the study of phenomena characterized by times scales longer than the inverse of plasma frequency ω_p and spatial scales greater than the Debye length λ_D, both of which are defined in section 1.1. This allows the study of the macroscopic dynamics of a fusion plasma in a magnetic confinement device, as the two constraints described above are widely respected.
Considering this spatial and temporal constraints is equivalent to imposing the quasi-neutrality of the plasma, $n_i \sim n_e$, which allows to neglect the density of electric charge $\rho_c = n_i - n_e$. It should be noted however that the quasi-neutral condition does not imply that the electric field is divergence-free, as can be seen by integrating the Poisson equation $\epsilon_0 \nabla \cdot \mathbf{E} = \rho_c$ once the equations (4.1) are solved.
An additional approximation is to neglect the mass of electrons compared to that of the ions, while the isotropic viscosity term in (4.1f) is a simplification of the general case in which the viscosity is a tensor quantity.
If the electrical resistance η and the viscosity ν of the plasma are neglected, the equations (4.1) are called *the ideal MHD model*.

4.1.1 Ideal MHD equilibrium of toroidal plasmas

The use of the MHD model allows the study of the properties that a magnetic field has to possess in order to produce the forces necessary to maintain a plasma in a state of equilibrium. The configuration of the magnetic field in such a situation must be such as to compensate, with the forces it exerts, the tendency of the plasma to expand outwardly. The simplifications to be used to study equilibrium situations using the MHD model consist of assuming a stationary state, where no physical quantity depends on time, and a static plasma, so $\mathbf{v} = 0$. A further simplification is to consider the ideal MHD model, which therefore imposes $\mathbf{E} = 0$ for (4.1d).

Under this simplifications, an equilibrium of the toroidal configuration is regulated by the ideal MHD equilibrium equation, the so-called *force-balance equation*

$$\nabla p = \mathbf{J} \times \mathbf{B}. \tag{4.2}$$

If we substitute for $\mathbf{J}$ from Ampère's law into the force-balance equation (4.2), we obtain the *pressure balance condition*

$$\nabla \left(p + \frac{B^2}{2\mu_0} \right) = \frac{1}{\mu_0} (\mathbf{B} \cdot \nabla) \mathbf{B}. \tag{4.3}$$

The terms on the right-hand side of equation (4.3) comes from the *bending* and *parallel compression* of the field lines, whereas the terms on the left-hand side indicate that the

magnetic field may be considered to have a *magnetic pressure* given by $B^2/2\mu_0$. The ratio of the plasma pressure to the magnetic pressure is defined as

$$\beta = \frac{2\mu_0 p}{B^2}. \tag{4.4}$$

The quantity β is a measure of the efficiency of a given magnetic field to sustain a given plasma equilibrium. Laboratory plasmas tends to have β values in the range of a ten per cent at most, so that the magnetic field plays a major role in the dynamics of the plasma.

Equation (4.2) obviously tells us that **J** and **B** are each perpendicular to ∇p. As a result, they must lie on the surfaces of constant p, which are called *magnetic surfaces*. In the axis-symmetric case, the magnetic field profiles of the equilibrium configuration can be obtained by solving the Grad-Shafranov equation. In this approach, the magnetic field is computed by solving an equation for the poloidal magnetic flux function Ψ, and the magnetic surfaces correspond to surfaces of constant Ψ [Grad and Rubin, 1958]. In a first approximation, one can assume $\beta = 0$, thus neglecting toroidal effects. In this case, the magnetic field admits a component B_ϕ in the toroidal direction and a component B_θ in the poloidal one, but no radial component; the same is true for every other field. Moreover, there is a smooth radial density gradient ∇p so that the surfaces of constant p are nested, concentric tori. The magnetic axis (defined as the zero radius magnetic surface) corresponds to the geometric axis of the torus. This configuration is sketched in Figure 4.1.

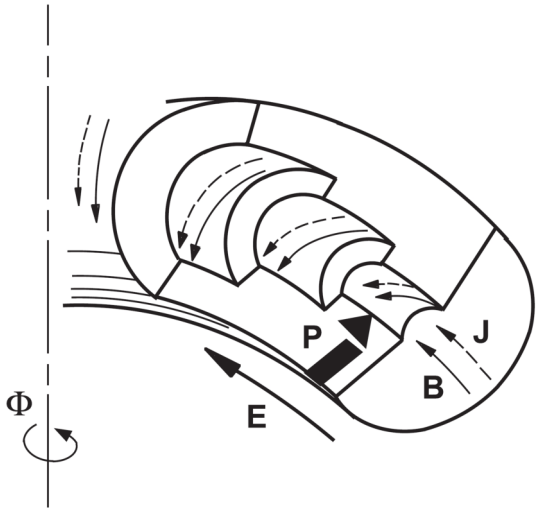

Figure 4.1: Schematic view of magnetic and current density field lines, pressure gradient and magnetic surfaces for a typical magnetic confinement configuration. The toroidal system of reference and the cylindrical coordinates are shown in Figure 2.4.

Since the resulting equilibrium configuration is axis-symmetric, the torus can be approximated as a straight periodical cylinder. The toroidal coordinate ϕ is thus substituted by the axial coordinate

$$z \equiv R_0 \phi, \tag{4.5}$$

and all of the equilibrium variables are taken to be periodical in this coordinate.

4.1.2 Ideal instabilities

Once an equilibrium configuration has been obtained, the stability properties of such a configuration must be studied. In general, an equilibrium is stable if any perturbation applied to it does not grow in time. We expect that unstable displacements cause the magnetic field lines to bend: since this, in general, results in an increase of the magnetic energy, the instability is further stabilized by the elastic reaction of the field line, which behaves like a rubber band.

The stabilizing effect vanishes in special surfaces where the wavefront $\mathbf{k}$ of the perturbation is parallel to the magnetic field:

$$0 = \mathbf{k} \cdot \mathbf{B} = k_\phi B_\phi + k_\theta B_\theta = \frac{n}{R_0} B_\phi + \frac{m}{r} B_\theta, \tag{4.6}$$

where

$$\mathbf{k} \equiv \frac{n}{R_0} \hat{\mathbf{e}}_\phi + \frac{m}{r} \hat{\mathbf{e}}_\theta \tag{4.7}$$

is the wave vector of the perturbation, described by an helical normal mode in the plasma. Indeed, it can be proved that unstable perturbations are localized near these surfaces.

The stability of the equilibrium configuration can be characterized using the safety factor $q(r)$ defined in (2.10). The resonance condition (4.6) then becomes

$$q(r) = -\frac{m}{n}. \tag{4.8}$$

Magnetic modes (i.e. m,n pairs) for which equation (4.8) is satisfied are called *resonant modes*, and surfaces where a magnetic mode is resonant are called *resonant surfaces*. Clearly, on such surfaces the field lines close upon themselves after a finite number of toroidal transits. In principle, unstable perturbations with mode numbers (m,n) can be avoided by constructing the magnetic geometry such that the corresponding resonant surface does not appear in the plasma. One of the most common modes in toroidal confinement devices is a *kink mode* with poloidal mode number $m = 1$, whose dynamics is characterized by a helical displacement of the toroidal plasma, as shown in Figure 4.2.

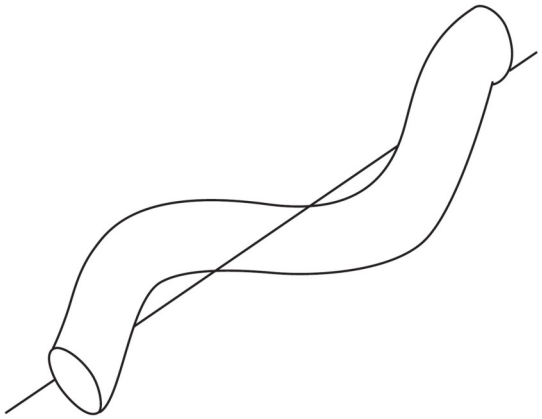

Figure 4.2: Plasma perturbation corresponding to a long wavelength $m = 1$ kink instability (from [Freidberg, 2014, p. 374]).

The previous discussion applies to perfectly conducting (i.e. zero resistivity) plasmas, whose instabilities are thus called *ideal instabilities*. The characteristic time scale associated with those modes comes from a possible solution for incompressible waves propagating along the field lines, which travels with Alfvén velocity:

$$v_A = \frac{|B|}{\sqrt{\rho \mu_0}}. \tag{4.9}$$

The characteristic time spent for travelling a distance equal to the system size is called the *Alfvén time*:

$$\tau_A = \frac{a}{v_A}, \tag{4.10}$$

which represents the shortest time scale supported by the MHD model.

4.1.3 Resistive instabilities

The introduction of resistivity can completely alter the stability properties of the plasma described by the MHD model. Indeed, in the ideal case the plasma is tied to the magnetic field lines, and the topology of the magnetic field cannot change. On the contrary, the addition of even the smallest amount of resistivity relaxes this constraint and allows the magnetic field lines to *reconnect* across the resonant surface, with a change in magnetic topology, and the formation of a *magnetic island*.

Modes of this type are called *resistive instabilities*, and the most common of these is the *tearing mode*, so named because the magnetic flux surface "tears" at the resonant surface. The tearing modes evolve on a time scale which is between τ_A and τ_R, where

$$\tau_R \equiv \frac{\mu_0 a^2}{\eta} \tag{4.11}$$

is the so-called *resistive diffusion time* which in hot plasmas is the longest of the time scales described by resistive MHD equations. The ratio between these two time scale is given by the so-called *Lundquist number*

$$S = \frac{\tau_R}{\tau_A}. \tag{4.12}$$

In most cases of interest $S \gg 1$ ($S \sim 10^6$ for thermonuclear plasmas, $S \sim 10^{12}$ for solar corona). Thus tearing modes evolve on a time scale that can be many order of magnitude slower that that of ideal instabilities or Alfvén waves.

Of course, though the addition of resistivity introduces a new class of instabilities, ideal instabilities can be present in resistive plasmas too. In other words each ideal instability has a resistive counterpart. For instance, with a finite resistivity the kink mode is called resistive kink.

4.1.4 Magnetic reconnection

As mentioned in the previous section, the introduction of a finite resistivity allows the magnetic field lines to reconnect across the resonant surfaces, with a change in magnetic topology. In fact the magnetic topology is perfectly preserved only in a magnetofluid with zero electrical resistivity, as the *Alfvén's theorem of flux-freezing* states (see Appendix A). Since electrical resistivity appears in the *induction equation* (for derivation see Appendix A)

$$\frac{\partial \mathbf{B}}{\partial t} = \nabla \times (\mathbf{v} \times \mathbf{B}) + \frac{\eta}{\mu_0} \nabla^2 \mathbf{B}, \tag{4.13}$$

as a coefficient in front of the second derivative $\nabla^2\mathbf{B}$, even if it's small, its effect can become important in a layer where the magnetic field gradient is large. Since large gradients of magnetic field are associated with large current densities, such regions are often called *current sheets*. In a low-resistivity plasma, cutting and pasting of field lines can take place within current sheets, while everywhere else the magnetic topology may be taken to be preserved.

To explain this phenomenon lets consider a typical current sheet with oppositely directed magnetic fields above and below, as shown in Figure 4.3. The large value of $\nabla^2\mathbf{B}$ in the central region would make the electrical resistivity term important there and hence the magnetic field would decay away in the central region. Since the magnetic fields have the pressure $B^2/2\mu_0$ associated with them, a decrease in the magnetic field would cause a pressure decrease in the central region. If the plasma-β defined in Eq. (4.4) is of the order of 1 or smaller, then the magnetic pressure constitutes an important fraction of the total pressure and the decay of the magnetic field in the central region would cause an appreciable depletion of the total pressure there. Therefore we expect that the plasma from above and below with fresh magnetic fields would be sucked into the central region. This fresh magnetic field would then decay and more plasma from above and below would be sucked in to compensate for the pressure decrease due to this decay. Thus the cutting and pasting of field lines takes place in the central region. This process, known as *magnetic reconnection* or *neutral-point reconnection*, may go on as long as fresh magnetic fields are brought to the central region. Since plasmas from the top and the bottom in Figure 4.3 push against the central region, the plasma in the central region is eventually squeezed out sideways with an outward velocity v_0. This process therefore converts the magnetic energy of the plasma into the kinetic energy.

The solar flares are a striking example of magnetic reconnection events that takes place on the Sun's surfaces and cause the coronal mass ejection. An analogous phenomenon in the fusion plasmas (in particular tokamak) are the so-called *sawtooth oscillations*, in which due to the resistive internal kink instability there is a periodic collapse of the core temperature as a result of periodic reconnection phenomena [Wesson, 2004, p. 365].

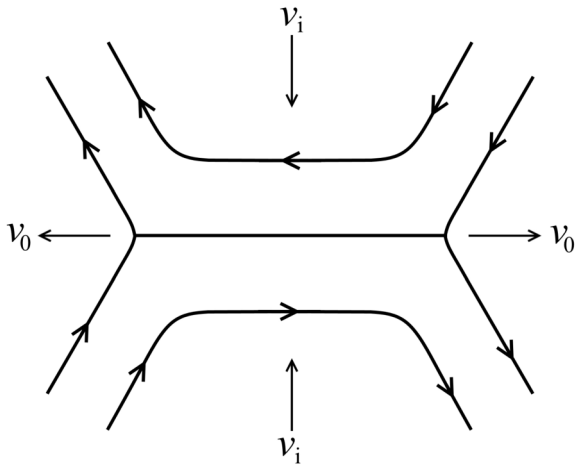

Figure 4.3: Magnetic reconnection in a current sheet with oppositely directed magnetic field lines above and below (from [Choudhuri, 1998, p. 322]).

4.2 Waves in the MHD model: Alfvén waves

In this section we consider the properties of small amplitude waves in a spatially uniform plasma, using the ideal MHD or hydromagnetic model described in section 4.1. The properties of small amplitude waves in the uniform plasma provide a reference for the discussion in the following chapters of the waves in the nonuniform plasmas. The waves will be assumed to have frequencies below of the ion cyclotron frequency $\Omega_i \equiv Be/m_i$.

Let us assume the equilibrium with the plasma at rest and with no zero-order electric field. We neglect the inertial term $(\mathbf{v}\cdot\nabla)\mathbf{v} \simeq 0$ in Eq. (4.1f) and we assume that the plasma has zero resistivity and viscosity (the ideal MHD model condition). If subscript 0 denote the equilibrium state, and subscript 1 denote the first-order perturbations associated with the wave motion, the equilibrium satisfies the force balance equation obtained from Eq. (4.1f),

$$\nabla p_0 = \mathbf{J}_0 \times \mathbf{B}_0. \tag{4.14}$$

From Eq. (4.1e) and Eq. (4.1g), the perturbed density and pressure satisfy

$$\frac{\partial \rho_1}{\partial t} + \nabla \cdot (\rho_0 \mathbf{v}_1) = 0 \tag{4.15}$$

and

$$p_1 = \frac{\gamma p_0}{\rho_0} \rho_1. \tag{4.16}$$

From the equation of fluid motion (4.1f), the perturbed fluid velocity satisfies

$$\rho_0 \frac{\partial \mathbf{v}_1}{\partial t} = -\nabla p_1 + \mathbf{J}_0 \times \mathbf{B}_1 + \mathbf{J}_1 \times \mathbf{B}_0. \tag{4.17}$$

The perturbed electric and magnetic fields satisfy the equations

$$\frac{\partial \mathbf{B}_1}{\partial t} = -\nabla \times \mathbf{E}_1 \tag{4.18}$$

and, from Eq. (4.1d) with $\eta = 0$,

$$\mathbf{E}_1 = -\mathbf{v}_1 \times \mathbf{B}_0. \tag{4.19}$$

If the wavelengths are much shorter than the scale lengths over which the equilibrium quantities ρ_0, p_0 and B_0 change, these quantities can be assumed to be constant, and the plasma is effectively uniform. The equilibrium current density $\mathbf{J}_0$ can therefore be neglected in Eq. (4.17). We have from Eq. (4.1c)

$$\mu_0 \mathbf{J}_1 = \nabla \times \mathbf{B}_1. \tag{4.20}$$

The uniform equilibrium magnetic field is chosen to lie along the z-axis. Let us also define the fluid vorticity in the magnetic field direction as

$$\zeta_{1z} = (\nabla \times \mathbf{v}_1)_z. \tag{4.21}$$

Equations (4.15)-(4.20) can then be manipulated to yield the following set of six differential equations:

$$\rho_0 \frac{\partial \zeta_{1z}}{\partial t} - B_0 \frac{\partial J_{1z}}{\partial z} = 0 \tag{4.22}$$

$$\mu_0 \frac{\partial J_{1z}}{\partial t} - B_0 \frac{\partial \zeta_{1z}}{\partial z} = 0 \tag{4.23}$$

$$\rho_0 \frac{\partial}{\partial t} \nabla \cdot \mathbf{v}_1 + \frac{B_0}{\mu_0} \nabla^2 B_{1z} + c_s^2 \nabla^2 \rho_1 = 0 \tag{4.24}$$

$$\frac{\partial B_{1z}}{\partial t} + B_0 \left(\nabla \cdot \mathbf{v}_1 - \frac{\partial v_{1z}}{\partial z} \right) = 0 \tag{4.25}$$

$$\rho_0 \frac{\partial v_{1z}}{\partial t} + c_s^2 \frac{\partial \rho_1}{\partial z} = 0 \tag{4.26}$$

$$\frac{\partial \rho_1}{\partial t} + \rho_0 \nabla \cdot \mathbf{v}_1 = 0. \tag{4.27}$$

where $c_s = (\gamma p/\rho)^{1/2}$ is the sound speed.

It is seen that the two differential equations (4.22) and (4.23) for ζ_{1z} and J_{1z} are uncoupled from the four differential equations (4.24)-(4.27) for $\nabla \cdot \mathbf{v}_1$, B_{1z}, v_{1z} and ρ_1. We should also note that in the equations for ζ_{1z} and J_{1z}, the spatial derivatives are only in the direction of the equilibrium magnetic field. Taking the Fourier transforms (see Appendix B) of Eq. (4.22) and Eq. (4.23) (or simply substituting the plane wave solution Eq. (B.3) into the differential equations), we obtain a consistency equation for a nontrivial solution which relates the frequency to the wavenumber. This is the dispersion equation for waves described by the variables ζ_{1z} and J_{1z}:

$$\omega^2 - v_A^2 k_z^2 = 0, \tag{4.28}$$

where the Alfvén speed v_A in the equilibrium plasma is given by

$$v_A = \frac{B_0}{(\mu_0 \rho_0)^{1/2}}. \tag{4.29}$$

The dispersion equation (4.28) is independent of the components of the wavevector perpendicular to the equilibrium magnetic field, and is also independent of the sound speed c_s.

Taking the Fourier transforms of Eqs. (4.24)-(4.27) yields a separate dispersion equation for waves described by the variables $\nabla \cdot \mathbf{v}_1$, B_{1z}, v_{1z} and ρ_1:

$$\omega^4 - \omega^2(v_a^2 + c_s^2)k^2 + v_a^2 c_s^2 k^2 k_z^2 = 0, \tag{4.30}$$

where $k = |\mathbf{k}|$. This dispersion equation does involve the perpendicular components of the wavevector, and the sound speed, in contrast to Eq. (4.28).

It is evident that the two dispersion equations (4.28) and (4.30), together with their corresponding sets of characteristic wave field variables, correspond to two distinct types of wave modes. The waves described by Eq. (4.28) are called *shear Alfvén waves*, and the waves described by Eq. (4.30) are called *magnetoacoustic* (or *magnetosonic*) waves (see Table 4.1). The magnetoacoustic mode may be further split into two distinct modes, the fast and slow magnetoacoustic waves. An arbitrary low-frequency disturbance can be represented as a superposition of the Alfvén wave and the fast and slow magnetoacoustic waves.

	Dispersion equation	Characteristic variables
Shear Alfvén wave	$\omega^2 - v_A^2 k_z^2 = 0$	J_{1z}, ζ_{1z}
Magnetoacoustic waves	$\omega^4 - \omega^2(v_A^2 + c_s^2)k_z^2$ $+v_A^2 c_s^2 k^2 k_z^2 = 0$	$\nabla \cdot \mathbf{v}_1$, v_{1z}, B_{1z}, ρ_1

Table 4.1: The dispersion equations and characteristic variables for the Alfvén and magnetoacoustic modes in the ideal MHD model.

Let us define the angle θ between the wavevector and the magnetic field $\mathbf{B}_0$, so that $k_z = k\cos\theta$. The first dispersion equation (4.28) then gives the positive frequency solution

$$\omega_A = v_a |k_z| = v_A k |\cos\theta| \tag{4.31}$$

of the shear Alfvén mode. The second dispersion equation (4.30) gives two positive frequency solutions: the fast magnetoacoustic mode, with

$$\omega_F^2 = \frac{k^2}{2}\left(v_A^2 + c_s^2 + ((v_A^2 + c_s^2)^2 - 4v_A^2 c_s^2 \cos^2\theta)^{(1/2)}\right) \tag{4.32}$$

and the slow magnetoacoustic mode, with

$$\omega_S^2 = \frac{k^2}{2}\left(v_A^2 + c_s^2 - ((v_A^2 + c_s^2)^2 - 4v_A^2 c_s^2 \cos^2\theta)^{(1/2)}\right). \tag{4.33}$$

We note that the phase velocity $v_{ph} = \omega/k$ is independent of k for all three modes, so all the modes are nondispersive, although they are anisotropic because v_{ph} depends on the angle of propagation θ. The characteristic phase velocity surfaces, that is, polar plots of the phase velocities of three modes against the angle θ, are plotted in Fig. 4.4

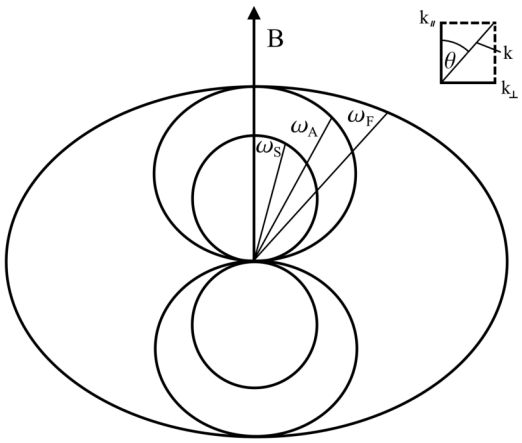

Figure 4.4: Dispersion curves $\omega_{A,F,S}(\theta)$, Eqs. (4.31), (4.32), (4.33), for $v_A^2/c_s^2 = 2$.

4.2.1 The Shear Alfvén Wave

If the wave is purely in the shear Alfvén mode, we can assume the characteristic variables listed in Table 4.1 for the magnetoacoustic mode to be zero. Also without loss of generality, for a uniform plasma we can choose the $\mathbf{k}$ vector to lie in the x-z plane

$$\mathbf{k} = (\sin\theta, 0, \cos\theta). \tag{4.34}$$

Thus we have (with $k_y = 0$),

$$v_{1z} = 0 \qquad \text{and} \qquad \nabla \cdot \mathbf{v}_1 = ik_x v_{1x} = 0. \tag{4.35}$$

Provided that $k_x \neq 0$ (i.e. $\sin\theta \neq 0$), we conclude that $v_{1x} = 0$ (the case of $k_x = 0$, i.e. propagation parallel or antiparallel to the magnetic field, is discussed in the next section). Thus the velocity perturbation $\mathbf{v}_1 = \mathbf{v}_A$ of the Alfvén mode is in the y-direction only, perpendicular to both the equilibrium magnetic field $\mathbf{B}_0$ and the wavevector $\mathbf{k}$. Therefore the field lines are bent, giving the rise to a magnetic tension. Also because $\nabla \cdot \mathbf{v}_1 = 0$, there is no density or particle pressure perturbation for this mode.

Since $B_{1z} = 0$ and $\nabla \cdot \mathbf{B}_1 = 0$, it follows that $B_{1x} = 0$, so that this mode only has a magnetic field perturbation in the y-direction, as exemplified in Figure 4.5. The absence of a magnetic field perturbation in the equilibrium magnetic field direction implies, since we have $\mathbf{B}_1 \cdot \mathbf{B}_0 = 0$ and $B^2 \simeq B_0^2 + 2\mathbf{B}_1 \cdot \mathbf{B}_0$ (to first order), that the magnetic field strength is constant to first order. The strengths of the magnetic and particle pressures in the plasma are thus each conserved; there is no compressive stress due to this wave, which therefore is

said to be a noncompressional *shear* wave. The phase speed of the wave lies between the speeds of the slow and fast magnetoacoustic waves (see Figure 4.4), so the shear Alfvén wave is also sometimes referred to as the *intermediate* wave.

Plasma flow across the magnetic field can increase the bending of the field; the shear wave acts to reduce the additional curvature of the field line. The currents that are set up to reduce the bending are closed partly along the field, so the shear wave introduces the field-aligned current J_{1z}. In a cylindrical geometry, the shear Alfvén wave is referred to as a *torsional* wave, with adjacent magnetic surfaces able to shear past each other without coupling to each other. Since ω is independent of $k_\perp$, the mode may be strongly localized to some field lines. This property is the origin of the singular Alfvén modes in and inhomogeneous sheared configuration which form the Alfvén *continuum* (as we will discuss in Section 6.2.1).

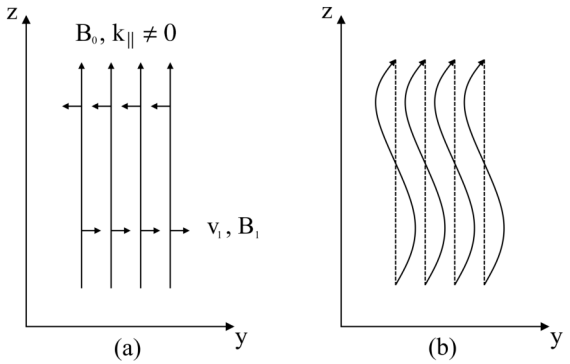

Figure 4.5: Magnetic field and velocity perturbations for the shear Alfvén wave shown in (a) vector component form and (b) combined form (from [Freidberg, 2014, p. 332]).

An important point to note is that the Alfvén wave dispersion relation is independent of the wavevector component perpendicular to the equilibrium magnetic field, and the wave cannot propagate perpendicular to the field (i.e. the phase velocity drops to zero). The group velocity

$$\mathbf{v}_g = \frac{\partial \omega_A}{\partial k} = v_A \cos\theta \hat{\mathbf{z}} \tag{4.36}$$

is aligned with the background magnetic field, that is, the wave energy is always carried along the direction of the background field, regardless of the direction of the wavevector.

4.2.2 The Fast and Slow Magnetoacoustic Modes

For a wave in the fast and slow magnetosonic mode, the characteristic variables for the shear Alfvén mode are zero. Thus, with the choice (Eq. 4.34) for the direction of $\mathbf{k}$, we have

$$\zeta_{1z} = i\mathbf{k} \times \mathbf{v}_1|_z = ik_x v_{1y} = 0, \tag{4.37}$$

so $v_{1y} = 0$. Also since $J_{1z} = 0$ and $\mu_0 \mathbf{J}_1 = \nabla \times \mathbf{B}_1$, it follows that $B_{1y} = 0$.

There are density perturbation in the wave (since $\nabla \cdot \mathbf{v}_1 \neq 0$), and perturbations of the magnetic field parallel to $\mathbf{B}_0$ (and thus of the field strength). Thus these modes are compressive in nature, even if the sound speed is zero. In contrast to the shear Alfvén wave, the fast and slow magnetoacoustic waves act to reduce magnetic or particle pressure gradients in the plasma.

The fast wave is sometimes called a *compressional Alfvén* wave. In the case of a low-β plasma, that is with $v_A^2 \gg c_s^2$, the fast wave dispersion relation is

$$\omega_F = v_A k \tag{4.38}$$

and the $\mathbf{v}_1$ is perpendicular to $\mathbf{B}_0$. See Figure 4.6. The fast wave can propagate and transport energy in any direction. The particle pressure and magnetic pressure in the fast wave increase and decrease in phase. In the slow wave, the particle and magnetic pressure vary out of phase.

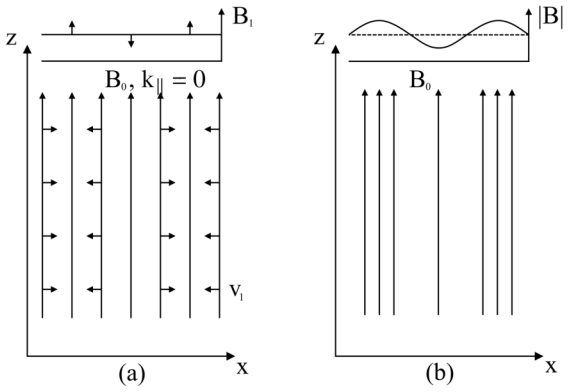

Figure 4.6: Magnetic field and velocity perturbations for the compressional Alfvén wave shown in (a) vector component form and (b) combined form (from [Freidberg, 2014, p. 333]).

For parallel or antiparallel propagation ($\sin\theta = 0$), the fast mode loses its compressive character and becomes degenerate with the Alfvén mode, in that both modes have a phase speed v_A, with a perturbation magnetic field perpendicular to the equilibrium field. The slow mode in this case is a pure sound mode with phase speed c_s.

Equations (4.31), (4.32) and (4.33) indicate that $\omega^2 \geq 0$. Hence frequencies are real. Adding dissipation will only introduce wave damping, $\omega \rightarrow \omega + i\gamma$, $\gamma < 0$. There are no unstable MHD modes in a homogeneous plasma, which represents global thermodynamic equilibrium, the lowest energy state a system may reach. Instability arises only for sufficiently strong spatial inhomogeneity. The overall above analysis of waves solutions in the MHD model will be considered again in Chapter 6 for cylindrical plasmas, both uniform and with space inhomogeneities.

Chapter 5

The SpeCyl code

The SpeCyl code is a non-linear visco-resistive 3D MHD code, that is used since the early 90ties in the theoretical physics group of Consorzio RFX as the main modeling tool for numerical simulations of RFP and tokamak plasmas. The SpeCyl code was used to provide nonlinear MHD simulations of Alfvén waves analyzed in this Thesis. In this Chapter we will introduce its physical model and numerical formulation. Then, we will present the results of a modeling study, based on RFP simulations performed with the SpeCyl code, which shows a systematic repetition of quasi-single helicity states (QSH) in between the reconnection events, in agreement with experimental observations from the RFX-mod device. This is done both to show an example of application of the SpeCyl code and because the same numerical simulations studied in that work will used in this Thesis to characterize the Alfvén waves in the most realistic RFP conditions achievable with the SpeCyl code.

5.1 Numerical simulations of fusion plasma: the SpeCyl code

The SpeCyl code [Cappello and Biskamp, 1996] is a numerical code that integrates numerically, in cylindrical geometry, the equations of a simplified version of the visco-resistive MHD model. This model derives from the equations of the visco-resistive MHD model under two fundamental hypotheses: the first is that the mass density of the plasma remains constant during the temporal evolution of the plasma, while the second consists in neglecting the role of pressure, a hypothesis justified by the value assumed in the RFP configuration by the beta parameter $\beta < 0.1$. As we will see in the next chapters, even with these approximations the code is able to provide a qualitative agreement with the frequency spectrum of Alfvén waves observed experimentally.

The importance of the SpeCyl code in the work carried out in this Thesis is given by the fact that the frequency spectrum, used to study and characterize the Alfvén waves, is derived from the simulation data by tacking their Fast Fourier Transform in time.

5.1.1 Physical model

SpeCyl solves the equations of the MHD model written in dimensionless form. The derivation of MHD equations using dimensionless quantities is carried out in Appendix C, and leads to the following set of equations:

$$\rho\left[\frac{\partial \mathbf{v}}{\partial t}+(\mathbf{v}\cdot\nabla)\mathbf{v}\right]=\mathbf{J}\times\mathbf{B}+\rho\nu\nabla^2\mathbf{v} \tag{5.1a}$$

$$\frac{\partial \mathbf{B}}{\partial t}=\nabla\times(\mathbf{v}\times\mathbf{B}-\eta\mathbf{J}) \tag{5.1b}$$

$$\nabla\times\mathbf{B}=\mathbf{J} \tag{5.1c}$$

$$\nabla\cdot\mathbf{B}=0. \tag{5.1d}$$

Here, the radial coordinate r is normalized to a, time and velocity are normalized to the Alfvén time τ_A and velocity v_A respectively, and $\mathbf{B}$ is normalized to the initial value B_0 of the toroidal magnetic field on axis. Moreover, η is the inverse Lundquist number, $\eta=\tau_A/\tau_R\equiv S^{-1}$, and ν corresponds to the inverse viscous Lundquist number, $\nu=\tau_A/\tau_V\equiv M^{-1}$, see Appendix C.

In the SpeCyl code, the resistivity and viscosity profiles are not calculated in a self-consistent manner but are selected a priori and kept constant throughout the duration of the simulation. In particular, the functional form for these profiles is:

$$\nu(r)=\nu_0\left(1+ar^b\right) \tag{5.2a}$$

$$\eta(r)=\eta_0\left(1+cr^d\right) \tag{5.2b}$$

with the values of the parameters a, b, c, and d chosen to have profiles similar to those estimated experimentally.

The choice of the η_0 value allows to define the number of Lundquist S that characterizes the system, while the choice of the central value of the viscosity profile ν_0 allows to fix the value of another important dimensionless quantity called *magnetic Prandtl number*:

$$P\equiv\frac{\nu_0}{\eta_0}. \tag{5.3}$$

Another important parameter that controls the dynamics of the system, in particular in situations in which the term of inertia in the equations is negligible, is the *Hartmann number*:

$$H\equiv(\eta_0\nu_0)^{-\frac{1}{2}}. \tag{5.4}$$

An important feature of the code is the geometry in which the equations are solved. This is the cylindrical geometry, with periodic conditions on the cylinder bases. This choice allows to simulate the plasma of a toroidal device for magnetic confinement (such as a tokamak or an RFP) in the approximation of large aspect ratio R_0/a, where the toroidal effects are negligible. This approximation is particularly suitable for treatment of plasmas of the RFP type for which the effects due to the toroidal geometry are less important.

Up to recent years the plasma boundary condition were chosen to be an ideal, i.e. perfectly conducting shell. The magnetic field was tangent to the shell, while the electric field was perpendicular to it. Plasma flow was taken to be vanishing at $r = 1$. In the [Bonfiglio et al., 2013] (a brief review is given in Section 5.2) and following articles based on the SpeCyl code simulations, the boundary conditions were generalized to also admit a magnetic field that was not purely tangent, but on the contrary admitted an imposed radial component.

The parameters which must be set for each simulation are the applied axial electric field and the profiles of resistivity and viscosity. From these parameters, the initial magnetic field profiles are derived, which also define the plasma current, toroidal flux and pinch parameter. The model equations are hence solved by finite differencing in the radial coordinate r and a Fourier decomposition along the periodic θ and z coordinates. The discretization in time is performed using the so-called semi-implicit algorithm, which allows for a relatively large time step Δt and prevents numerical instabilities [Cappello and Biskamp, 1996].
The nonlinear verification benchmark between SpeCyl and another MHD code, called PIXIE3D, demonstrated an excellent agreement between the two codes in their common limit of application, showing that both code solve the nonlinear MHD equations with high accuracy and reliability [Bonfiglio, Chacón, and Cappello, 2010].

5.1.2 Spectral formulation of the code

The equation system (5.1) is solved in cylindrical coordinates (r, θ, z) with $r \in [0 : 1]$, $\theta \in [0 : 2\pi]$, $z \in [0 : 2\pi R_0]$ where R_0 is given by the aspect ratio of the torus. Typically we use $R_0 = 4$ to have the same aspect ratio as the RFX-mod experimental device.

The spatial discretization of the physical quantities is carried out in a radial direction through the finite difference method on a mesh formed by a number N_r of points, while the periodicity conditions in the directions θ and z allow a spectral decomposition formed by N_θ harmonics in the poloidal direction and by N_z harmonics in axial direction.

It follows that the generic quantity $f(r, \theta, z, t)$ can be written in the following form:

$$f(r,\theta,z,t) = \sum_{m=-N_\theta}^{N_\theta} \sum_{n=-N_z}^{N_z} f_{m,n}(r,t) \exp\left[i \left(m\theta + \frac{n}{R_0} z \right) \right], \tag{5.5}$$

in which the Fourier components $f_{m,n}(r,t)$ are constrained by the condition on the reality of the quantity $f(r, \theta, z, t)$, which can be written as:

$$f_{-m,-n} = f^*_{m,n}. \tag{5.6}$$

Using the Fourier decomposition (5.5) to rewrite equations (5.1) provides the following

system of equations:

$$\frac{\mathrm{d}\mathbf{v}_{m,n}}{\mathrm{d}t} + [(\mathbf{v}\cdot\nabla)\,\mathbf{v}]_{m,n} = [\mathbf{J}\times\mathbf{B}]_{m,n} + \left[\nu\nabla^2\mathbf{v}\right]_{m,n} \tag{5.7a}$$

$$\frac{\partial\mathbf{B}_{m,n}}{\partial t} = [\nabla\times(\mathbf{v}\times\mathbf{B})]_{m,n} - [\nabla\,(\eta\mathbf{J})]_{m,n} \tag{5.7b}$$

$$[\nabla\times\mathbf{B}]_{m,n} = \mathbf{J}_{m,n} \tag{5.7c}$$

$$[\nabla\cdot\mathbf{B}]_{m,n} = 0 \tag{5.7d}$$

where $[\quad]_{m,n}$ denotes the Fourier component (m,n) of the term in brackets. Nonlinear terms such as $[\mathbf{J}\times\mathbf{B}]_{m,n}$ are computed through convolution sums like:

$$a_{m,n} = \sum_{p,q} J_{p,q} B^*_{p-m,q-n}. \tag{5.8}$$

The advantage of the spectral formulation consists in being able to select the Fourier modes to be included in the calculation, based on their importance in the dynamics of the system. This allows a quite significant reduction in the calculation time compared to other numerical approaches. In the practical use of the code, one can choose a single mode (and possibly its helical harmonics) that allows to make simulations with a given helical symmetry, or a range of modes with different helicity, which allows to do"fully-3D" simulations.

5.2 Experimental-like helical self-organization in RFP modeling

In this Section we will give a brief review of the first nonlinear three-dimensional magnetohydrodynamic (MHD) numerical simulations , performed with the SpeCyl code, of the reversed-field pinch (RFP) that exhibit a systematic repetition of quasi-single helicity states with the same dominant mode in between reconnection events [Bonfiglio et al., 2013]. This was the first time that this distinctive experimental feature have been reproduced by a 3D MHD code. This analysis gave a satisfactory qualitative and quantitative agreement with respect to experimental observations that has been lacking so far (although previous modeling studies with the SpeCyl code played a fundamental role for the discovery of helical RFP states).

The same numerical simulation used in this publication will be later analyzed in this Thesis to see if the experimental observation of Alfvén Eigenmodes in RFP plasmas can be numerically reproduced in conditions of a "realistic " RFP configuration (although with present limitations of the code, such as cylindrical approximation, zero-β etc.).

The key ingredient to observe QSH states is the use of helical boundary conditions for the edge radial magnetic field B_r, consistent with a small helical modulation of the plasma magnetic boundary. Helical boundary conditions with $m = 1$ poloidal and $n = -7$ toroidal periodicity are used, corresponding to the standard dominant mode in RFX-mod. In the simulation a wide spectrum of 225 modes with $0 \le m \le 4$ is used. This spectrum

was employed and validated in previous simulation studies [Cappello, 2004; Cappello and Biskamp, 1996; Bonfiglio, Chacón, and Cappello, 2010].

We first consider a simulation with ideal boundary conditions. The on-axis Lundquist and viscous Lundquist numbers are set to $S = 10^6$ and $M = 10^4$, respectively. This corresponds to Hartmann and Prandtl numbers $H \equiv (SM)^{1/2} = 10^5$ and $P \equiv S/M = 100$, respectively. The initial condition is a nonreversed axis-symmetric Ohmic equilibrium with pinch parameter $\Theta = B_\theta(a)/< B_\theta > \simeq 1.6$ and reversal parameter $F = B_\phi(a)/< B_\phi > \simeq 0.15$, where $< \cdot >$ represents a volume average. The temporal evolution of the reversal parameter F and the normalized edge B_ϕ amplitudes of the most active $m = 1$ modes is shown in Figs. 5.1(a) and 5.1(b). The resulting sawtoothing dynamics closely reproduces what was already reported in past viscoresistive MHD studies with similar ideal boundary conditions. After a strong initial reconnection event leading to the reversal of the F parameter (i.e., to the formation of the RFP configuration), the system undergoes quasiperiodic cycles with reconnection events. This is followed by relatively longer phases with reduced MHD activity. In this simulation, the MH regime is typically observed in between reconnection events, while QSH phases occasionally occur, although without any specific dominant mode and with a rather small amplitude separation with respect to secondary modes.

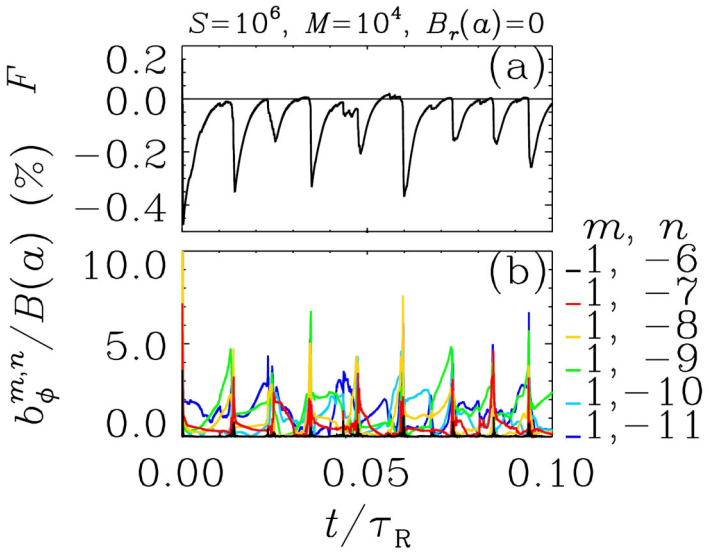

Figure 5.1: The temporal evolution of the simulation with ideal boundary condition, as discussed in the modeling study of the RFP [Bonfiglio et al., 2013].

A qualitative change occurs with the inclusion of helical boundary conditions. We consider now a simulation with the addition of a helical perturbation of the edge radial magnetic field. This perturbation is chosen with $m = 1$, $n = -7$ periodicity and a constant in time amplitude around 2% of the mean edge field. Such boundary conditions provide a

schematic representation of the plasma magnetic boundary during high current discharges in RFX-mod. The temporal evolution of the simulation with helical boundary conditions is shown in Figs. 5.2(a) and 5.2(b). It can be clearly seen that QSH phases with $1,-7$ dominant mode regularly occur in between reconnection events, while MH conditions seldom intervene. Thus, the observed numerical QSH dynamics presents the peculiar experimental features missing in previous modeling. The finite helical B_r perturbation also affects the periodic sawtoothing activity of the reversal parameter F, which on average becomes more frequent and less intense. This trend is confirmed for increasing helical perturbation amplitudes.

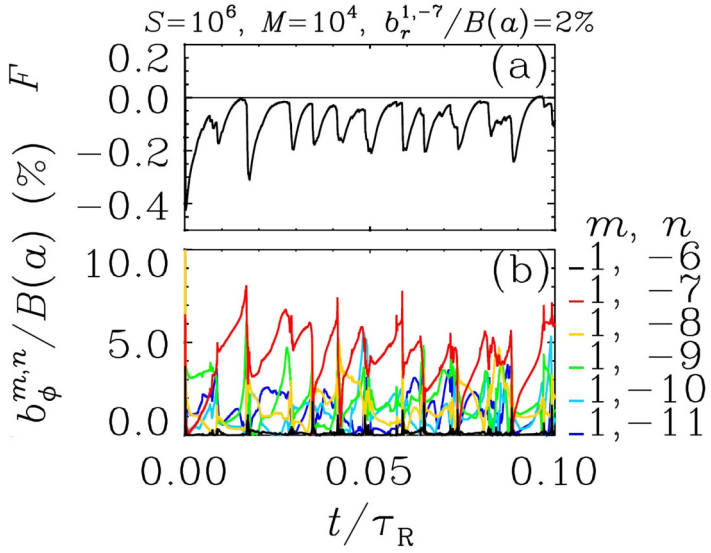

Figure 5.2: The temporal evolution of the simulation with helical boundary condition, as discussed in the modeling study of the RFP [Bonfiglio et al., 2013].

For comparison, a typical RFX-mod discharge with standard feedback control at high current is shown in Figs. 5.3(a) and 5.3(b). The main quantitative differences with respect to experimental findings are the wider range of numerical F oscillations and the larger level of secondary modes. This difference is mainly due to the use of unrealistic dissipation parameters. Taking Lundquist numbers of the order of $S = 10^7$ a temporal evolution of the simulation is obtained, which is qualitatively similar to the previous one Fig. 5.2. However, the average total amplitude of secondary modes decreases. This makes the repetition of QSH phases in between reconnection events particularly clear and systematic. In fact, QSH phases turn out to occur always in between reconnection events,with a close to realistic amplitude separation with respect to secondary modes.

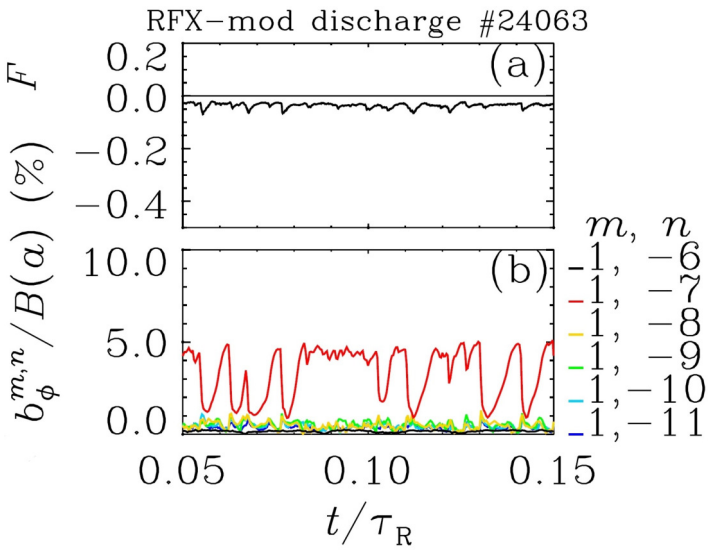

Figure 5.3: RFX-mod discharge, as discussed in the modeling study of the RFP [Bonfiglio et al., 2013].

Part III

Performed analysis

Chapter 6

Alfvén waves in cylindrical plasmas

In the ideal MHD approximation, the behaviour of the shear Alfvén wave is not sensitive to the plasma geometry since this wave propagates only along $\mathbf{B}_0$ lines and does not reflect off the plasma boundaries. However, the compressional wave does reflect off the plasma boundary or off metal wall boundaries, which can act like a waveguide or resonant cavity. Thus eigenmodes of the waves may exist, with spectra of discrete eigenfrequencies called Compressional Alfvén Eigenmode (CAE). The geometry is therefore very significant in determining the modes of propagation of the compressional wave. Nevertheless, wave propagation in a toroidal plasma is often modelled in cylindrical geometry, first because the mathematics is much simpler and second because a torus behaves, in most respects, like a bend cylinder.

In this Chapter we will compute the equations of Alfvén waves in cylindrical geometry and with ideal boundary condition (perfectly conducting wall that contains the plasma). This analytical study is an original synthesis of several textbooks and scientific articles [Cramer, 2001; Villard and Vaclavik, 1997; Musielak and Suess, 1989]. The resulting equations will be compared to those for free Alfvén waves in cartesian coordinates, as derived in Chapter 4. In particular we will consider waves in periodic straight cylindrical column of both uniform and non-uniform plasma (with non uniform density $\rho_0(r)$ and /or magnetic field $\mathbf{B}_0(r)$). The non-uniform case, compared to the uniform one, will be characterised by a new Alfvén mode, the Global Alfvén Eigenmode (GAE), and new phenomena like phase mixing and Alfvén resonance absorption. As we will see, while in the uniform case we are still able to obtain an analytical solution for shear and compressional modes, in the non-uniform case this is not always possible. Therefore we will employ the *local* or *Wentzel-Kramers-Brillouin* (WKB) approximation and numerical calculations to obtain the frequencies we are interested in for the analysis of SpeCyl simulations in Chapter 8.

It has to be noted that the SpeCyl code, as discussed in Section 5.1.1, is a visco-resistive numerical code, with viscosity and resistivity given by Eqs. (5.2), and so one could argue that the ideal MHD model is not suited for the analysis of SpeCyl simulations. But as we will see in the following chapters these dissipative terms only introduce a damping effect and cause the fields to decay in time, without actually affecting the frequency spectra

themselves. A more detailed treatise of the effects of dissipative terms on MHD waves can be found in [Cramer, 2001, p. 29].

6.1 Uniform plasma case

In this Section we will consider a uniform plasma in cylindrical geometry with ideal boundary conditions. As in Chapter 4 we will use the ideal MHD model in the cold plasma approximation ($p = 0$). Therefore, as before, we assume the equilibrium with the plasma at rest and with no zero-order electric field. We neglect the inertial term $(\mathbf{v}\cdot\nabla)\mathbf{v} \simeq 0$ in Eq. (4.1f) and we assume that the plasma has zero resistivity and viscosity (the ideal MHD model condition). The subscript 0 will denote the equilibrium state, and subscript 1 will denote the first-order perturbations associated with the wave motion. In particular we will compute the dispersion relations for shear Alfvén and compressional modes to see if and how they change from the free case discussed in Chapter 4.

6.1.1 Shear Alfvén Wave

We now will compute the dispersion relation for the Shear Alfvén Wave in a uniform axial magnetic field $\mathbf{B}_0$, uniform density ρ_0 and $\mathbf{v}_0 \equiv 0$ (plasma at rest), in the cold plasma approximation $p_0 = 0$. For the shear Alfvén mode we can assume the characteristic variables listed in Table 4.1 for the magnetoacoustic mode to be zero. Therefore $\rho_1 = 0$ and for Eq. 4.16 $p_1 = 0$. If the equilibrium quantities ρ_0 and B_0 are constant, the equilibrium current density $\mathbf{J}_0$ can be neglected in Eq. (4.17).

From Eq. (4.17) and Eq. (4.20), the perturbed velocity then satisfy

$$\rho_0 \frac{\partial \mathbf{v}_1}{\partial t} = \frac{1}{\mu_0}(\nabla \times \mathbf{B}_1) \times \mathbf{B}_0. \tag{6.1}$$

From Eq. (4.18) and Eq. (4.19), and the following identity

$$\nabla \times (\mathbf{A} \times \mathbf{B}) = \mathbf{A}(\nabla \cdot \mathbf{B}) - \mathbf{B}(\nabla \cdot \mathbf{A}) + (\mathbf{B} \cdot \nabla)\mathbf{A} - (\mathbf{A} \cdot \nabla)\mathbf{B}, \tag{6.2}$$

we can see that the perturbed magnetic field satisfies

$$\frac{\partial \mathbf{B}_1}{\partial t} = \nabla \times (\mathbf{v}_1 \times \mathbf{B}_0) = (\mathbf{B}_0 \cdot \nabla)\mathbf{v}_1 = B_0 \frac{\partial \mathbf{v}_1}{\partial z}, \tag{6.3}$$

where in the last two steps we used fact that $\mathbf{B}_0$ is uniform and $\nabla \cdot \mathbf{v}_1 = 0$ (condition (4.35)).

Taking the time derivative of Eq. (6.1) and putting it together with the previous equation we obtain

$$\rho_0 \frac{\partial^2 \mathbf{v}_1}{\partial t^2} = \frac{1}{\mu_0}\left(\nabla \times \frac{\partial \mathbf{B}_1}{\partial t}\right) \times \mathbf{B}_0 = \frac{B_0}{\mu_0}\left(\nabla \times \frac{\partial \mathbf{B}_1}{\partial t}\right) \times \hat{\mathbf{z}} = \frac{B_0^2}{\mu_0}\left(\nabla \times \frac{\partial \mathbf{v}_1}{\partial z}\right) \times \hat{\mathbf{z}}.$$

Using the two identities:

$$\nabla(\mathbf{A} \cdot \mathbf{B}) = \mathbf{A} \times (\nabla \times \mathbf{B}) + \mathbf{B} \times (\nabla \times \mathbf{A}) + (\mathbf{A} \cdot \nabla)\mathbf{B} + (\mathbf{B} \cdot \nabla)\mathbf{A} \tag{6.4}$$

and

$$\mathbf{A}\times(\mathbf{B}\times\mathbf{C}) = (\mathbf{A}\cdot\mathbf{C})\mathbf{B} - (\mathbf{A}\cdot\mathbf{B})\mathbf{C}, \tag{6.5}$$

and the condition $v_{1z} = 0$ (4.35) it follows that

$$\begin{aligned}\frac{B_0^2}{\mu_0}\left(\nabla\times\frac{\partial\mathbf{v}_1}{\partial z}\right)\times\hat{\mathbf{z}} &= \frac{B_0^2}{\mu_0}\left[-\nabla\left(\hat{\mathbf{z}}\cdot\frac{\partial\mathbf{v}_1}{\partial z}\right) + \frac{\partial\mathbf{v}_1}{\partial z}\times(\nabla\times\hat{\mathbf{z}}) + (\hat{\mathbf{z}}\cdot\nabla)\frac{\partial\mathbf{v}_1}{\partial z} + \left(\frac{\partial\mathbf{v}_1}{\partial z}\cdot\nabla\right)\hat{\mathbf{z}}\right] \\ &= \frac{B_0^2}{\mu_0}\left[-\nabla\frac{\partial v_{1z}}{\partial z} + \frac{\partial^2\mathbf{v}_1}{\partial z^2}\right] \\ &= \frac{B_0^2}{\mu_0}\frac{\partial^2\mathbf{v}_1}{\partial z^2}.\end{aligned}$$

Finally we get

$$\frac{\partial^2\mathbf{v}_1}{\partial t^2} - v_A^2\frac{\partial^2\mathbf{v}_1}{\partial z^2} = 0, \tag{6.6}$$

where $v_A^2 = B_0^2/(\mu_0\rho_0)$ is the Alfvén velocity.

Let us compute this equation in cylindrical coordinate. We seek solutions of perturbed velocity in the form

$$\mathbf{v}_1(t,r,\theta,z) = \mathbf{v}_1^{m,n}(r)\exp^{i\left(m\theta+\frac{n}{R}z-\omega t\right)}. \tag{6.7}$$

Putting it in Eq. (6.6) we obtain

$$\left(\omega^2 - v_A^2\frac{n^2}{R^2}\right)\mathbf{v}_1^{m,n}(r) = 0,$$

and finally the dispersion relation is

$$\omega^2 - v_A^2 k_z^2 = 0, \tag{6.8}$$

where $k_z^2 = n^2/R^2$. This expression is identical to the one obtained in cartesian coordinates (Eq. 4.28). This is due the fact that, as said before, the shear Alfvén wave is not sensitive to the plasma geometry since it propagates only along $\mathbf{B}_0$ lines and does not reflect off the plasma boundaries, which we indeed did not had to impose in this discussion. In Figure 6.1 the normalized frequency dependence on k_z wavevector component is shown, in the case of $m = 0$, for the shear Alfvén wave.

6.1.2 Compressional Alfvén Eigenmode

To compute the compressional mode dispersion relation let us rewrite Eqs. (4.24)-(4.26) in the cold plasma approximation ($p_0 = 0 \Rightarrow c_s^2 = \gamma p_0/\rho_0 = 0$)

$$\rho_0\frac{\partial}{\partial t}\nabla\cdot\mathbf{v}_1 + \frac{B_0}{\mu_0}\nabla^2 B_{1z} = 0 \tag{6.9}$$

$$\frac{\partial B_{1z}}{\partial t} + B_0\left(\nabla\cdot\mathbf{v}_1 - \frac{\partial v_{1z}}{\partial z}\right) = 0 \tag{6.10}$$

$$\rho_0\frac{\partial v_{1z}}{\partial t} = 0. \tag{6.11}$$

Taking the time derivative of Eq. (6.10)

$$\frac{\partial^2 B_{1z}}{\partial t^2} + B_0 \left[\frac{\partial}{\partial t}(\nabla \cdot \mathbf{v}_1) - \frac{\partial}{\partial z}\frac{\partial v_{1z}}{\partial t} \right] = 0$$

and using the Eqs. (6.11) and (6.9) we get

$$\frac{\partial^2 B_{1z}}{\partial t^2} - v_A^2 \nabla^2 B_{1z} = 0, \tag{6.12}$$

where $v_A^2 = B_0^2/(\mu_0 \rho_0)$ is the Alfvén velocity.

Let's compute this equation in cylindrical coordinates

$$B_{1z}(t, r, \theta, z) = B_{1z}^{m,n}(r) \exp^{i\left(m\theta + \frac{n}{R}z - \omega t\right)}. \tag{6.13}$$

We seek solutions of Eq. (6.12), with ideal boundary conditions

$$0 = E_\theta\big|_{r=a} = \eta J_\theta\big|_{r=a} = \frac{\eta}{\mu_0}\frac{\mathrm{d}}{\mathrm{d}r}B_z\bigg|_{r=a}. \tag{6.14}$$

Replacing Eq. (6.13) in Eq. (6.12) we obtain

$$\frac{\partial^2 B_{1z}}{\partial t^2} - v_A^2 \left[\frac{1}{r}\frac{\partial}{\partial r}\left(r\frac{\partial B_{1z}}{\partial r} \right) + \frac{1}{r^2}\frac{\partial^2}{\partial \theta^2}B_{1z} + \frac{\partial^2}{\partial z^2}B_{1z} \right] = 0.$$

Deriving B_{1z}

$$\left\{ -\omega^2 - v_A^2 \left[\frac{\mathrm{d}^2}{\mathrm{d}r^2} + \frac{1}{r}\frac{\mathrm{d}}{\mathrm{d}r} - \frac{m^2}{r^2} - \frac{n^2}{R^2} \right] \right\} B_{1z}^{mn}(r) = 0,$$

and multiplying both members with $-r^2/v_A^2$ we obtain

$$\left[r^2\frac{\mathrm{d}^2}{\mathrm{d}r^2} + r\frac{\mathrm{d}}{\mathrm{d}r} + \left(\frac{\omega^2}{v_A^2} - \frac{n^2}{R^2} \right) r^2 - m^2 \right] B_{1z}^{mn}(r) = 0. \tag{6.15}$$

Defining the quantity

$$\xi^2 \equiv \left(\frac{\omega^2}{v_A^2} - \frac{n^2}{R^2} \right), \tag{6.16}$$

and performing the following substitution

$$r' = \xi r \tag{6.17}$$

we obtain the *Bessel's differential equation*

$$\left[r'^2\frac{\mathrm{d}^2}{\mathrm{d}r'^2} + r'\frac{\mathrm{d}}{\mathrm{d}r'} + r'^2 - m^2 \right] B_{1z}^{mn}(r') = 0, \tag{6.18}$$

where m is the order of the Bessel function.

The solution is given by a Bessel function of order m, which expression is, resubstituting r,

$$B_{1z}^{mn}(r) = B_{1z}^{mn}(0) J_m(\xi r). \tag{6.19}$$

Let's now impose the ideal boundary condition (6.14)

$$\frac{\mathrm{d}}{\mathrm{d}r} B_{1z}^{mn}(r = a) = 0 \quad \Longrightarrow \quad B_{1z}^{mn}(0) \frac{\mathrm{d}}{\mathrm{d}r} J_m(\xi a) = 0. \tag{6.20}$$

The solutions are the roots of the first derivative of the Bessel function of order m (this values can be derived and are well know[1]), which we name χ_{mj}, where j is the j-th root,

$$\xi a = \chi_{mj} \qquad \text{with} \quad j = 1, 2, 3 \ldots. \tag{6.21}$$

Therefore, taking the square of Eq. (6.21), we find the following dispersion relation

$$\xi^2 = \frac{\omega_{mj}^2}{v_A^2} - \frac{n^2}{R^2} = \frac{{\chi_{mj}}^2}{a^2}$$

$$\omega_{mj}^2 = v_A^2 \left(k_z^2 + \frac{{\chi_{mj}}^2}{a^2} \right) \qquad \text{with} \quad j = 1, 2, 3 \ldots, \tag{6.22}$$

where $k_z^2 = n^2/R^2$.

The first thing to note is that in this case we are considering only the fast magnetoacoustic mode, indeed assuming $c_s^2 = 0$ the slow magnetoacoustic mode's frequency is null, as can be seen from Eq. (4.33). Furthermore the expression of the compressional mode itself is different from the one in cartesian coordinates (Eq. (4.32)). In fact the effect of moving to cylindrical geometry and imposing the ideal boundary conditions (6.14) brings a set of Compressional Alfvén Eigenmodes (CAEs), whose frequency depends on j-th root of the derivative of Bessel function of order m. In Figure 6.1 the normalized frequency dependence on k_z wavevector component is shown, in the case of $m = 0$, for the first five CAEs.

[1] See for example http://wwwal.kuicr.kyoto-u.ac.jp/www/accelerator/a4/besselroot.htmlx

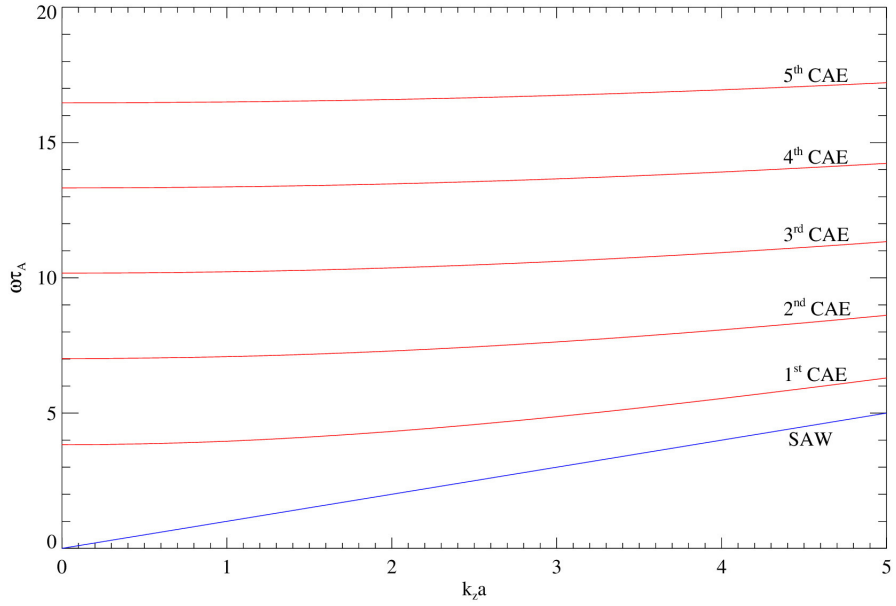

Figure 6.1: Case $m = 0$. Normalized frequency dependence on k_z wavevector component for SAW and the first five CAEs in cylindrical geometry.

6.2 Non-uniform plasma case

In this Section we will consider the case of a non-uniform plasma in cylindrical geometry with ideal boundary conditions. Compared to the previous uniform case, now the magnetic field $\mathbf{B}_0$ and/or plasma density ρ_0 are allowed to vary with radial coordinate r. Apart from that, we will use the same model and conditions used in the previous Section. In particular we will compute the dispersion relations for shear Alfvén and compressional modes as well as for the new Alfvén mode, the Global Alfvén Eigenmode. Also we will briefly discuss the new phenomena that arise from the non-uniformity of the plasma: phase mixing and Alfvén resonance absorption.

6.2.1 Continuous Shear Alfvén Wave and phase mixing

The magnetic field is assumed to have θ and z components and is allowed to vary with r in magnitude and direction:

$$\mathbf{B}_0(r) = B_{0\theta}(r)\hat{\boldsymbol{\theta}} + B_{0z}(r)\hat{\mathbf{z}}. \tag{6.23}$$

The plasma density ρ_0 is also allowed to vary with r.

To derive the shear Alfvén dispersion relation we start from the general case with finite pressure ($p_0 \neq 0$). Let us consider the linearized MHD equation of motion (4.1f)

expressed in terms of perturbed fluid velocity $\mathbf{v}_1$, magnetic field $\mathbf{B}_1$ and (particle plus magnetic) pressure p_T:

$$\rho_0 \frac{\partial \mathbf{v}_1}{\partial t} = -\nabla p_T + \frac{1}{\mu_0}(\mathbf{B}_1 \cdot \nabla)\mathbf{B}_0 + \frac{1}{\mu_0}(\mathbf{B}_0 \cdot \nabla)\mathbf{B}_1. \tag{6.24}$$

We also employ Faraday's equation (4.1b), combined with Ohm's law (4.1d) with zero resistivity $\eta = 0$:

$$\frac{\partial \mathbf{B}_1}{\partial t} = \nabla \times (\mathbf{v}_1 \times \mathbf{B}_0) \tag{6.25}$$

and the linearized version of the adiabatic equation of state (4.1g). For a wave of given frequency ω, we can derive from Eqs. (6.24)-(6.25), in cylindrical geometry, two coupled differential equations in p_T and velocity component v_{1r} (the analogous calculus but in cartesian coordinates was done by Musielak and Suess, 1989):

$$\frac{\mathrm{d}p_T}{\mathrm{d}r} - \tau v_{1r} = 0 \tag{6.26}$$

$$\frac{1}{r}\frac{\mathrm{d}}{\mathrm{d}r}(r v_{1r}) - \frac{q^2}{\tau} p_T = 0 \tag{6.27}$$

where

$$\tau = i\frac{\rho_0}{\omega}\left(\omega^2 - (\mathbf{k}\cdot\mathbf{v}_A)^2\right) \tag{6.28}$$

and

$$q^2 = k^2 - \frac{\omega^4}{\omega^2(c_s^2 + v_A^2) - c_s^2(\mathbf{k}\cdot\mathbf{v}_A)^2}, \tag{6.29}$$

where $\mathbf{k} = (0, k_\theta, k_z) = (0, m/r, n/R)$ is the wavevector, $k = |\mathbf{k}|$ and $\mathbf{v}_A = \mathbf{B}_0/\sqrt{\mu_0\rho_0}$ is the vector Alfvén velocity which now depends on r. The Alfvén wave and fast and slow magnetoacoustic waves described by ideal MHD model in Section 4.2 can be recovered, using cartesian geometry, from Eqs. (6.26) and (6.27) in the limit of a uniform plasma density and magnetic field (in the z-direction). This shows us that in the non-uniform case the two waves are coupled. In general when the wavevector $\mathbf{k}$ of the perturbation is not parallel or perpendicular to the equilibrium magnetic field $\mathbf{B}_0$ but oblique to it, we expect such perturbation to excite both types of the waves.

The second-order differential equation for v_{1r} is then

$$\frac{\mathrm{d}}{\mathrm{d}r}\left[\frac{\tau}{q^2 r}\frac{\mathrm{d}}{\mathrm{d}r}(r v_{1r})\right] - \tau v_{1r} = 0 \tag{6.30}$$

and that for p_T is

$$\frac{\tau}{r}\frac{\mathrm{d}}{\mathrm{d}r}\left(\frac{r}{\tau}\frac{\mathrm{d}p_T}{\mathrm{d}r}\right) - q^2 p_T = 0. \tag{6.31}$$

There are two possible singularities of Eqs. (6.30) and (6.31). One singularity occurs where $\tau = 0$, that is, at a point where

$$\omega(r) = |\mathbf{k}\cdot\mathbf{v}_A| = |k_\parallel(r)\cdot v_A(r)| = \frac{|k_\theta B_{0\theta} + k_z B_{0z}|}{\sqrt{\mu_0\rho_0}} = \frac{|\frac{m}{r}B_{0\theta} + \frac{n}{R}B_{0z}|}{\sqrt{\mu_0\rho_0}}, \tag{6.32}$$

where $k_\parallel = \mathbf{k}\cdot\mathbf{B}_0/|\mathbf{B}_0|$ and $v_A = |\mathbf{B}_0|/\sqrt{\mu_0\rho_0}$. This is the *Alfvén resonance condition*.

The condition (6.32) is also said to define the *continuous shear Alfvén wave spectrum*, or the *Alfvén continuum*, in a nonuniform plasma. For a given frequency and $\mathbf{k}$, the condition (6.32) is possibly satisfied only at isolated points in the density and magnetic field profiles. However, if just $\mathbf{k}$ is specified, every point in the plasma profile is associated with different frequency, given by Eq. (6.32). In a smoothly varying plasma profile we therefore have a continuous spectrum of frequencies, which formally corresponds to localized shear Alfvén waves with the same wavevector. It is noteworthy that the analogous calculation in cartesian coordinates bring the same result ($\omega = |\mathbf{k}\cdot\mathbf{v}_A|$). The existence of the continuous spectrum is also related to a *phase mixing* in time, leading to the decay of wave fields. We will discuss this phenomenon shortly below.

A second singularity occurs where $1/q^2 = 0$, that is, at a position in the density and magnetic field profile where the following condition holds:

$$\omega^2 = \frac{c_s^2(\mathbf{k}\cdot\mathbf{v}_A)^2}{v_A^2 + c_s^2}. \tag{6.33}$$

This condition is called the *cusp* or *compressive resonance condition*. However, in our case of cold plasma approximation, this singularity does not occur as $c_s^2 = 0$. Therefore in the following sections we will introduce a consequence of Alfvén resonance condition, that is the *Alfvén resonance absorption* process.

To illustrate the phase mixing phenomena let us consider a simpler case: an equilibrium uniform magnetic field $\mathbf{B}_0 = B_0\hat{\mathbf{z}}$ and non-uniform plasma density profile $\rho_0(r)$, with corresponding local Alfvén speed $v_A(r)$. For a wave with given frequency ω, we can derive from Eqs. (6.24)-(6.25), in cylindrical geometry, two coupled differential equation in p_T and the fields components $v_{1\theta}$ and $B_{1\theta}$:

$$\rho_0\frac{\partial v_{1\theta}}{\partial t} = -ik_\theta p_T + \frac{B_0}{\mu_0}\frac{\partial B_{1\theta}}{\partial z} \tag{6.34}$$

$$\frac{\partial B_{1\theta}}{\partial t} = B_0\frac{\partial v_{1\theta}}{\partial z}. \tag{6.35}$$

Taking $k_\theta = m/r = 0$, the perturbed velocity component $v_{1\theta}$ than satisfies the equation

$$\frac{\partial^2 v_{1\theta}}{\partial t^2} = v_A^2(r)\frac{\partial^2 v_{1\theta}}{\partial z^2}, \tag{6.36}$$

with the local dispersion relation $\omega(r) = k_z v_A(r)$ for each magnetic surface oscillating with its own frequency. For the initial condition of standing wave of fixed k_z, as time proceeds the phase of the wave on each field line changes, that is, we have phase mixing. In fact, each field line oscillates at the local Alfvén frequency, losing coherence with the motion of adjacent lines. This fact qualitatively explains the reason of the name "phase mixing". This effect effectively leads to the damping of any initial Alfvén perturbation in an inhomogeneous plasma at the rate:

$$\gamma_d \sim \left|\frac{\mathrm{d}}{\mathrm{d}r}\left(k_z v_A(r)\right)\right|. \tag{6.37}$$

Of course this considerations are also valid for any mode numbers (m, n) and in case of non-uniform magnetic field $\mathbf{B}_0$ and uniform plasma density ρ_0 or both $\mathbf{B}_0$ and ρ_0 non-uniform, as long as the shear dispersion relation is given by Eq. (6.32).

6.2.2 Compressional Alfvén Eigenmode and resonance absorption

Compared to the uniform case, with nonuniform magnetic field and/or plasma density there are no exact solutions for the compressional mode. In fact we can still solve the MHD equations in cylindrical geometry and ideal boundary conditions, Equations from (6.14) to (6.15). In this case, however, ξ will depend on the radial coordinate r

$$\xi^2 = \left(\frac{\omega^2}{v_A^2(r)} - \frac{n^2}{R^2} \right), \tag{6.38}$$

where, in the general case

$$v_A^2(r) = \frac{B_0^2(r)}{\mu_0 \rho_0(r)}. \tag{6.39}$$

Therefore the differential equation (6.18) with $\xi(r)$ cannot be cast anymore in the form of a Bessel equation and does not possess an analytic solution.

We can still solve the CAE equation (6.15) using a *local* or *WKB approximation* (similarly to what was done in Cramer, 2001, p. 183). That is we assume that each point in the plasma locally satisfies the homogeneous plasma dispersion relation. It's a good approximation when the density or magnetic field varies by only a small amount in a distance equal to one wavelength in the radial direction. Nevertheless, the WKB approximation is very useful for qualitative discussion even in cases with relatively high variable density and/or magnetic field in radial coordinate.

When this approximation is applied, the solution of the differential equation for B_{1z}^{mn} is found in the form

$$B_{1z}^{mn}(r) \propto J_m \left(\int_0^r \xi(r') \mathrm{d}r' \right). \tag{6.40}$$

Of course if ξ doesn't depend on r this expression becomes the same as in the homogeneous case (6.19).

Imposing the ideal boundary condition (6.14) we get

$$\frac{\mathrm{d}}{\mathrm{d}r} B_{1z}^{mn}(r = a) = 0 \quad \Longrightarrow \quad \frac{\mathrm{d}}{\mathrm{d}r} J_m \left(\int_0^a \xi(r') \mathrm{d}r' \right) = 0. \tag{6.41}$$

In this case the solution, from which we can derive the frequencies of the CAEs, is given by the condition

$$\int_0^a \xi(r') \mathrm{d}r' = \chi_{mj} \qquad \text{with} \quad j = 1, 2, 3 \ldots, \tag{6.42}$$

where, as before, χ_{mj} is the j-th root of derivative of Bessel function of order m.

We can rewrite the previous condition as

$$\int_0^a \left(\frac{\omega_{mj}^2}{v_A^2(r')} - \frac{n^2}{R^2} \right)^{1/2} \mathrm{d}r' = \chi_{mj} \qquad \text{with} \quad j = 1, 2, 3 \ldots, \tag{6.43}$$

with the following constrain on ω_{mj}^2 values

$$\omega_{mj}^2 \geq \frac{n^2}{R^2} v_A^2(r') \quad \forall r' \in [0, a]. \tag{6.44}$$

The values of the frequencies ω_{mj} can be derived then via numerical calculation, searching for ω_{mj} values for which the conditions (6.43) and (6.44) are satisfied.

A smooth plasma nonuniformity has an important effect for the propagation of the fast magnetoacoustic wave. This process, called Alfvén resonant absorbtion, has been proposed as a mean of providing supplementary heating of fusion plasmas, and as a possible explanation of the heating of the corona of the Sun and other stars.

When a magnetoacoustic wave propagates in a plasma of varying density and/or magnetic field, it can be absorbed under certain conditions, leading to a local heating of the plasma. The damping of the magnetoacoustic wave occurs because of the coupling with the continuous spectrum of the shear Alfvén wave. In particular it occurs when, in a specific location of the plasma, the frequency of the compressional wave is equal to that of the Alfvén resonance condition (6.32).
The ideal MHD model confirms the existence of this process and can describe some of its characteristics, but it doesn't provide an explicit damping mechanism and so gives no indication of how the energy in the wave is finally dissipated. When more realistic models, including kinetic effects, are employed, it is shown that the energy of the compressional mode may be absorbed via mode conversion into a short-wavelength mode, such as Kinetic Alfvén Wave (KAW) or Inertial Alfvén Wave (IAW), with subsequent collisionless and collisional damping of those waves.
Because of the difficulty in dealing analytically with this process, in this Thesis we will limit ourselfs into discussing the phenomenological features of this process when encountered in the analysed numerical simulations. For more information on this phenomenon see [Cramer, 2001; Vlad, Zonca, and Briguglio, 2008; Chen and Hasegawa, 1974].

6.2.3 Global Alfvén Eigenmode

In case the Alfvén continuum, given by the Eq. (6.32), has a minimum in its spectrum (for instance due to a non-uniform density $\rho_0(r)$), a new type of mode appears just below the Alfvén continuum minimum, the so-called Global Alfvén Eigenmode (GAE). To analytically describe the Global Alfvén Eigenmode we present here the analysis made by Villard and Vaclavik, 1997, which perfectly suits the plasma model (ideal MHD model) and configuration (cylindrical geometry) we are interested in this Thesis.

Let's start considering a toroidal axis-symmetric plasma that we assume to be in an ideal magnetohydrodynamic (MHD) equilibrium configuration with nested flux surfaces

labelled with the variable ψ. Let us define $\mathbf{e}_\parallel = \mathbf{B}_0/B_0$, $\mathbf{e}_n = \nabla\psi/|\nabla\psi|$, $\mathbf{e}_b = \mathbf{e}_\parallel \times \mathbf{e}_n$. The electromagnetic oscillations are described by the variational form

$$\int_{V_p} \left\{ \left|\nabla\times\mathbf{E} - \mathbf{J}E_b\right|^2 - 2\mathbf{J}\cdot\nabla_\parallel\mathbf{e}_n|E_b|^2 - \frac{\omega^2}{c^2}\mathbf{E}^*\cdot\begin{pmatrix}\epsilon_{nn} & \epsilon_{nb}\\ \epsilon_{bn} & \epsilon_{bb}\end{pmatrix}\cdot\mathbf{E}\right\}\mathrm{d}^3x + \\ + \int_{V_v}\left|\nabla\times\mathbf{E}\right|^2\mathrm{d}^3x = 0, \tag{6.45}$$

where $\mathbf{J} = (\mu_0\mathbf{j}_0\times\mathbf{e}_n)/B_0$, $\mathbf{j}_0$ is the equilibrium current, V_p and V_v are the plasma and vacuum volumes respectively, and

$$\epsilon_{nn} = \epsilon_{bb} = \frac{c^2}{v_A^2}\sum_i \frac{f_i}{1-(\omega/\omega_{ci})^2} \tag{6.46a}$$

$$\epsilon_{nb} = \epsilon_{bn}^* = i\frac{c^2}{v_A^2}\sum_i \frac{f_i(\omega/\omega_{ci})}{1-(\omega/\omega_{ci})^2} \tag{6.46b}$$

$$f_i = \frac{n_i m_i}{\sum_j n_j m_j}. \tag{6.46c}$$

The plasma is surrounded by a vacuum region V_v, enclosed by a perfectly conducting wall. This model includes finite ω/ω_{ci}, and, in the limit $\omega/\omega_{ci}\to 0$, is equivalent to linearized full ideal MHD in the approximation of $\gamma p\to 0$, where γ is the adiabaticity index and p is the plasma pressure. There are no limiting assumptions on the ratio of the poloidal to the toroidal components of the magnetic field. There are no geometrical expansions or simplifications.

In order to obtain approximate dispersion relations with analytical means we model the toroidal axis-symmetric plasma of major radius R by a cylindrical, circular, current carrying plasma column of periodicity $2\pi R$. In general both $B_{0\theta}$ and B_{0z} are functions of the radial coordinate r. The equations for the low frequency oscillations in the ideal MHD model limit ($\omega/\omega_{ci}\to 0$) can be written as

$$\frac{\mathrm{d}}{\mathrm{d}r}\left(\frac{AB_0^2}{A-k_b^2}\frac{1}{r}\frac{\mathrm{d}}{\mathrm{d}r}(r\xi_r)\right) + \\ + \left[AB_0^2 - \frac{r}{R^2}\frac{\mathrm{d}}{\mathrm{d}r}\left(\frac{B_{0z}^2}{q^2}\right) - \frac{4n^2B_{0z}^2}{R^4q^2(A-k_b^2)} + r\frac{\mathrm{d}}{\mathrm{d}r}\left(\frac{2nk_bB_0B_{0z}}{R^2qr(A-k_b^2)}\right)\right]\xi_r = 0, \tag{6.47}$$

with

$$q = \frac{rB_{0z}}{RB_{0\theta}} \tag{6.48}$$

the safety factor (defined in (2.10)), and

$$k_\parallel = \frac{B_{0z}}{B_0R}\left(n+\frac{m}{q}\right) \tag{6.49}$$

$$k_b = \frac{B_{0z}}{B_0}\left(\frac{m}{r}-\frac{nr}{qR^2}\right) \tag{6.50}$$

$$A = \frac{\omega^2 - \omega_A^2}{v_A^2} \tag{6.51a}$$

$$\omega_A^2 = v_A^2 k_\parallel^2 \tag{6.51b}$$

$$v_A^2 = \frac{B_0^2}{\mu_0 \rho_0}, \tag{6.51c}$$

where n and m are as usual the toroidal and poloidal mode numbers, ξ_r is the plasma radial displacement and $\rho_0 = \rho_0(r)$ is the mass density. Equation (6.47) is equivalent to Eq. (6.45) in the limit of large aspect ratio and small ω/ω_{ci}. It is important to point out that no approximation on the smallness of $B_{0\theta}/B_{0z}$ has been made in the derivation of Eqs. (6.45) and (6.47).

Equation (6.47) describes two types of wave: a continuum, which we have already discussed, and a discrete set of eigenmodes called the GAEs. The existence of GAEs can be demonstrated by carrying out a Wentzel-Kramers-Brillouin (WKB) analysis of Eq. (6.47). We obtain

$$\omega^2 = \omega_A^2 - \frac{1}{\mu_0 \rho_0 k_r^2}\left[\left(\frac{2B_{0z}n}{qR^2}\right)^2 - k_b^2 \frac{r}{R^2}\frac{\mathrm{d}}{\mathrm{d}r}\left(\frac{B_{0z}^2}{q^2}\right)\right]. \tag{6.52}$$

For $n = 0$, we have then

$$k_r^2 = \frac{(-1/\mu_0\rho_0)}{\omega_A^2 - \omega^2}\frac{B_{0z}^2}{B_0^2}\frac{m^2}{r}\frac{1}{R^2}\frac{\mathrm{d}}{\mathrm{d}r}\left(\frac{B_{0z}^2}{q^2}\right). \tag{6.53}$$

For a plasma of finite size (radius a) the quantization condition

$$\int_0^a k_r \mathrm{d}r = j\pi \qquad \text{with} \quad j = 1, 2, 3\ldots \tag{6.54}$$

gives a discrete spectrum of eigenfrequencies of the Alfvén wave.

We can rewrite the Eq. (6.53) as

$$k_r^2 = -\frac{B_{0z}^2}{B_0^2}\frac{1}{r}\frac{1}{\triangle}\left(\frac{\mathrm{d}}{\mathrm{d}r}\ln(\omega_A^2) + \frac{\mathrm{d}}{\mathrm{d}r}\ln\rho_0\right), \tag{6.55}$$

where

$$\triangle \equiv \frac{\omega_A^2 - \omega^2}{\omega_A^2} \tag{6.56}$$

is the frequency separation between the GAEs and the continuum.

Putting together Eqs. (6.55) and (6.54) and after a few steps we obtain the following condition:

$$\int_0^a \left[-\frac{\omega_A^2(r)}{\omega_A^2(r) - \omega_j^2}\frac{B_{0z}^2}{B_0^2}\frac{1}{r}\left(\frac{\mathrm{d}}{\mathrm{d}r}\ln(\omega_A^2(r)) + \frac{\mathrm{d}}{\mathrm{d}r}\ln\rho_0(r)\right)\right]^{1/2} \mathrm{d}r = j\pi \qquad \text{with} \quad j = 1, 2, 3\ldots \tag{6.57}$$

with the following constrain on ω_j^2 values

$$\omega_j^2 < \omega_A^2(r) \quad \forall r \in [0, a]. \tag{6.58}$$

The values of the frequencies ω_j can be derived then via numerical calculation, in analogous way as for the CAEs in nonuniform plasmas we discussed before. That is searching for the values of ω_j for which the conditions (6.57) and (6.58) are satisfied.

Keeping in mind the Eq. (6.49), for n=0 we can write the continuum frequency as

$$\omega_A^2(r) = \frac{B_{0z}^2(r) m^2}{\mu_0 \rho_0(r) q^2(r) R^2}. \tag{6.59}$$

Let's analyze the case we are interested in, that is when $\omega_A^2(r)$ has a local extremum at $r = r_c \neq 0$. This means that

$$\frac{\mathrm{d}}{\mathrm{d}r}\left(\frac{B_{0z}^2}{q^2\rho_0}\right)\bigg|_{r=r_c} = 0. \tag{6.60}$$

Defining $x \equiv r - r_c$ and looking for solutions of the type $\xi_r = x^\alpha$, the characteristic equation can be written as

$$\alpha^2 + \alpha - g = 0 \tag{6.61a}$$

$$g = -\frac{2}{r}\frac{B_{0z}^2}{B_0^2}\frac{\mathrm{d}(\ln\rho_0)/\mathrm{d}r}{\mathrm{d}^2(\ln\omega_A^2)/\mathrm{d}r^2}. \tag{6.61b}$$

If the discriminant of Eqs. (6.61) is negative then there exists an oscillatory solution in the vicinity of $r = r_c$ and the extremum of the continuum is an accumulation point of a discrete spectrum, whose frequencies ω_j are given by the condition (6.57). The sufficient condition for this is $g > 1/4$.

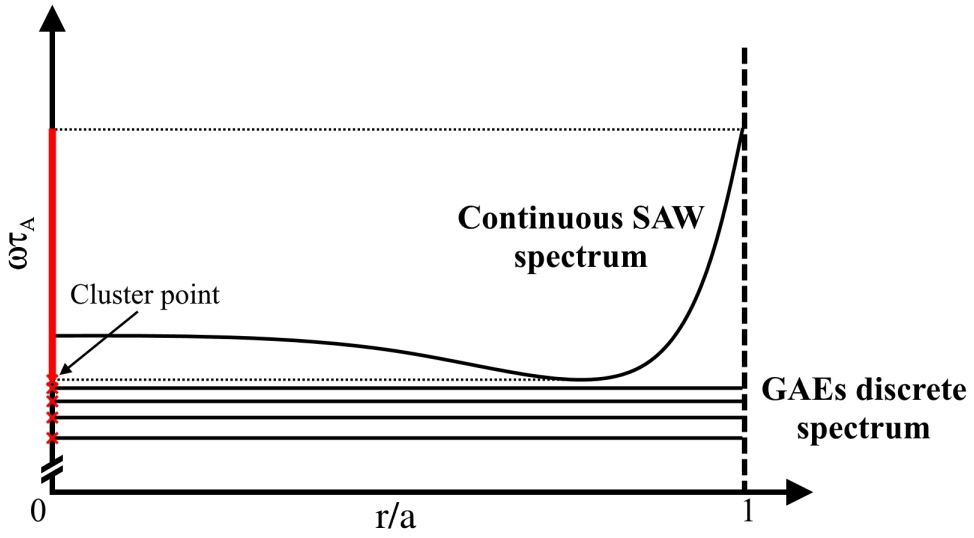

Figure 6.2: Schematic diagram of GAEs discrete spectrum and continuous SAW spectrum in the cylindrical plasma. The *red line* represents the continuous spectrum and *red crosses* show the discrete spectrum.

Standing wave structure

It has to be noted that because of the condition (5.6), in all SpeCyl simulations analyzed in the following chapters, all of the Alfvén modes previously computed have a standing wave structure as the perturbed velocity field **v** (for simplicity we omit the subscript 1) and magnetic field **B** are a superposition of two couples of mode numbers (m,n) with opposite signs that satisfies such condition. We can easily show this by considering the perturbed velocity field as a superposition of two such modes: for example one with $(m,n) = (0,1)$ Fourier component and the other with $(m,n) = (0,-1)$. Choosing $\mathbf{v} = \mathbf{v}_{01} + \mathbf{v}_{0-1}$ and using the expression (6.7) we have

$$\begin{aligned}\mathbf{v}(r) &= \mathbf{v}_{01}(0)\left[e^{i(\frac{1}{R}z-\omega_1 t)} + e^{i(\frac{1}{R}z+\omega_1 t)}\right] \\ &= \mathbf{v}_{01}(0)e^{i\frac{z}{R}}\left[e^{-i\omega_1 t} + e^{i\omega_1 t}\right] \\ &= \mathbf{v}_{01}(0)e^{i\frac{z}{R}}\cos(\omega_1 t),\end{aligned} \tag{6.62}$$

where ω_1 is the frequency of shear Alfvén or compressional mode with the toroidal and poloidal mode numbers $n = 1$ and $m = 0$. Thus we obtained a standing wave solution. An analogous consideration applies to **B**.

For GAE case we can see that Eq. (6.47) is invariant under the couples of mode numbers (m,n) that satisfies the condition (5.6). This means that for any given eigenfrequency the eigensolution is a superposition of two such modes and the GAE will also have a standing wave structure.

Chapter 7

Analysed configurations and expected solutions

To study and characterize Alfvén modes in nonlinear MHD simulations, in this Thesis we considered configurations with increasing complexity: from a purely axial uniform magnetic field, through a non-uniform RFP-like field, up to a "realistic" RFP configuration with time-varying, zero-order magnetic field in the presence of magnetic reconnection events.

In this Chapter we will list, in order of increasing complexity, all the magnetic configurations that were considered in nonlinear MHD simulations whose results are discussed in the next Chapter. For each configuration we will show the equilibrium (mean-field) magnetic field and density profiles. In addition, we will discuss the expected Alfvén wave solutions for selected (m,n) modes, according to the theoretical models developed in Chapter 6. Such theoretical solutions will prove to be a powerful tool to interpret and understand the results of nonlinear simulations discussed in Chapter 8.

7.1 Equilibrium configuration with uniform axial magnetic field

In this section we consider the simplest magnetic configuration analysed, that is a uniform equilibrium magnetic field in the axial direction z (see Figure 7.1 with field components normalized to the B_0 on the axis, as done in SpeCyl). We will see two configurations which differ for the radial density profile: one with an uniform equilibrium density $\rho_0 = 1$, the other with an RFX-mod-like hollow density $\rho_0(r)$ profile, shown in Figure 7.3, which is qualitatively similar to the density profile in RFX-mod RFP experiments at high plasma current.

As discussed in Chapter 5, SpeCyl uses dimensionless quantities and consistently we have chosen to represent all the quantities in abscissa and ordinate, of all the following figures, in dimensionless units. Furthermore since SpeCyl is a fully spectral code (as discussed in Section 5.1.2) we are able to select independently the Fourier modes (m,n)

to be included in the simulation accordingly to our needs. Therefore, except for the "realistic" case, to characterize the Alfvén modes we will always analyse simulations with one single mode, in particular with low mode numbers, which are the most interesting from the experimental point of view.

The first Fourier mode that we will consider is $(m,n) = (0,1)$ (with aspect ratio $R/a = 4$, that is $k_z a = na/R = 0.25$) because, as discussed in Chapter 6, this is the simplest mode that presents both SAW and CAE solutions.

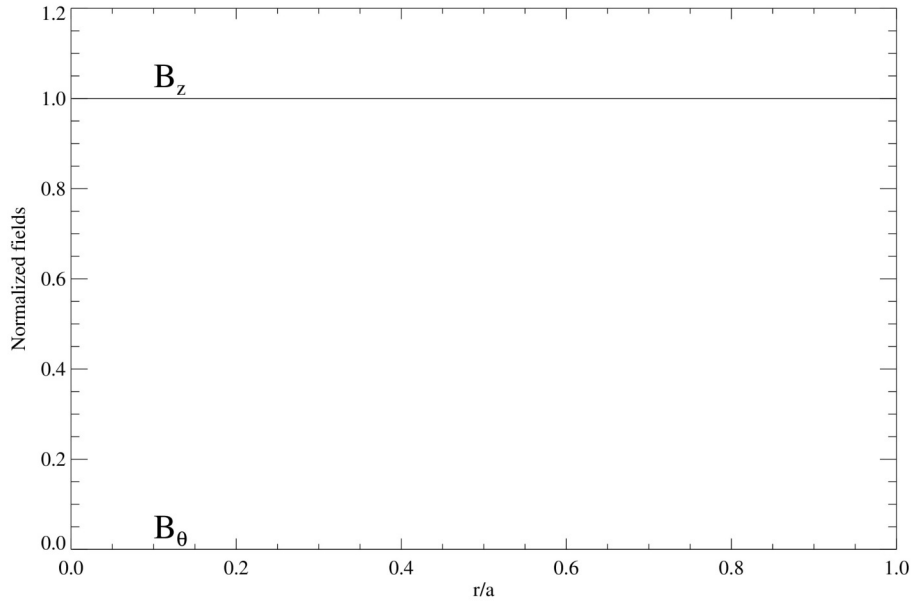

Figure 7.1: Radial profiles of the components of the normalized magnetic field $\mathbf{B}_0$ for the uniform equilibrium case.

7.1.1 Uniform density $\rho_0 = 1$

The first configuration we analysed was with all the uniform quantities, so that we could compare the simulation spectra with exact analytical predictions, discussed in Section 6.1, in the case of uniform plasma. The analytical dispersion relations to check are given by Eq. (6.8) and Eq. (6.22), respectively for the Shear Alfvén Wave and Compressional Alfvén Eigenmode. The corresponding frequencies as a function of the axial wavenumber are displayed for the m=0 case in Figure 6.1.

7.1.1.1 $(m,n) = (0,1)$ mode

The simplest mode that can present both SAW and CAE solutions is $(m,n) = (0,1)$. The expected frequency spectrum for this configuration is shown in Figure (7.2), where CAEs frequencies are given by Eq. (6.22), while the SAW is given by Eq. (6.8). For the sake of simplicity we will always consider the first three CAE. In particular only for this case we

also displayed the nodes on the compressional eigenmodes, i.e., the radial locations were the B_{1z} component of the compressional mode do not oscillate being equal to zero. These are due to the fact that the fields components depend on the Bessel functions, as can been seen from Eq. (6.19) for example for B_{1z} component, and in turn these functions become zero when their argument is equal to their roots. We can see for what radial coordinates r the Bessel function of order m goes to zero from the following condition:

$$\xi r = X_k^m \qquad \text{with} \quad k = 1, 2, 3 \ldots, \tag{7.1}$$

where ξ is given by Eq. (6.16) and X_k^m are the roots of the Bessel function of order m. To be noticed that there may be none, one or many indices k that satisfies this condition for a fixed ω_j and different r values. This means that different ω_j can present none, one or many nodes. Note also that the number of nodes in CAE modes increases with their harmonic number as can been seen from Figure 7.2.

In this case of uniform magnetic field $\mathbf{B}_0 = B_0\mathbf{z}$ and $(m,n) = (0,1)$, the resulting $\mathbf{k} = (0, k_\theta, k_z) = (0, m/r, n/R) = (0, 0, k_z)$ is parallel to the equilibrium field, and therefore either the SAW or the CAEs will be excited depending on the initial perturbed velocity component. Thus the frequency spectra of SAW and CAE won't appear together in the same component of magnetic field or velocity field.

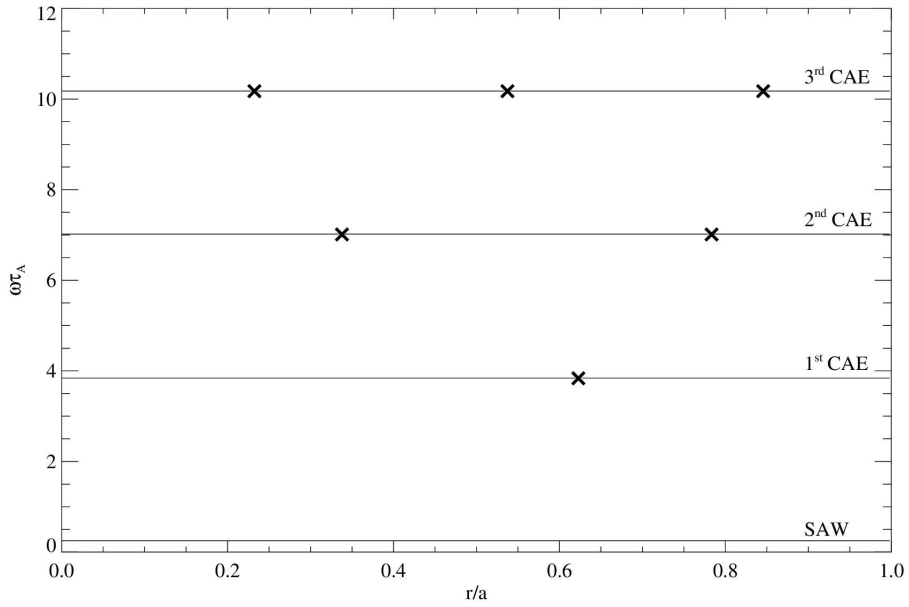

Figure 7.2: Uniform axial field configuration with uniform density. $(m,n) = (0,1)$ mode. Analytical frequency spectra for SAW and CAE modes. For CAEs, crosses locate the nodes of the B_{1z} perturbation component.

7.1.2 RFX-mod-like hollow density profile

Let us now complicate the analysed configuration, that is let's consider a variable plasma density. In particular we will consider a density profile typical of RFX-mod plasmas at high current, where a brawback of the increased core confinement is that core density fueling is more difficult, resulting in a hollow density profile. A typical RFX-mod-like hollow density profile is shown in Figure 7.3. This profile corresponds to the analytical fit:

$$\rho_0(r) = 1.0 + 2.12r^{5.0} - 3.12r^{8.5} + 0.1r^{100.0}. \tag{7.2}$$

Unlike the previous case of uniform density, now the dispersion relation of CAEs can't be obtained analytically. Therefore the CAEs frequencies will be derived in WKB approximation through numerical calculation as discussed in Section 6.2.2. On the other hand, the SAW will now exhibit a continuous spectrum given by Eq. (6.32).

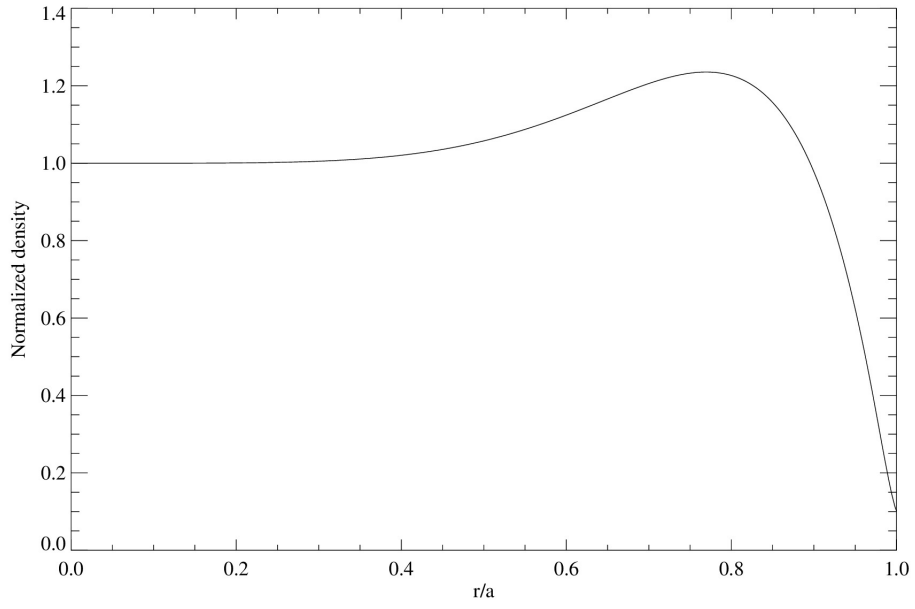

Figure 7.3: Normalized density profile used for the RFX-mod like hollow density case.

7.1.2.1 $(m,n) = (0,1)$ mode

Considering the same mode as in case of uniform density, $(m,n) = (0,1)$, we can see from Figure 7.4 that the expected frequency spectrum for CAEs, obtained in the WKB approximation from the condition (6.43) via numerical calculation, is almost identical to the one in Figure 7.2, obtained instead with CAEs analytical dispersion relation (6.22). This means that the radial dependence of this density profile doesn't change much the CAEs frequencies (and makes us confident of using the numerical calculation based on the WKB approximation).

On the other hand the SAW will now have a much different spectrum given by Eq. (6.32), as shown in Figure 7.4. Furthermore, as discussed in 6.2.1 we expect the frequency to be damped in time in the spatial regions where it has a gradient because of the phase mixing. We will verify this phenomenon in the next chapter by analyzing the evolution of the SAW amplitude in time.

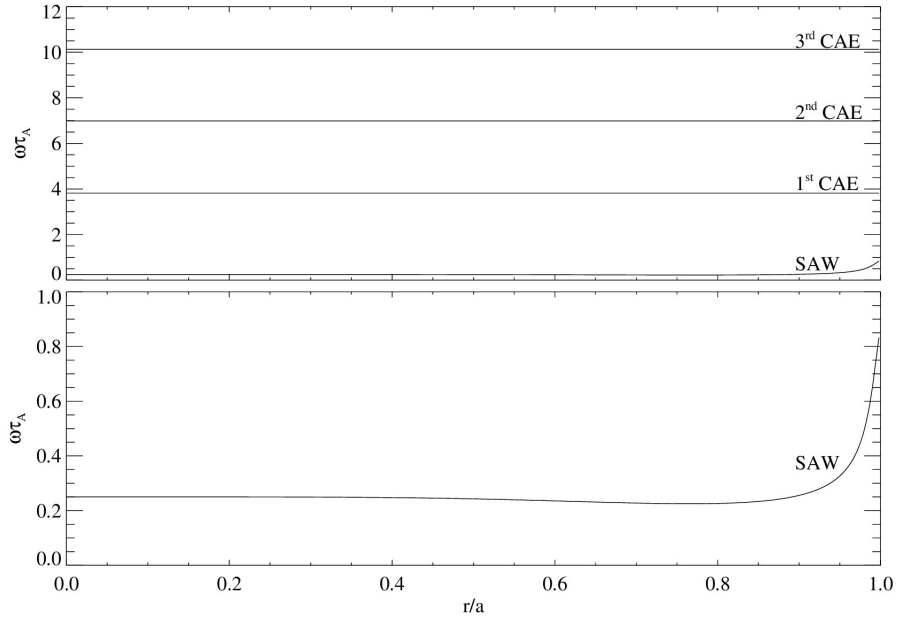

Figure 7.4: Uniform axial field configuration with hollow density profile. $(m,n) = (0,1)$ mode. (Top) Frequency spectra in WKB approximation for CAEs and analytical frequency spectrum for continuous SAW. (Bottom) Magnification of SAW spectrum.

7.2 Tokamak-like equilibrium configuration

Let us now consider a more complex case of slightly non-uniform magnetic field $\mathbf{B}_0(r)$ in a Tokamak like configuration shown in Figure 7.5. In this case, the axial magnetic field is still uniform, but a linearly increasing small azimuthal component is now included, which implies the presence of a small axial current. Furthermore with non-uniform magnetic field a coupling between the SAW and CAEs is expected, as mentioned in Section 6.2.1. For this magnetic configuration we will only consider the case with the uniform density ρ_0 since our aim here will be only to verify the coupling between SAW and CAEs and to investigate how a slightly non-uniform magnetic field can change the frequency spectrum of Alfvén modes.

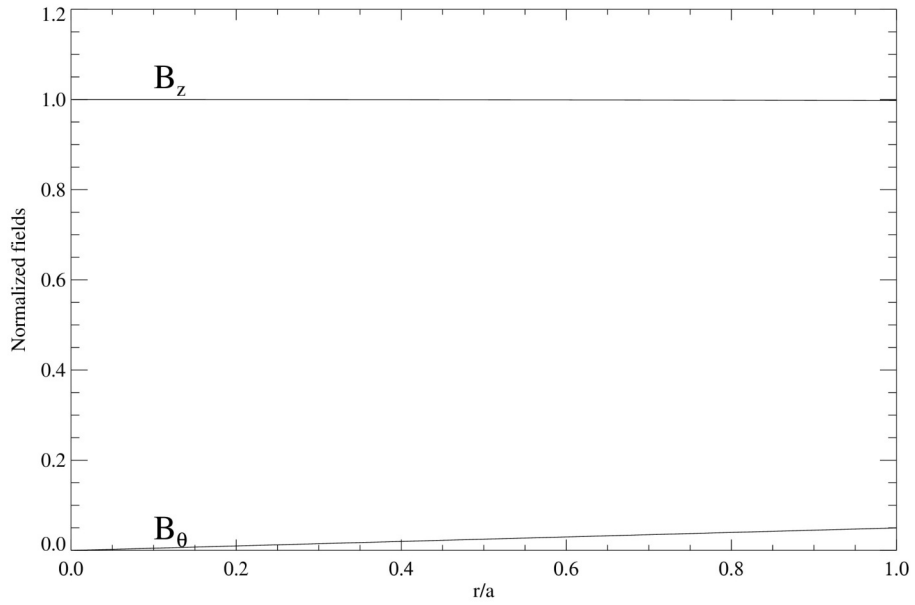

Figure 7.5: Radial profiles of the components of the normalized magnetic field $\mathbf{B}_0(r/a)$ for the tokamak-like equilibrium case.

We consider here again the Fourier mode $(m,n) = (0,1)$. The expected frequency spectrum for this magnetic configuration is shown in Figure 7.6, where CAEs frequencies are obtained in the WKB approximation from the condition (6.43) via numerical calculation while the continuous SAW spectrum is given by Eq. (6.32). The CAEs and SAW spectra are very similar to the uniform case shown in Figure 7.2. This was also a way to test the reliability of the numerical calculation based on the WKB approximation in the case of weakly variable magnetic field.

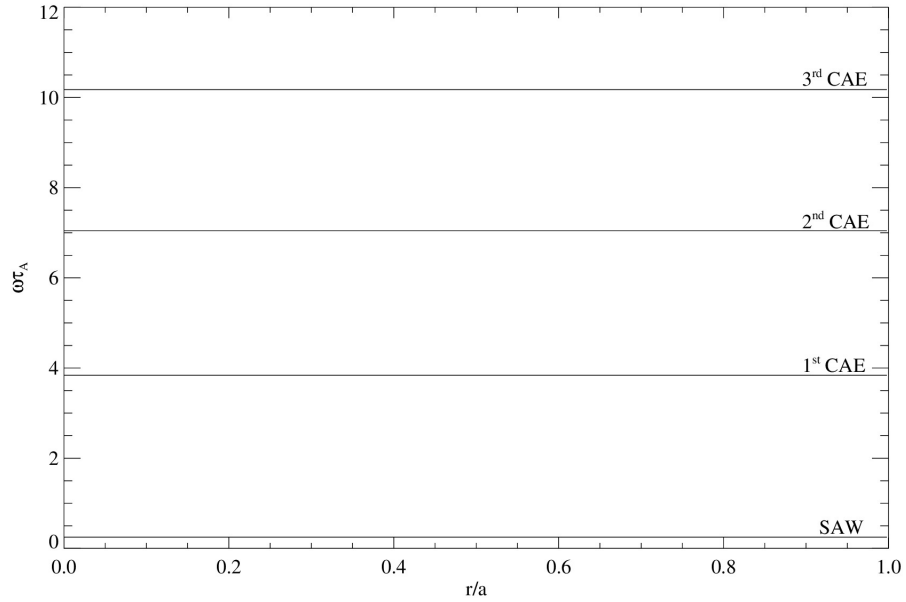

Figure 7.6: Tokamak-like configuration with uniform density. $(m,n) = (0,1)$ mode. Frequency spectrum in WKB approximation for CAEs and analytical frequency spectrum for continuous SAW.

7.3 "Academic" RFP-like equilibrium configuration

After having introduced the equilibrium configurations that will be used for a first basic assessment of Alfvén waves in MHD simulations (namely, uniform axial magnetic field and tokamak-like equilibrium), we now move the configurations that will be employed for the physical characterization of Alfvén waves in the RFP and the comparison with experimental observations in the RFX-mod device. In this Section we consider a first, simplified RFP-like case, that we dub "academic" RFP configuration. By "academic" we mean without the axial field reversal at the edge and, most importantly, with fixed equilibrium profiles. Indeed, this "academic" RFP configuration is a numerical solution of the 1D zero-β paramagnetic pinch equilibrium equations, discussed for instance in [Bonfiglio, Chacón, and Cappello, 2010]. The lack of the axial field reversal at the edge is just a mathematical consequence of the 1D equilibrium assumption, also known as Cowling's theorem (see also [Escande et al., 2000b]). The specific RFP-like equilibrium used in this Thesis is shown in Fig. 7.7. It corresponds to a paramagnetic pinch equilibrium with aspect ratio $R/a = 4$, uniform resistivity and $\alpha_0 = 3.25$ (the parameter α_0 is defined in [Bonfiglio, Chacón, and Cappello, 2010] and corresponds to the ratio between the applied induction electric field and the central resistivity).

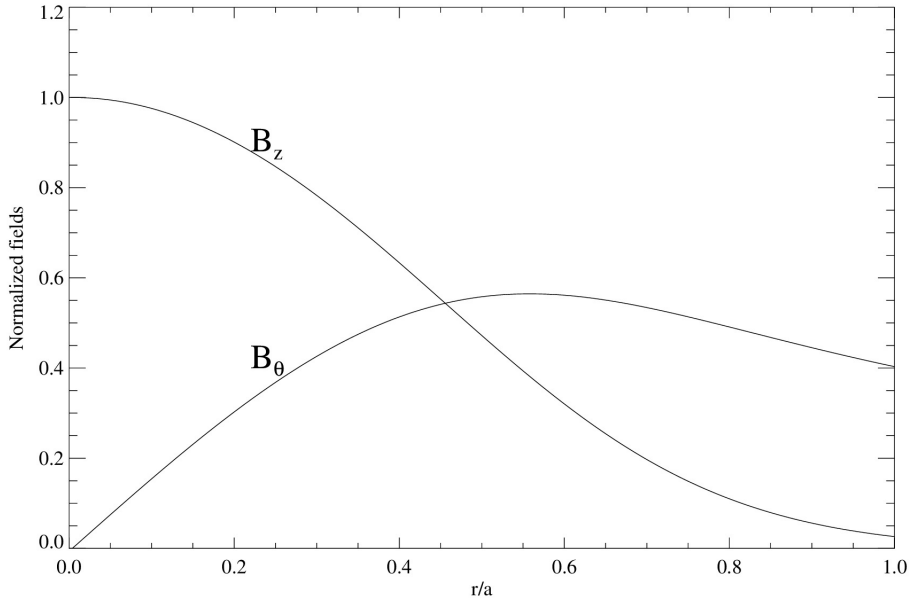

Figure 7.7: Radial profiles of the magnetic field components of the "academic" RFP-like equilibrium configuration.

7.3.1 Uniform density $\rho_0 = 1$

7.3.1.1 $(m,n) = (1,0)$ mode

From now on we will mostly focus on the $(m,n) = (1,0)$ mode as experimentally it is the Fourier component with the strongest Alfvénic activity, and also because this mode is the most excited by Alfvén waves in "realistic" RFP simulations, as we will see in the next Chapter.
The expected frequency spectrum for this configuration is shown in Figure 7.8, where CAEs frequencies are obtained in the WKB approximation from the condition (6.43) via numerical calculation while the continuous SAW is given by Eq. (6.32). With respect to the previous magnetic configurations, now the SAW frequency range increases while the CAE frequencies are shifted down, so that a very peculiar condition occurs in which the SAW and the 1^{st} CAE intersect each other. Instead in the uniform and tokamak cases, as seen previously, the SAW and the CAE are well separated in frequency. This is the reason why in the tokamak the CAEs are considered of little importance and are decoupled from the shear mode.
As discussed in 6.2.1 we expect the SAW frequency to be damped in time in the spatial regions where it has a frequency gradient because of the phase mixing. We will verify this phenomenon in the next chapter by analyzing the evolution of the SAW frequency spectrum in time. In this case we would also expect, as discussed in 6.2.2, to see the Alfvén resonance absorption of the 1^{st} CAE since its frequency is equal to that of the

Alfvén resonance condition (6.32) in a radial position, around $r/a = 0.5$. However, as we will see in the next chapter, the damping of the 1^{st} CAE is absent in this case of uniform density ρ_0, although it will be indeed found in the case of variable density profile.

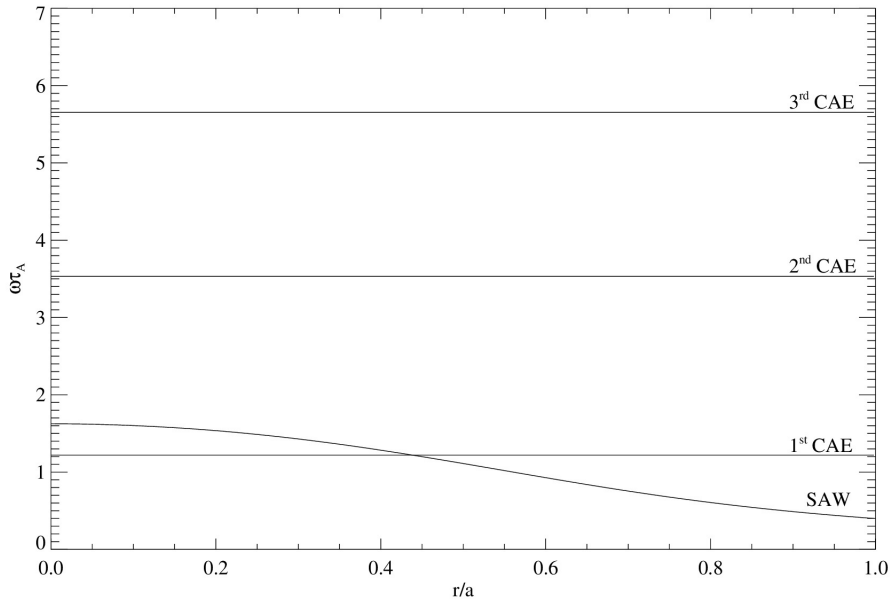

Figure 7.8: RFP-like configuration with uniform density. $(m,n) = (1,0)$ mode. Frequency spectrum in WKB approximation for CAEs and analytical frequency spectrum for continuous SAW.

7.3.2 RFX-mod-like hollow density profile

7.3.2.1 $(m,n) = (1,0)$ mode

Let us now consider the same simulation with $(m,n) = (1,0)$ mode but RFX-mod-like hollow density profile. As shown in Figure 7.9, we expect a very similar frequency spectrum but with a qualitative difference: now the Alfvén continuum has a minimum around $r/a = 0.9$. As a consequence, we would expect a new mode to show up below the frequency minimum, the Global Alfvén Eigenmode (GAE) discussed in Section 6.2.3. The GAE frequency spectrum is obtained from the condition (6.57) via numerical calculation. It's important to note that with the equilibrium magnetic field configuration and density profile here examined the GAE spectrum, which in general is characterized by a discrete spectrum of frequencies with the Alfvén continuum minimum as an accumulation point, is given by a single discrete mode very close to the minimum. However, as we will see in the

next chapter, nonlinear MHD simulations for this equilibrium case showed a rather weak GAE signal. To investigate this, as we will discuss below, we analysed several different density profiles in order to see if we could better excite the GAE mode.
In this case however, compared to the previous with uniform density, we did observe the resonance absorption process by looking the time evolution of the frequency spectrum.

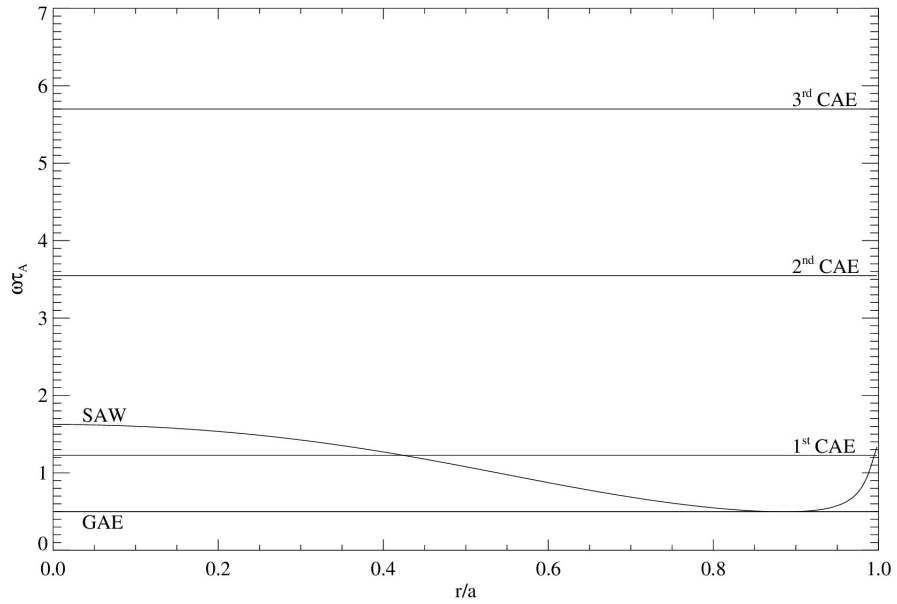

Figure 7.9: RFP-like configuration with hollow density profile. $(m,n) = (1,0)$ mode. Frequency spectrum in WKB approximation for CAEs and GAE, and analytical frequency spectrum for continuous SAW.

7.3.2.2 $(m,n) = (0,2)$ and $(m,n) = (4,4)$ modes

To further investigate the phenomenon of resonance absorption we analysed two cases: one with the Alfvén continuum below the 1^{st} CAE ($(m,n) = (0,2)$ mode), the other with the Alfvén continuum crossing the 1^{st} and the 2^{nd} CAE ($(m,n) = (4,4)$ mode). In the first case we don't expect to see the resonance absorption process, in the second one we expect the first two CAEs to be damped in time as both of them have their frequency equal to that of Alfvén resonance condition (6.32) in some radial position. These theoretical expectations will be confirmed by numerical results discussed in the next Chapter. The expected spectra for the two selected modes are shown below, see Figures 7.10 and 7.11.

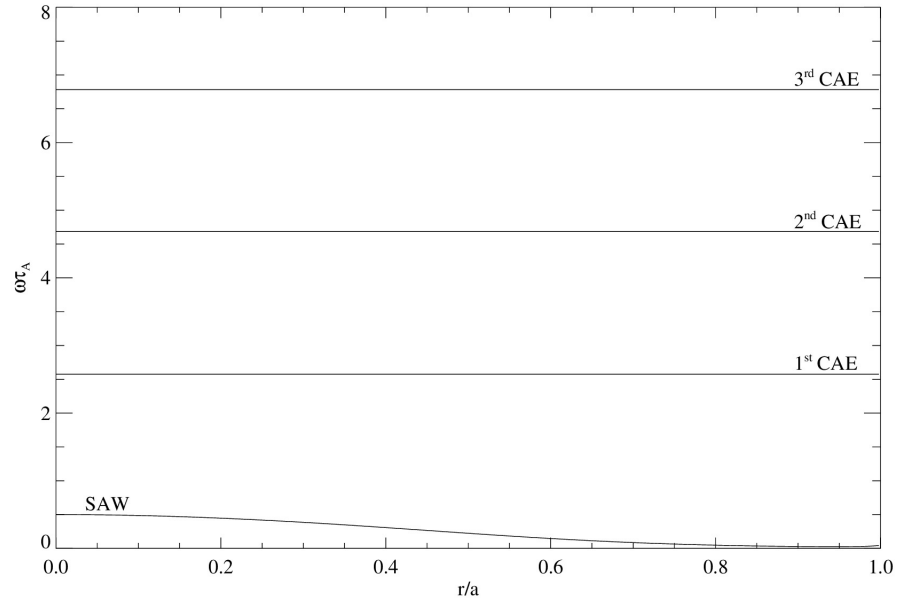

Figure 7.10: RFP-like configuration with hollow density profile. $(m,n) = (0,2)$ mode. Frequency spectrum in WKB approximation for CAEs and analytical frequency spectrum for continuous SAW.

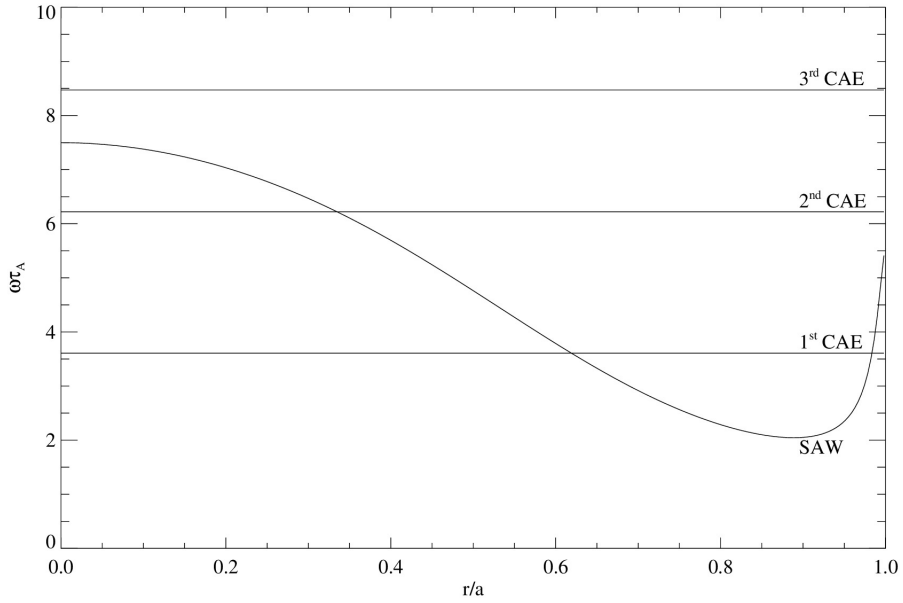

Figure 7.11: RFP-like configuration with hollow density profile. $(m,n) = (4,4)$ mode. Frequency spectrum in WKB approximation for CAEs and analytical frequency spectrum for continuous SAW.

7.3.3 Center-peaked density profile

In order to try to better excite the GAE mode and see its qualitative relation with the profile of the equilibrium density we analysed the same Fourier mode as before, $(m,n) = (1,0)$, with five different density $\rho_0(r)$ profiles shown in Figure 7.12. In particular we considered density profiles with different radial locations of their peak density, moving it from the wall to the center of the cylinder. Note that the (d) profile is the RFX-mod-like hollow density profile from Figure 7.3.
In the next chapter we will analyse the density profile that results in the strongest excitation of the GAE mode, that is the central peaked density profile (a) which analytical expression is:

$$\rho_0(r) = 1.2 - 1.2r^{2.0} + 0.1r^{100.0}. \tag{7.3}$$

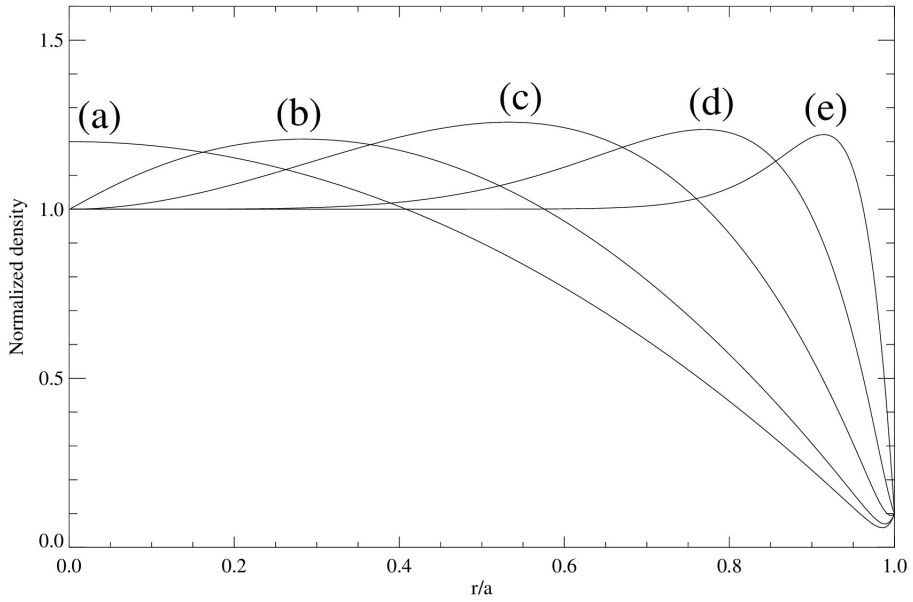

Figure 7.12: Different profiles of normalized density $\rho_0(r/a)$.

7.3.3.1 $(m,n) = (1,0)$ mode

The expected frequency spectrum for $(m,n) = (1,0)$ mode with central peaked density profile (marked as (a) in Figure 7.12) is shown in Figure 7.13, where CAEs frequencies are obtained in the WKB approximation from the condition (6.43) via numerical calculation, GAE frequency value is obtained from the condition (6.57) also via numerical calculation and the continuous SAW spectrum is given by Eq. (6.32). Compared to the RFX-mod-like

density profile case, now the CAEs are higher in frequency, while the SAW turns out to be flatter. As a result the 1^{st} CAE and GAE are closer in frequency to each other. To note that while the density peak changed a lot its radial position, compared to the RFX-mod-like density case, shifting all the way to the center of the cylinder, the SAW minimum shifted only slightly toward the center. As already mentioned, this case with density profile peaked in the plasma core will prove in next Chapter to be the one where the GAE is most excited.

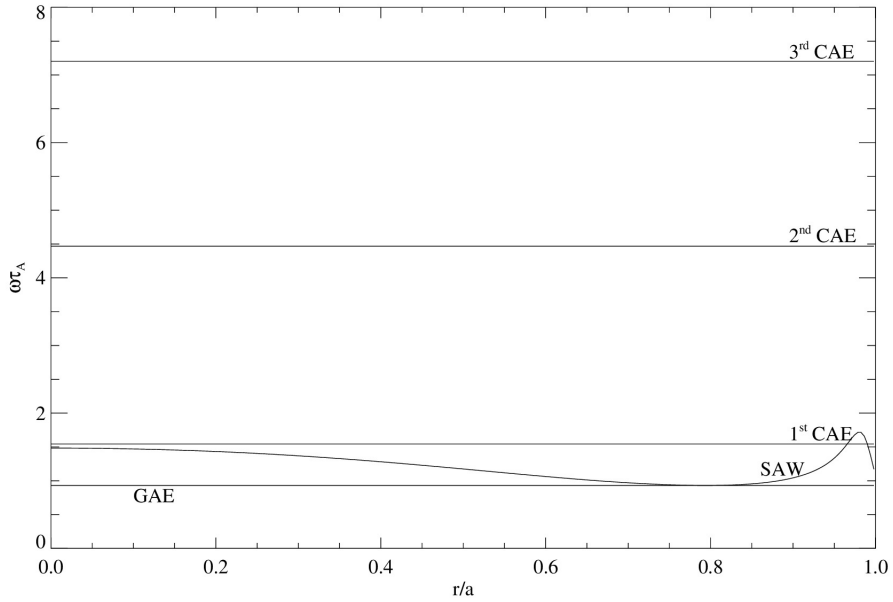

Figure 7.13: RFP-like configuration with center-peaked density profile. $(m,n) = (1,0)$ mode. Frequency spectrum in WKB approximation for CAEs and GAE, and analytical frequency spectrum for continuous SAW.

7.4 "Realistic" time-evolving RFP configurations

The most advanced case, that we will consider in this Thesis, is a “realistic” RFP dynamical configuration, where with “realistic” we mean the closest to the experimental conditions we can presently achieve with the SpeCyl code. Such realistic conditions include time-evolving mean-field $\mathbf{B}_0$ profiles[1] with quasi-periodic magnetic reconnection events triggered by nonlinear bursts of global MHD instabilities, as described in the modeling study of QSH states in the RFP configuration [Bonfiglio et al., 2013] (and briefly recalled in Section 5.2). We will consider simulations with two different density profiles: one with uniform density profile, the other with a RFX-mod-like hollow density profile. These simulations will be used in the next Chapter to try to explain from a theoretical point of view the experimental observation of Alfvén Eigenmodes in RFP plasmas, which we discussed in Section 3.3.

All the simulations of this Section are based on the simulation with uniform density profile reported in Figure 5.2, and here in Figure 7.14.

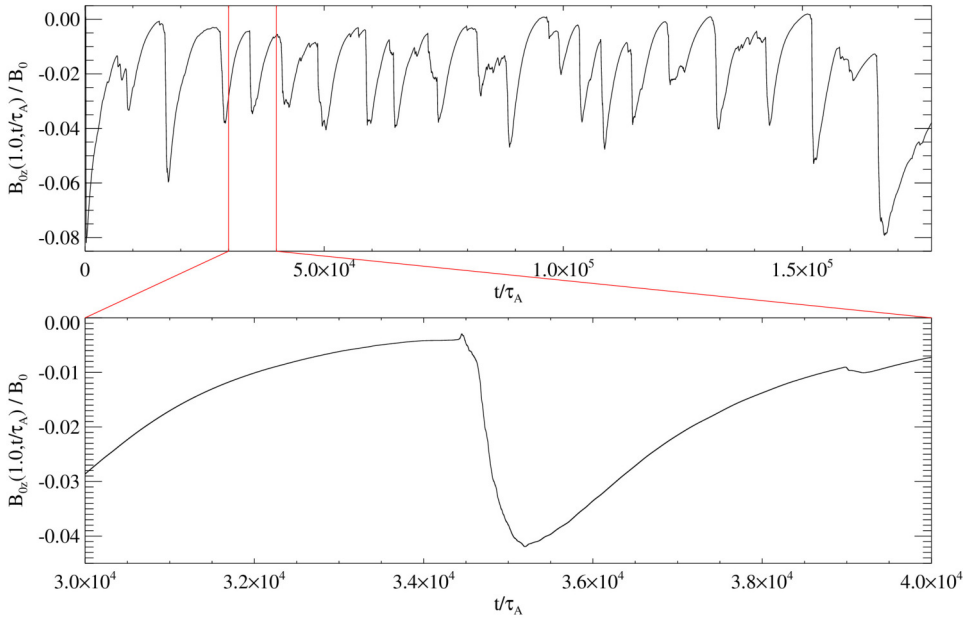

Figure 7.14: “Realistic” RFP configuration with uniform density. Profile of the component $B_{0z}(r/a,t/\tau_A)$ of the magnetic field $\mathbf{B}_0(r/a,t/\tau_A)$ as a function of normalized time t/τ_A at a fixed radius $r/a = 1.0$.

As already mentioned, this simulation is characterized by a quasi periodic repetition of magnetic reconnection events. Therefore, to qualitatively characterize the dynamics of

[1]Note that in this case the subscript 0 doesn't stand for the stationary equilibrium component of the magnetic field, as in these simulations the mean magnetic field $\mathbf{B}_0$ is time evolving. However, such mean field is still changing much slowly than the evolution of Alfvén waves, and therefore it can be used as before for theoretical predictions of the Alfvén modes frequency spetrum.

Alfvén modes, it is sufficient to focus on a single dynamical cycle. In this Thesis we have chosen to focus on the time window, centered around a magnetic reconnection event, from $t = 3\times10^4\ \tau_A$ to $t = 4\times10^4\ \tau_A$. The mean magnetic field profiles at several times along the selected time window are displayed in Figure 7.15. It should be noted that unlike in the "academic" case, now we have the reversal of the axial component of the mean magnetic field on the edge, which is the distinctive feature of the RFP configuration.

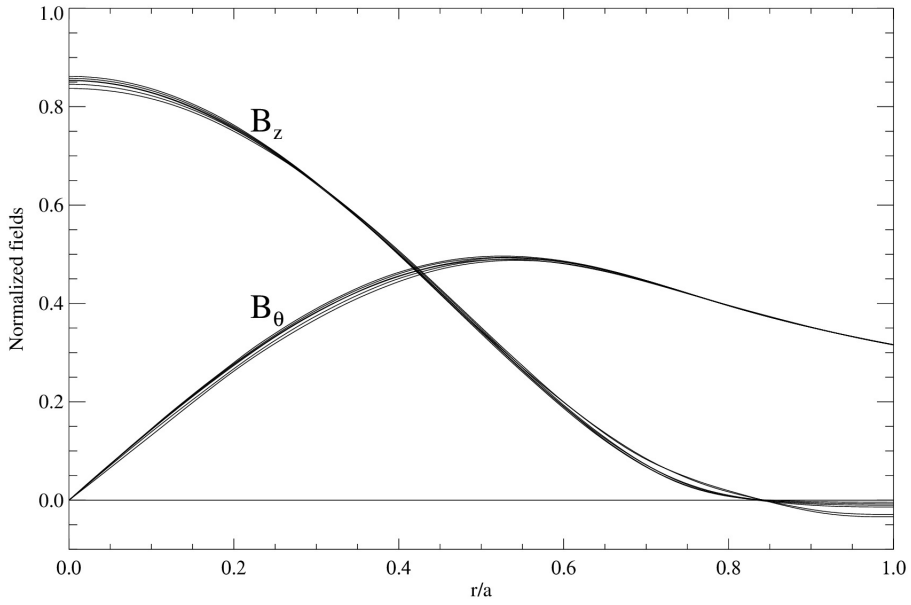

Figure 7.15: Radial profiles of the components of the normalized mean magnetic field $\mathbf{B}_0$ at several times along the time window centered around a magnetic reconnection event that was chosen for the characterization of Alfvén modes in "realistic" RFP conditions.

7.4.1 Uniform density $\rho_0 = 1$

First we consider the case with uniform density profile. The nonlinear MHD simulation analyzed in this case is just a repetition, starting from $t = 3\times10^4\ \tau_A$, of the original uniform density simulation, with same MHD spectrum but with fields saved each $0,1\tau_A$ (a high sampling frequency suitable for the analysis of Alfvén times) instead of each $10\tau_A$ as in the original simulation. The time step is also reduced from $t = 5\times10^{-2}\ \tau_A$ to $t = 10^{-3}\ \tau_A$, and the semi-implicit term is turned off, to obtain a more accurate characterization of Alfvén modes. The temporal evolution of the safety factor on edge $q(a)$ and the normalized edge B_ϕ amplitudes of the most active $m = 1$ modes is shown in Fig. 7.16.
It's important to note that, unlike in all the previous cases, Alfvén modes in these simulations do not depend on specific details of the initial velocity perturbations. Indeed, we will see in the next Chapter that now each reconnection events provides a new velocity perturbation (produced self-consistently by the nonlinear MHD dynamics itself) that will trigger Alfvén modes in a quasi-periodic fashion.

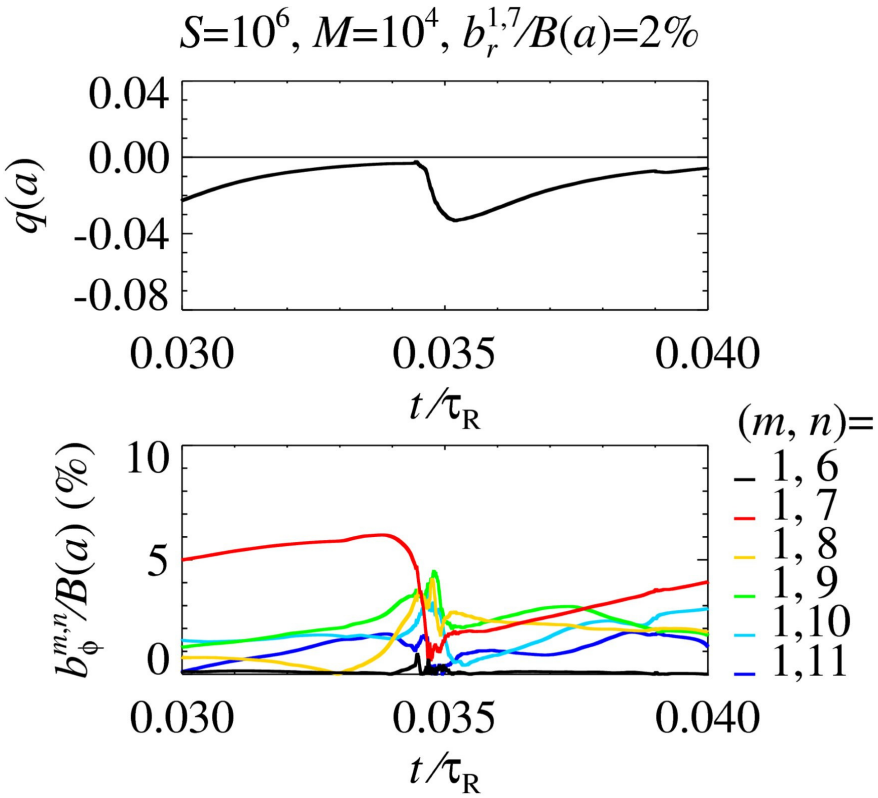

Figure 7.16: "Realistic" RFP configuration with uniform density. The temporal evolution of the simulation is centered around a magnetic reconnection event, from $t = 3\times10^4\ \tau_A$ to $t = 4\times10^4\ \tau_A$.

7.4.1.1 $(m,n) = (1,0)$ mode

As already mentioned the $(m,n) = (1,0)$ mode is the most excited one by Alfvén modes in this "realistic" simulations, as we will see in the next chapter, and so it's the one we will analyse here. The expected frequency spectrum is shown in Figure 7.17, where CAEs frequencies are obtained in the WKB approximation from the condition (6.43) via numerical calculation while the continuous SAW is given by Eq. (6.32)[2]. This spectrum appears qualitatively similar to the one in the "academic" RFP case with uniform density (Figure 7.8), and therefore that case will prove to be an important basis for the interpretation of this one.

[2]To compute the CAEs and SAW frequencies here we used the mean magnetic field profiles at the time of the magnetic reconnection event.

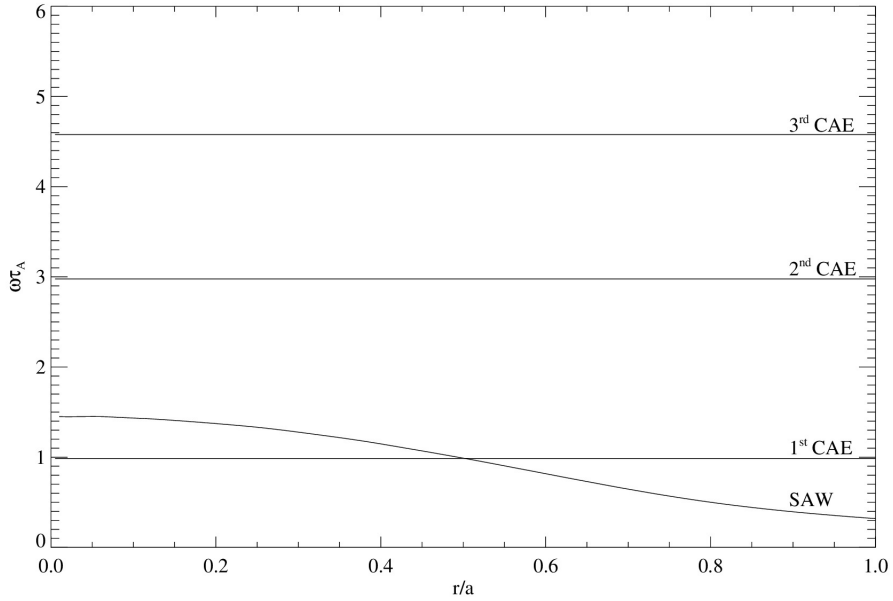

Figure 7.17: "Realistic" RFP configuration with uniform density. $(m,n) = (1,0)$ mode. Frequency spectrum in WKB approximation for CAEs and analytical frequency spectrum for continuous SAW.

7.4.2 RFX-mod-like hollow density profile

7.4.2.1 $(m,n) = (1,0)$ mode

The last analysed configurations was with a RFX-mod-like hollow density profile as experimentally the plasma density is a function of r and we want to obtain a frequency spectrum as close as possible to the experimental one discussed in Section 3.3 to try to identify the coherent peaks in the power spectrum of the magnetic fluctuation measured at the edge of the RFX-mod plasma.

In this case, the analyzed nonlinear MHD simulation starts from time $t = 3\times10^4\ \tau_A$ of the original uniform density simulation, but now the hollow density profile is imposed (together with reduced time-step and high sampling frequency as in the previous uniform density simulation for Alfvén modes). As an effect of the modified density profile, the nonlinear MHD dynamics is slightly different from the original simulation. Indeed, now the reconnection event around $t = 3.5\times10^4\ \tau_A$ is weaker, and a second much stronger reconnection event occurs around $t = 3.9\times10^4\ \tau_A$, as shown in Fig. 7.18. In the next Chapter, we will focus on a time window around this second reconnection event.

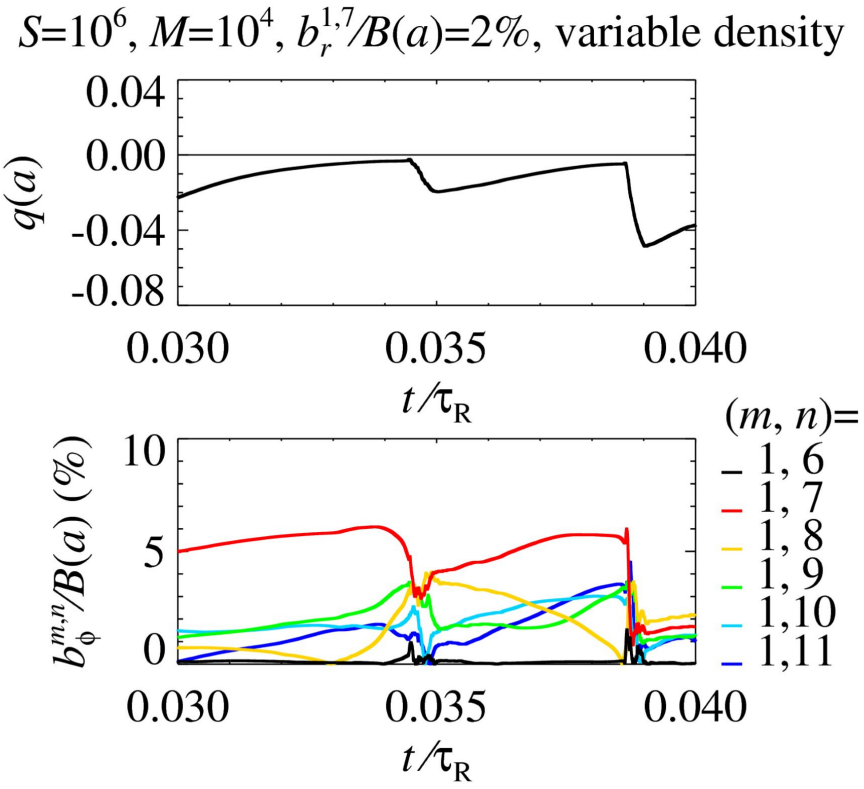

Figure 7.18: "Realistic" RFP configuration with hollow density profile. The temporal evolution of the simulation centered around a magnetic reconnection event, from $t = 3\times10^4\ \tau_A$ to $t = 4\times10^4\ \tau_A$.

The expected frequency spectrum is shown in Figure 7.19, where as usual CAEs frequencies are obtained in the WKB approximation from the condition (6.43) via numerical calculation, GAE frequency value is obtained from the condition (6.57) also via numerical calculation and the continuous SAW spectrum is given by Eq. (6.32). This spectrum also appears qualitatively similar to the one in the "academic" RFP case with RFX-mod-like density (Figure 7.9), and therefore that case will also be used as a basis for the interpretation of this one.

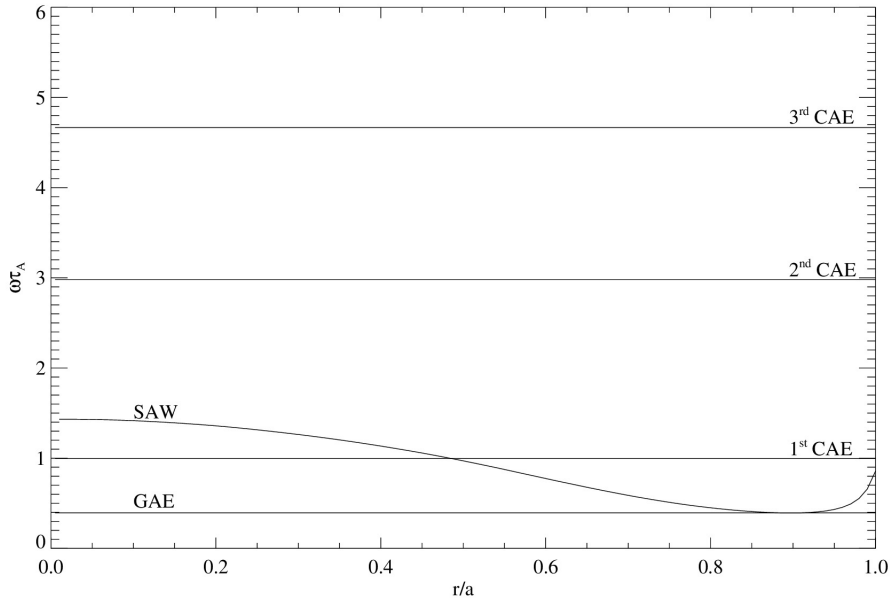

Figure 7.19: "Realistic" RFP configuration with hollow density profile. $(m,n) = (1,0)$ mode. Frequency spectrum in WKB approximation for CAEs and GAE, and analytical frequency spectrum for continuous SAW.

Chapter 8

Analysis of nonlinear MHD simulations and experimental comparison

In this Chapter we will analyze the results of nonlinear MHD simulations performed with the SpeCyl code, for the different magnetic configurations introduced in Chapter 7. We will consider simulations in configurations of increasing complexity: from a purely axial uniform magnetic field, through a non-uniform RFP-like magnetic field, up to a "realistic" RFP configuration with time-evolving mean magnetic field in the presence of the magnetic reconnection events. For each simulation case, we will test the presence of Alfvén waves and characterize their properties (such as frequency spectra and nonlinear dynamics) by computing the Fast Fourier Transform (FFT) of simulation data. In particular, FFTs are performed on time windows of $500\tau_A$. All the computed spectra will be compared with the expected ones shown in Chapter 7 which in turn were derived from the theoretical models discussed in Chapter 6. Finally, we will try to explain the experimentally observed Alfvén Eigenmodes in RFX-mod experiment through the analysis of "realistic" RFP simulations.

Except for the "realistic" case, for which we will specify the simulation parameters later, for all the other SpeCyl simulations we considered the ideal boundary conditions given by (6.14), aspect ratio $R/a = 4$, a radial resolution of 256 points and a single Fourier harmonic in the angular directions, with periodicity (m, n) to be specified for each simulation case. Lundquist number and Prandtl number were set to $S = 10^6$ and $P = 1$ respectively. The time-dependent magnetic and velocity field components computed by SpeCyl with a time step of $10^{-4}\tau_A$ are saved to disk every $0.1\tau_A$, and later the FFT in time of such fields is performed. Moving time windows of $500\tau_A$ are used for the FFTs, hence corresponding to 5000 time snapshots. The sampling rate of $0.1\tau_A$ and the time window of $500\tau_A$ are chosen to obtain temporal FFTs with good resolution and range of the resulting frequency spectra. On the other hand, a time window of $500\tau_A$ is not too long for the field components to change significantly within it.

8.1 Equilibrium configuration with uniform axial magnetic field

We start with the analysis of the most simple case, that is the equilibrium configuration with uniform axial magnetic field discussed in Section 7.1. We will first consider the case with uniform density and then with RFX-mod-like hollow density profile.

8.1.1 Uniform density $\rho_0 = 1$

8.1.1.1 $(m,n) = (0,1)$ mode with initial v_θ perturbation

In all the following simulations (except for the “realistic" RFP cases) the Alfvén waves are excited starting from a stable equilibrium configuration by applying a small initial perturbation to the velocity field. This can be intuitively understood with the analogy of plucking a string originally at rest, giving it an initial speed different from zero and letting it evolve in time.
However, it is important on which component of the magnetic field or velocity field the initial perturbation, which excites the Alfvén modes, is applied. This is especially true when the Alfvén modes SAW and CAEs are uncoupled as in this case of uniform magnetic field. In fact, depending on which component (r,θ,z) of the field is perturbed, it is possible to excite separately the SAW or CAEs, as can be deduced from the theoretical model discussed in Section 6.1. Therefore for all the analyzed modes (m,n) we will consider two separate simulations, one with initial v_θ perturbation, the other with initial v_r perturbation.

Let’s start discussing the simulation with uniform density and initial velocity perturbation on the azimuthal component v_θ, with radial profile given by

$$v(r) = \varepsilon r(1-r), \tag{8.1}$$

where $\varepsilon \ll 1$.

Let’s first look at the overall trend of the simulation, shown in Figure 8.1. We observe that by perturbing the v_θ component, only the b_θ and perturbed v_θ components are finite, and evolve in time by slowly decaying. Which component is excited by the initial perturbation depends on the MHD relations between $\mathbf{B}_1$ and $\mathbf{v}_1$ and fields configuration. The decaying in time of the fields is due to, as we already mentioned, the SpeCyl code being a visco-resistive numerical code, with viscosity and resistivity expressions given by Eqs. (5.2). These terms introduce a damping of the amplitude of the fields, making them to decay in time.

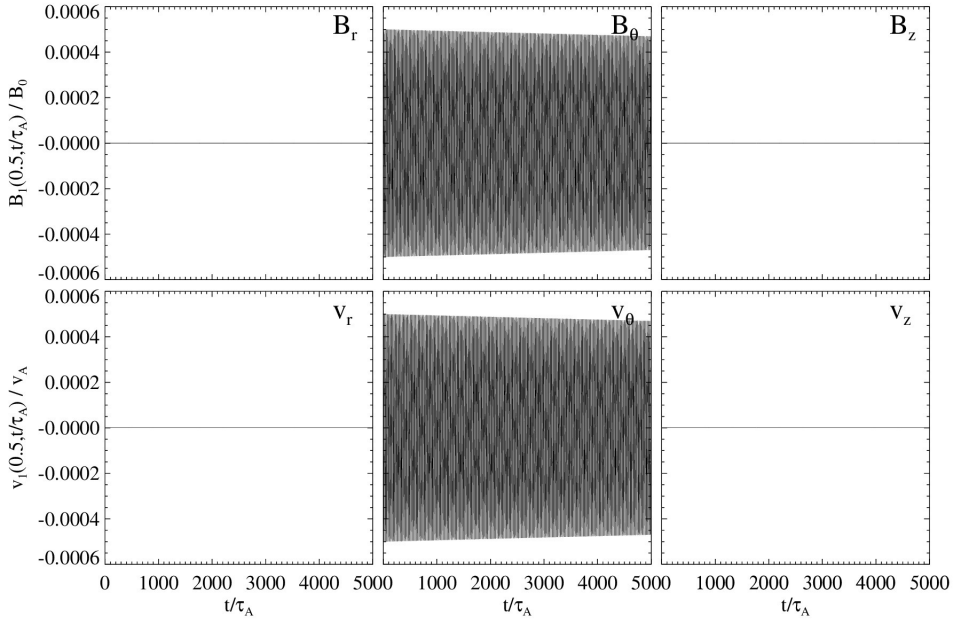

Figure 8.1: Simulation with uniform axial magnetic field and uniform density. $(m,n) = (0,1)$ mode with initial v_θ perturbation. The time traces of $\mathbf{v}_1$ and $\mathbf{B}_1$ normalized fields components are shown at a fixed radius $r/a = 0.5$.

If we zoom in the initial phase of the simulation (Fig. 8.2) we see that the time traces of b_θ and v_θ, which previously were indistinguishable because too compressed, now clearly appear as sinusoids with a period ΔT such that about 10 cycles are observed in a range of 250 τ_A. It is therefore expected that by doing the FFT of these time signals a single frequency $\omega\tau_A = 2\pi\tau_A/\Delta T \simeq 2\pi/25 \simeq 0.25$ would be obtained. Indeed doing the FFT in the interval $t \in [0, 500\tau_A]$, as shown in Figure 8.3, we obtain a spectrum with a single frequency centered on the expected value. This is the SAW that we expected from the theoretical analysis of Chapter 6. In general the color scale can be different for velocity components and field components. It must also be noted that the color scale in not linear but follows a power law, which is necessary to detect higher order harmonics, and it refers to the absolute value of the spectral amplitude. As we can see from Figure 8.4, we have an excellent agreement regarding both the frequency spectrum of the mode and its radial form.

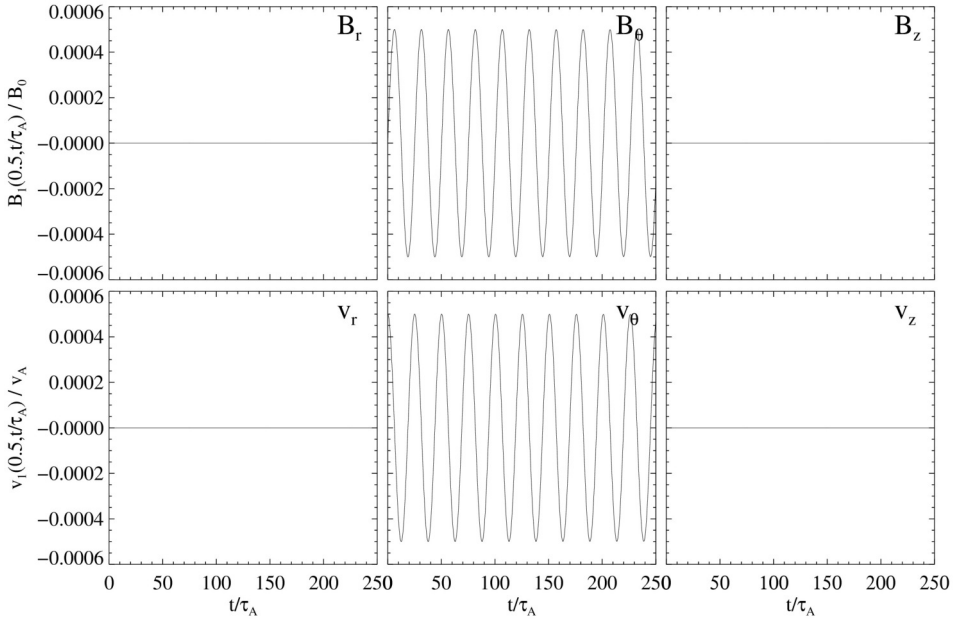

Figure 8.2: Simulation with uniform axial magnetic field and uniform density. $(m,n) = (0,1)$ mode with initial v_θ perturbation. The time traces of $\mathbf{v}_1$ and $\mathbf{B}_1$ normalized fields components are shown at a fixed radius $r/a = 0.5$.

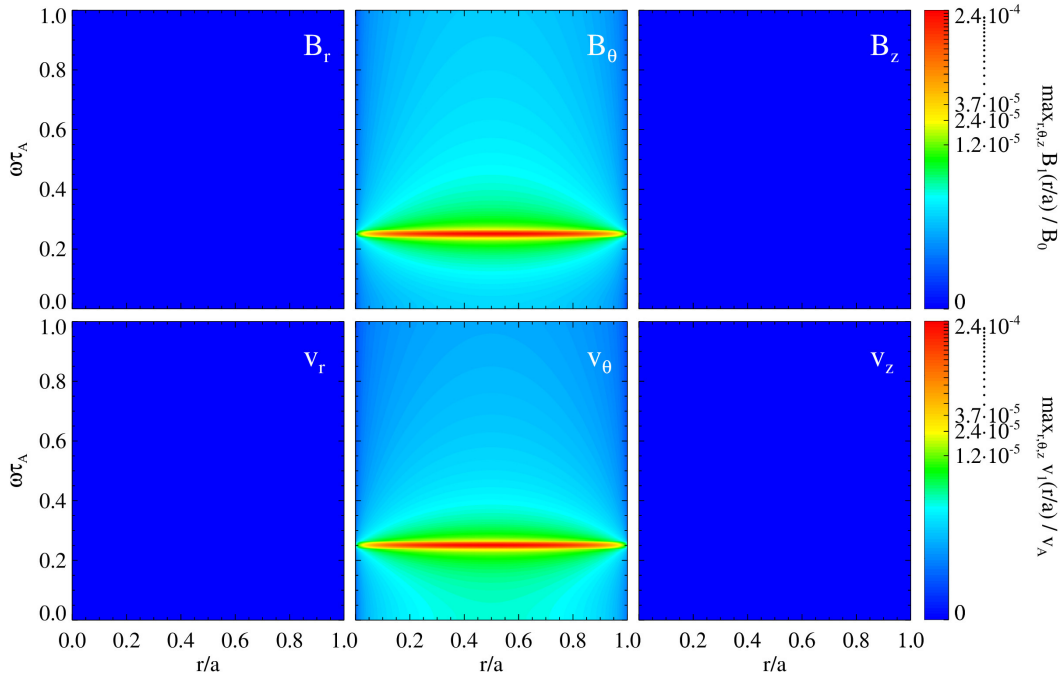

Figure 8.3: Simulation with uniform axial magnetic field and uniform density. $(m,n) = (0,1)$ mode with initial v_θ perturbation. The frequency spectra of $\mathbf{v}_1$ and $\mathbf{B}_1$ normalized fields components are shown as a function of radius, as computed for the time window $t \in [0, 500\tau_A]$.

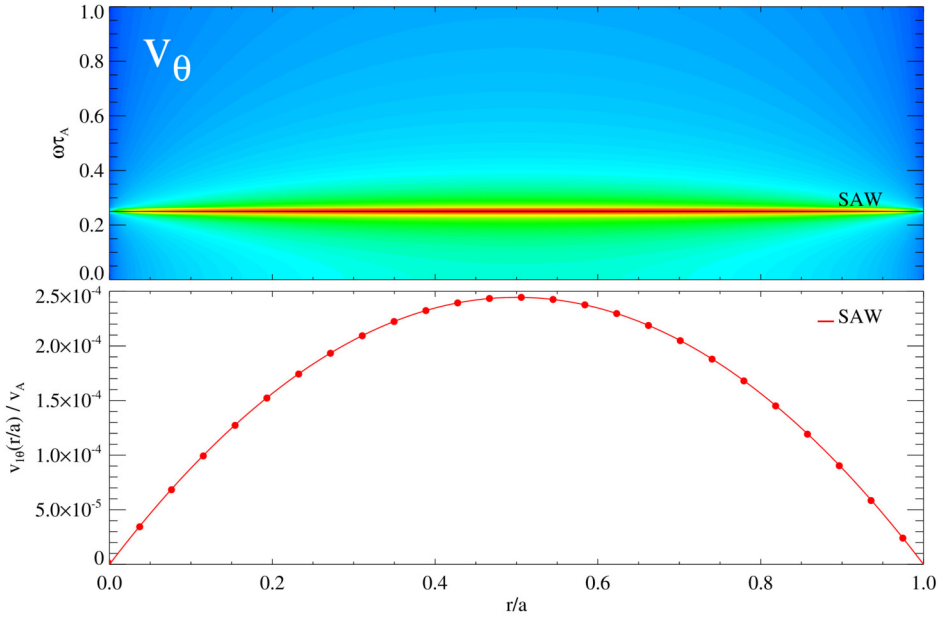

Figure 8.4: Simulation with uniform axial magnetic field and uniform density. $(m,n) = (0,1)$ mode with initial v_θ perturbation. Verification of frequency spectrum with the theoretical model for $v_{1\theta}$ velocity field component. On the top panel the agreement of simulation's frequency spectrum of the $v_{1\theta}$ component and the expected theoretical one (the SAW spectrum in Fig. 7.2) are shown. On the bottom panel the analytical perturbation given by Eq. (8.1) (solid line) is displayed together with the corresponding values from the simulation's spectrum (solid dots).

8.1.1.2 $(m,n) = (0,1)$ mode with initial v_r perturbation

Let's see now what we obtain from a simulation in which the radial component of velocity is perturbed instead of the azimuthal one. As we can see from Figure 8.5 in this case we obtain a time trend in which we have three non-zero components, B_r, B_z and v_r, which decay over time relatively quickly. If we plot the temporal traces on a narrower window of time (Fig. 8.6), again we recognize a wave pattern but this time it does not correspond to a simple sinusoidal wave. We therefore expect the spectrum to contain not only a dominant frequency but also higher harmonics. This is confirmed by Figure 8.7, in which multiple harmonics are observed. Looking at the frequency spectrum we can see the CAEs with their nodes, radial locations where the Alfvénic oscillations have zero amplitude for a specific field component.

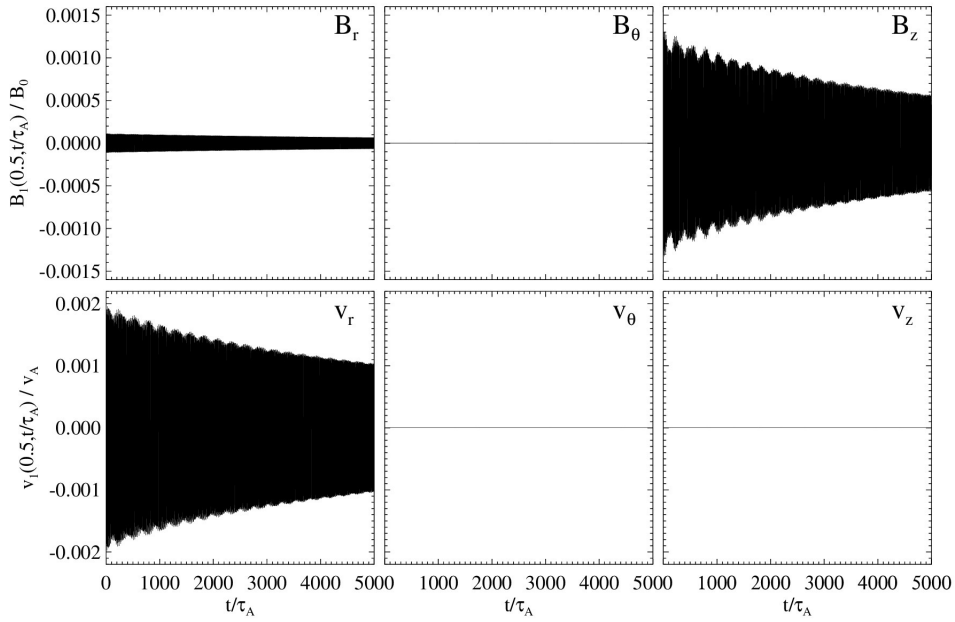

Figure 8.5: Simulation with uniform axial magnetic field and uniform density. $(m,n) = (0,1)$ mode with initial v_r perturbation. The time traces of $\mathbf{v}_1$ and $\mathbf{B}_1$ normalized fields components are shown at a fixed radius $r/a = 0.5$.

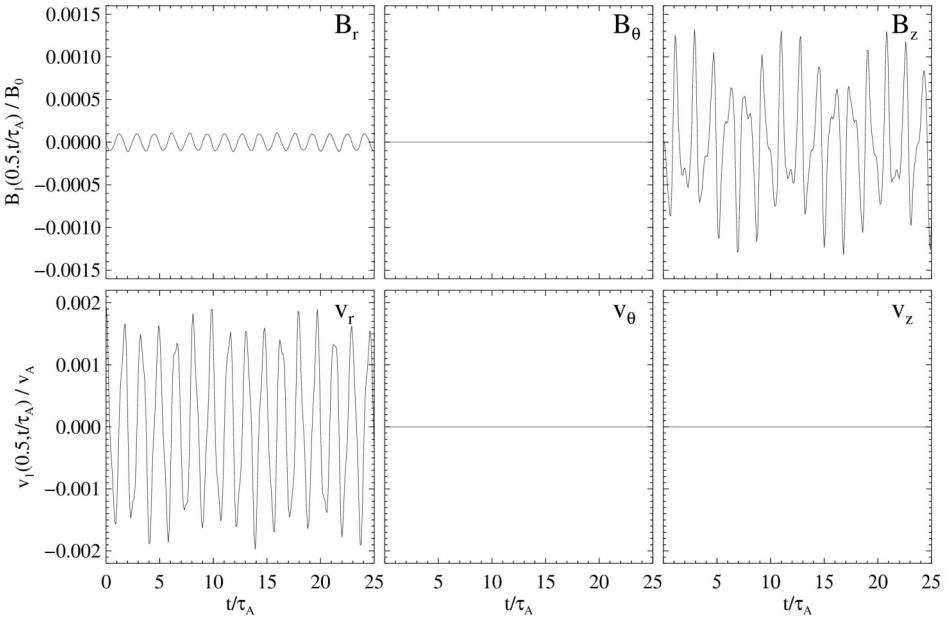

Figure 8.6: Simulation with uniform axial magnetic field and uniform density. $(m,n) = (0,1)$ mode with initial v_r perturbation. The time traces of $\mathbf{v}_1$ and $\mathbf{B}_1$ normalized fields components are shown at a fixed radius $r/a = 0.5$.

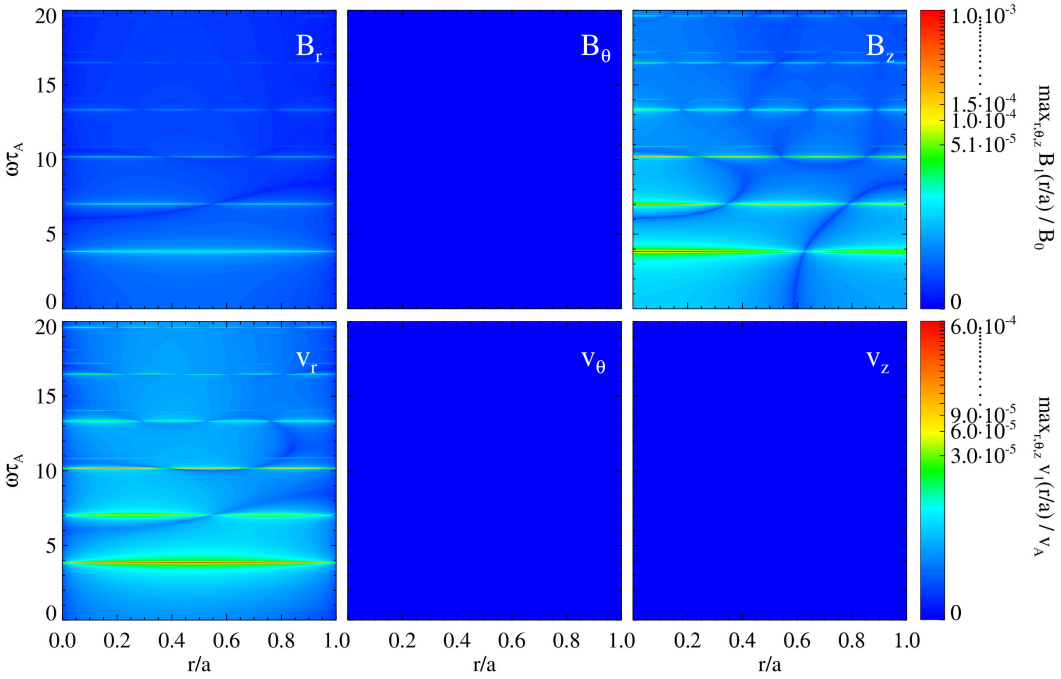

Figure 8.7: Simulation with uniform axial magnetic field and uniform density. $(m,n) = (0,1)$ mode with initial v_r perturbation. The frequency spectra of $\mathbf{v}_1$ and $\mathbf{B}_1$ normalized fields components are shown as a function of radius, as computed for the time window $t \in [0, 500\tau_A]$.

Again we have an excellent agreement between the simulation's spectrum and theoretical model as can be seen from Figure 8.8. This is a further demonstration of the robustness of the SpeCyl code, after the nonlinear verification benchmark discussed in [Bonfiglio, Chacón, and Cappello, 2010].

The above analysis was applied to similar single-mode simulations with mode numbers $m = 0$ and $0 \leq n \leq 6$ for both v_r and v_θ initial perturbations in order to verify the analytical dispersion relations for CAEs and SAW shown in in Figure 6.1. As can be seen from Figure 8.9 the values of the CAEs and SAW frequencies (solid dots) from the simulations are in complete agreement with the theoretical model (solid lines).

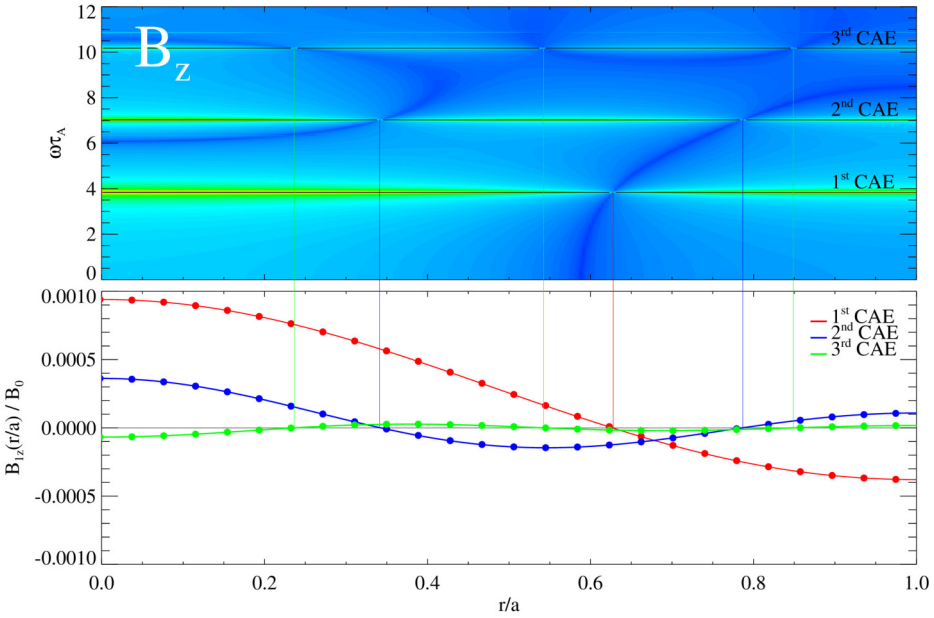

Figure 8.8: Simulation with uniform axial magnetic field and uniform density. $(m,n) = (0,1)$ mode with initial v_r perturbation. Verification of frequency spectrum with the theoretical model for B_{1z} magnetic field component. On the top panel, the simulation's frequency spectrum of the B_{1z} component and the corresponding analytical spectrum (CAE spectrum in Fig. 7.2) are shown. On the bottom panel the analytical Bessel function J_0 for the frequencies of the first three CAEs (solid lines) are displayed together with the corresponding values from the simulation's spectrum (solid dots). Note that on the top panel the oscillations are shown with their absolute values, while in the bottom panel they are not.

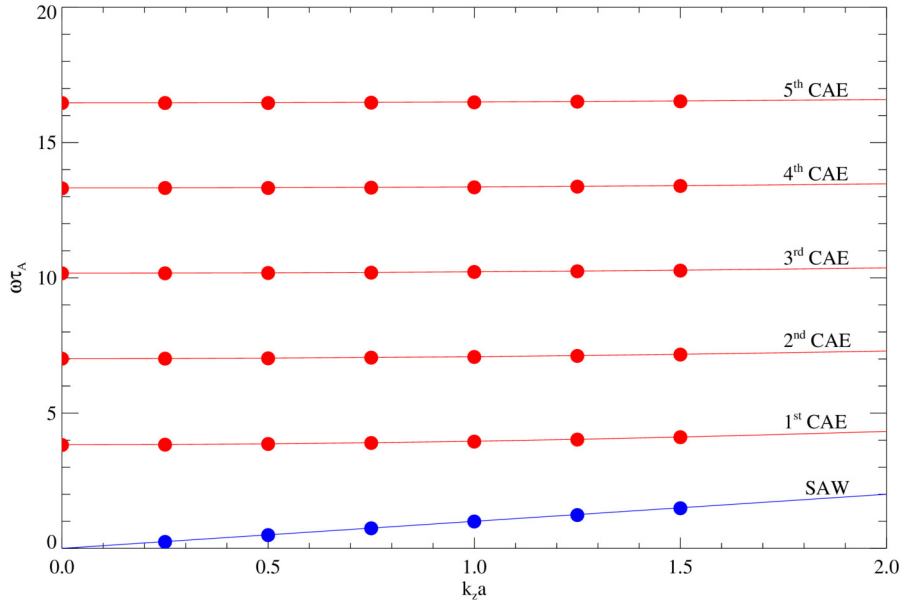

Figure 8.9: Simulation with uniform axial magnetic field and uniform density. Verification of numerical results against analytical spectra for $m = 0$. Frequency dependence on k_z wavevector component for SAW and the first five CAEs.

8.1.2 RFX-mod-like hollow density profile

Now let's consider the two previous cases with $(m,n) = (0,1)$ perturbed mode but in the presence of a hollow density profile, shown in Figure 7.3. We will see that there are no qualitative changes regarding the CAE, instead we will observe for the first time the phenomenon of phase mixing of the SAW.

8.1.2.1 $(m,n) = (0,1)$ mode with initial v_r perturbation

Let's first analyse the simulation with initial velocity perturbation on the radial component, which gives the CAE solutions. The resulting frequency spectrum for initial v_r perturbation, shown in Figure 8.10, is qualitatively very similar to the one with uniform density in Figure 8.7, with the CAEs frequencies now just slightly lower than before.

The verification with the expected spectrum from theoretical model (Fig. 7.4) is shown in Figure 8.11. In this case there is a small discrepancy due to the fact that now the expected CAEs frequencies are obtained in the WKB approximation through numerical calculation from the condition (6.43) as the MHD equations are no longer analytically solvable for CAEs in case of non-uniform plasma. Although approximate, the numerical computation of CAE frequencies will prove to be quite useful in all this Thesis to identify and interpret the observed frequency spectra from nonlinear MHD simulations.

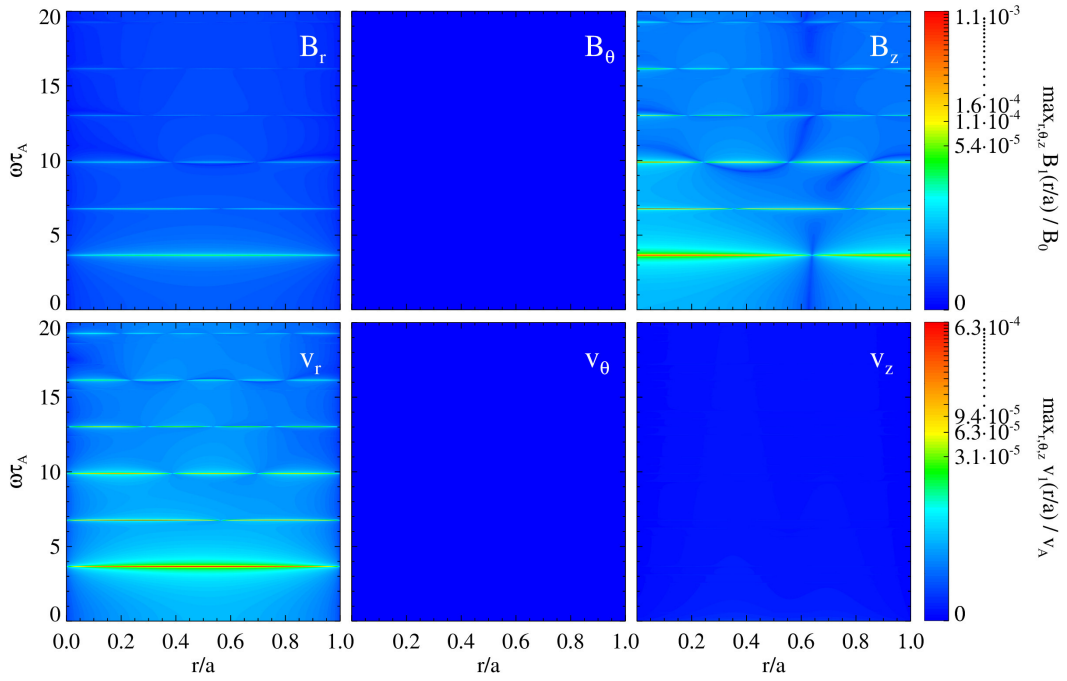

Figure 8.10: Simulation with uniform axial magnetic field and hollow density profile. $(m,n) = (0,1)$ mode with initial v_r perturbation. The frequency spectra of $\mathbf{v}_1$ and $\mathbf{B}_1$ normalized fields components are shown as a function of radius, as computed for the time window $t \in [0, 500\tau_A]$.

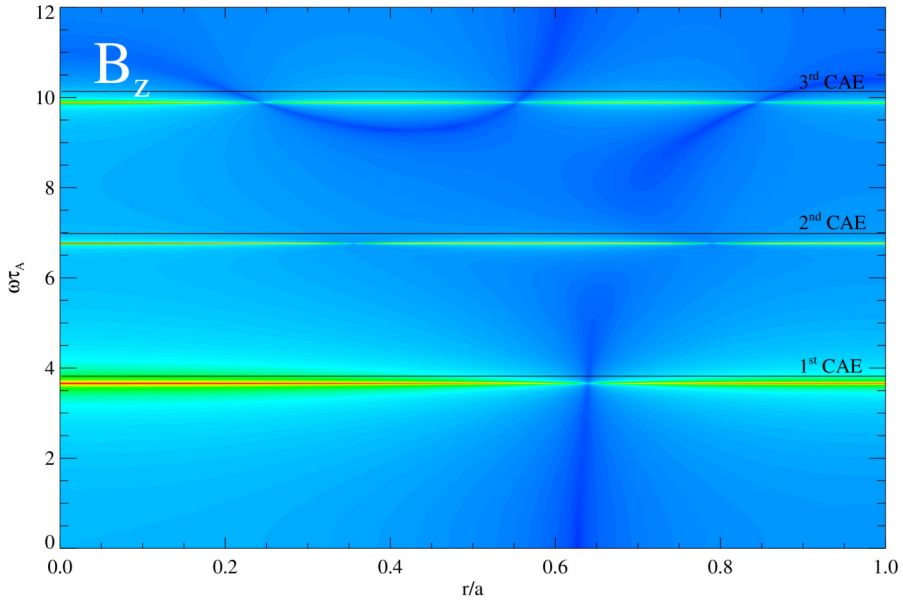

Figure 8.11: Simulation with uniform axial magnetic field and hollow density profile. $(m,n) = (0,1)$ mode with initial v_r perturbation. Verification of frequency spectrum with the theoretical model for B_{1z} magnetic field component.

8.1.2.2 $(m,n) = (0,1)$ mode with initial v_θ perturbation

We now proceed with the analysis of the nonlinear MHD simulation with initial velocity perturbation on the azimuthal component, which gives the Shear Alfvén Wave solution. We can see from Figure 8.12 that the frequency's profile is much different from the one with uniform density in Figure 8.3. Now we have a Shear Alfvén Wave characterized by a continuous spectrum with a frequency that depends on the radius, with the $\omega(r)$ profile resembling the inverse of the density profile (Fig. 7.3). This is perfectly expected, as the Alfvén frequency is inversely proportional to the root of the density (Eq. (6.32)). Indeed, as expected we can see from Figure 8.13 that the frequency spectrum is perfectly superimposed to the theoretical shear Alfvén spectrum from Fig. 7.4.

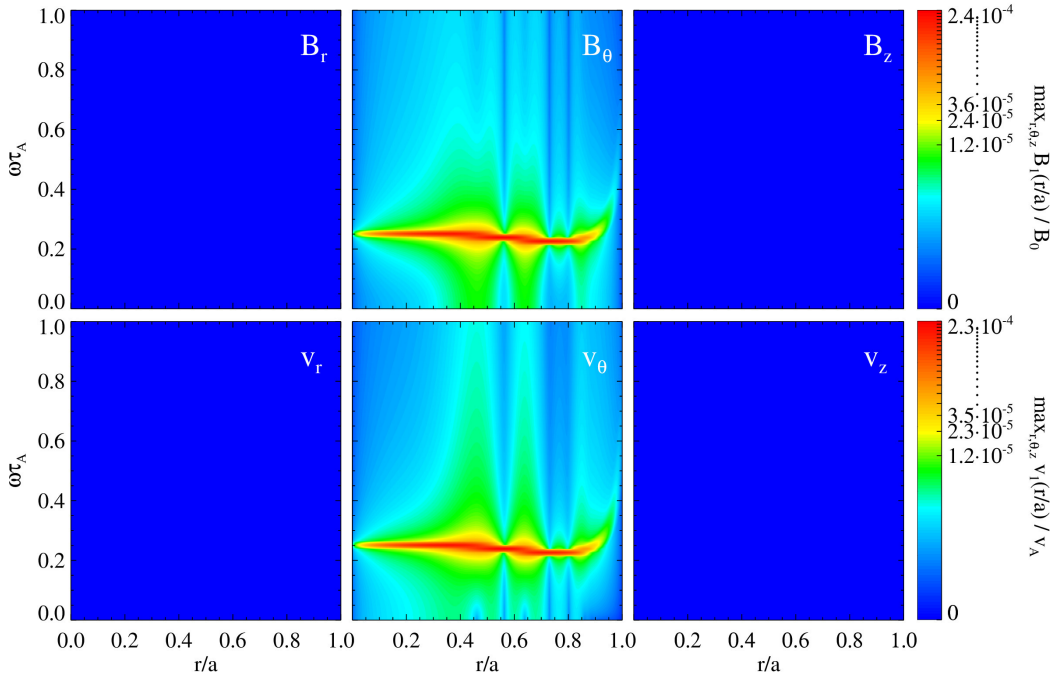

Figure 8.12: Simulation with uniform axial magnetic field and hollow density profile. $(m,n) = (0,1)$ mode with initial v_θ perturbation. The frequency spectra of $\mathbf{v}_1$ and $\mathbf{B}_1$ normalized fields components are shown as a function of radius, as computed for the time window $t \in [0, 500\tau_A]$.

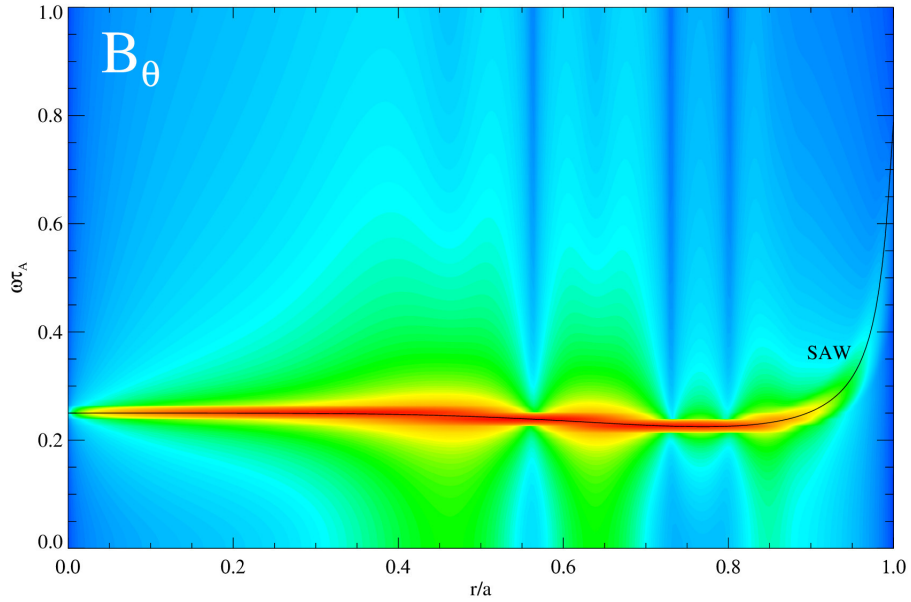

Figure 8.13: Simulation with uniform axial magnetic field and hollow density profile. $(m,n) = (0,1)$ mode with initial v_θ perturbation. Verification of the nonlinear MHD simulation results against the theoretical Shear Alfvén solution, for the $B_{1\theta}$ magnetic field component.

We now look at the time evolution of the SAW spectrum during the nonlinear MHD simulation. To do this, we do the FFT of simulation data on a moving time window, with same time interval of $500\tau_A$ but increasing initial time, as exemplified with square brackets in Fig. 8.14. In this way it is possible to see that the SAW spectrum changes in time, as shown in Figure 8.15. By looking at the temporal evolution of the SAW spectrum, one can observe an interesting phenomenon, that is the fact that the amplitude of the wave is damped very quickly in the radial positions that correspond to regions with a radial gradient of the Alfvén frequency, while it remains almost constant in the radial positions that correspond to the extremes of the $\omega(r)$, i.e. the initial region and the region around $r/a = 0.75$. This is perfectly consistent with the phase mixing phenomenon, discussed in Section 6.2.1, due to which the Alfvén wave tends to be more rapidly damped in the regions with spatially variable Alfvén frequency. This damping mechanism is added to the damping due to the visco-resistive dissipation, which instead occurs in a similar way throughout the plasma volume since the dissipation coefficients (resistivity and viscosity) are assumed to be uniform in these SpeCyl simulations.

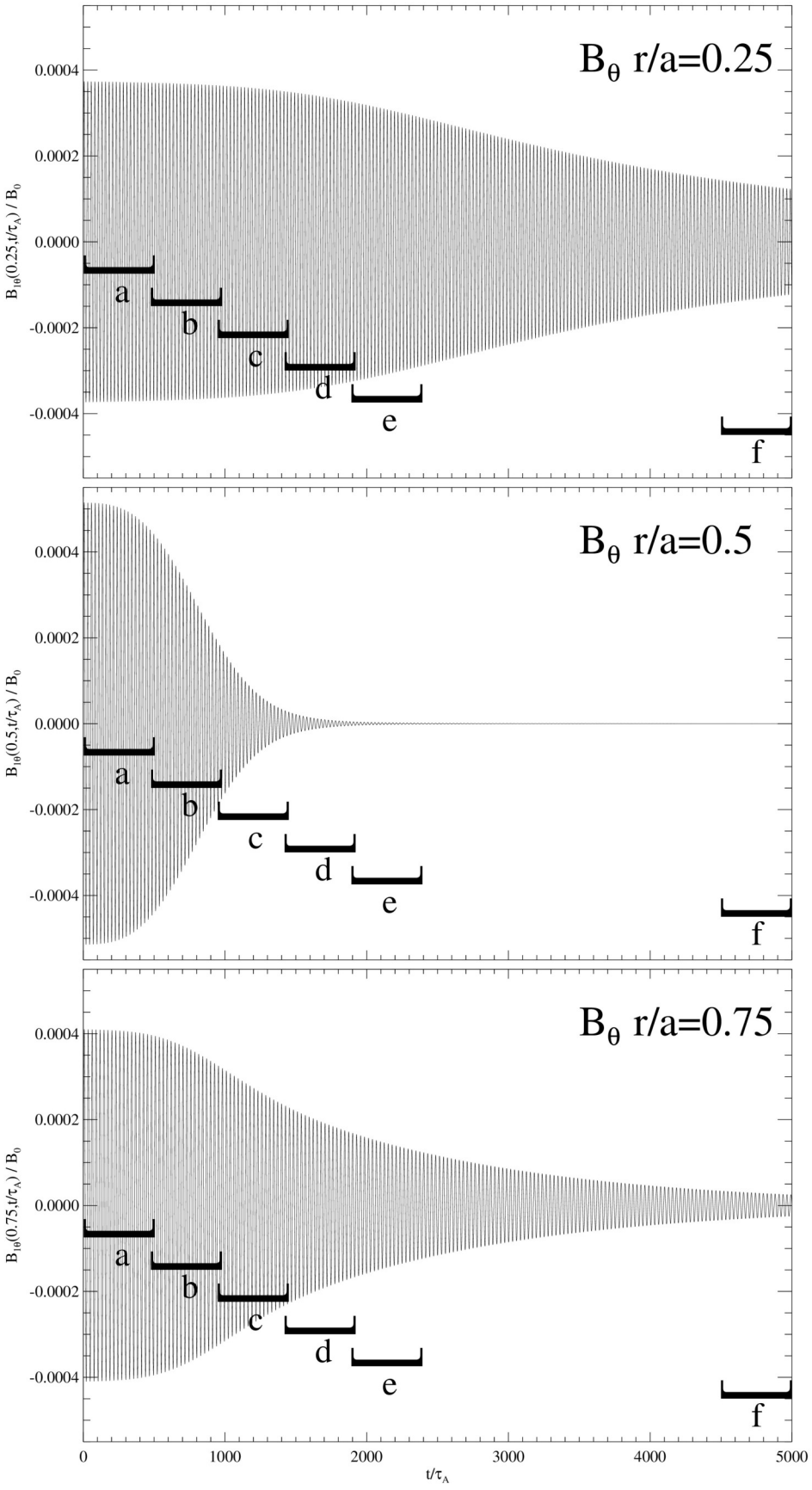
B_θ r/a=0.25
B_θ r/a=0.5
B_θ r/a=0.75
B_θ(0.25,t/τ_A) / B_0
B_θ(0.5,t/τ_A) / B_0
B_θ(0.75,t/τ_A) / B_0
0.0004
0.0002
0.0000
-0.0002
-0.0004
a
b
c
d
e
f
0
1000
2000
3000
4000
5000
t/τ_A

Figure 8.14: Simulation with uniform axial magnetic field and hollow density profile. $(m,n) = (0,1)$ mode with initial v_θ perturbation. The time traces of the normalized magnetic field component $B_{1\theta}$ are shown at a fixed radius $r/a = 0.2,\ 0.5,\ 0.75$. The time windows indicated are those used in the analysis of Fig. 8.15.

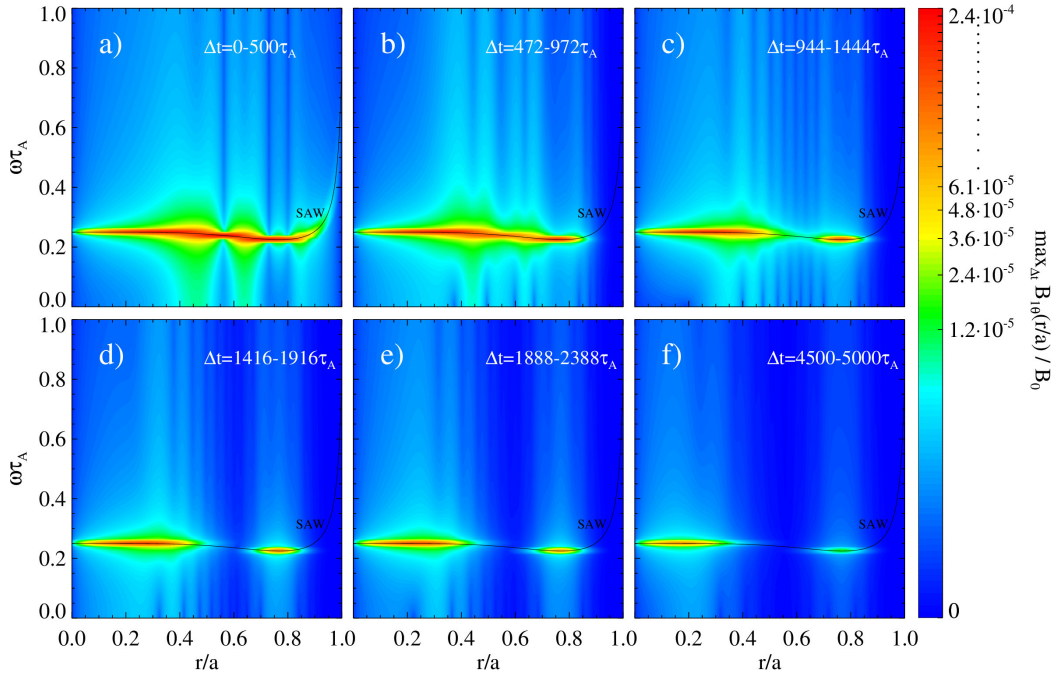

Figure 8.15: Simulation with uniform axial magnetic field and hollow density profile. $(m,n) = (0,1)$ mode with initial v_θ perturbation. Time evolution of the frequency spectrum of the normalized magnetic field component $B_{1\theta}$ at the beginning of the simulation (panels a-e) and the end of the simulation (panel f).[1]

8.2 Tokamak-like equilibrium configuration

Now we consider the first case with a variable magnetic field. A weak azimuthal field is added to the uniform axial field, as shown in Figure 7.5. This is an intermediate case that we consider before moving on to the configuration that most interests us, namely the RFP. For this tokamak configuration we consider only the case with uniform density as here we are mainly interested in the consequences of the non-uniformity of the magnetic field.

[1]For those interested the corresponding movie can bee seen at the following link: https://www.dropbox.com/s/k269k77xv2c95ap/Bt_denn_pertvt.mp4?dl=0.

8.2.1 Uniform density $\rho_0 = 1$

8.2.1.1 $(m,n) = (0,1)$ mode with initial v_r and v_θ perturbation

Perturbing v_r we can see in Figure 8.16 that now the CAE spectrum is present (albeit weak) also in the B_θ, v_θ and v_z components, compared with the analogous Figure 8.7 in the uniform field case in which these components weren't excited at all. In addition, now in the B_θ and v_θ components appears a weak SAW signal. Vice versa, by perturbing the v_θ component (Figure 8.17), the SAW signal is dominant as in the analogous uniform field case in Figure 8.3, but there also appears a weak signal that corresponds to the CAE spectrum. So there is a weak coupling of the shear and the compressional modes (as the magnetic field has a weakly variable azimuthal component). As mentioned in Section 6.2.1 this coupling is due to the fact that the wavevector $\mathbf{k}$ is oblique to the magnetic field $\mathbf{B}_0$, in this case $\mathbf{k}$ is oblique due to the weak azimuthal component of the magnetic field. A stronger coupling will be seen in the RFP case (which presents a more strongly variable magnetic field), where the SAW and the CAE will have similar amplitude by perturbing either v_r or v_θ, and therefore only the perturbation in v_r will be discussed there.

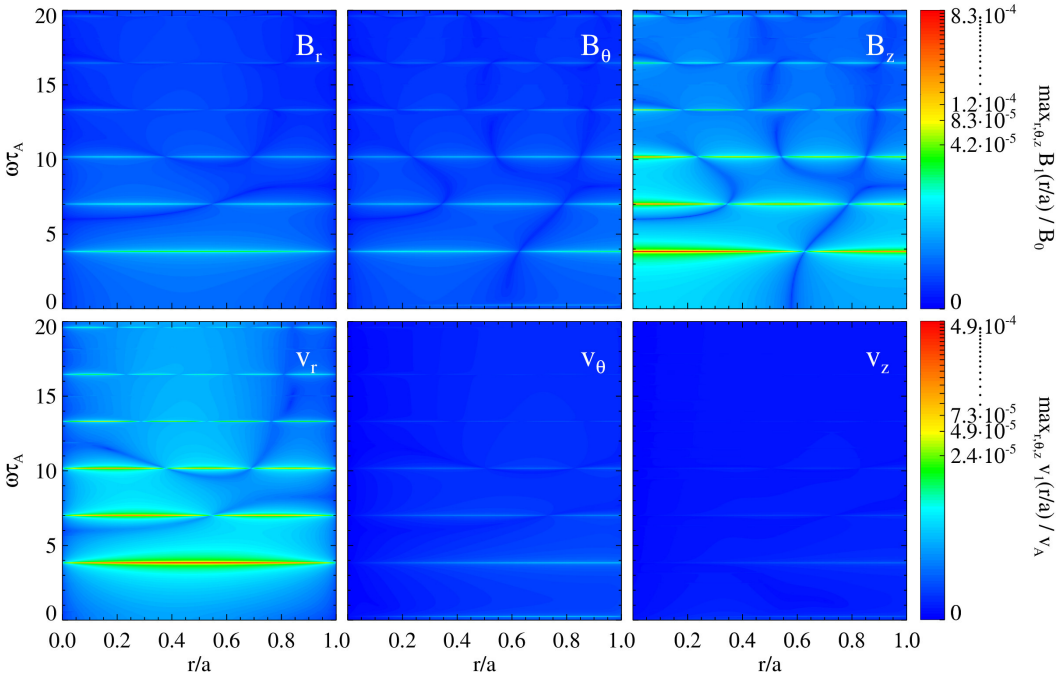

Figure 8.16: Simulation with Tokamak-like magnetic field and uniform density. $(m,n) = (0,1)$ mode with initial v_r perturbation. The frequency spectra of $\mathbf{v}_1$ and $\mathbf{B}_1$ normalized fields components are shown as a function of radius, as computed for the time window $t \in [0, 500\tau_A]$.

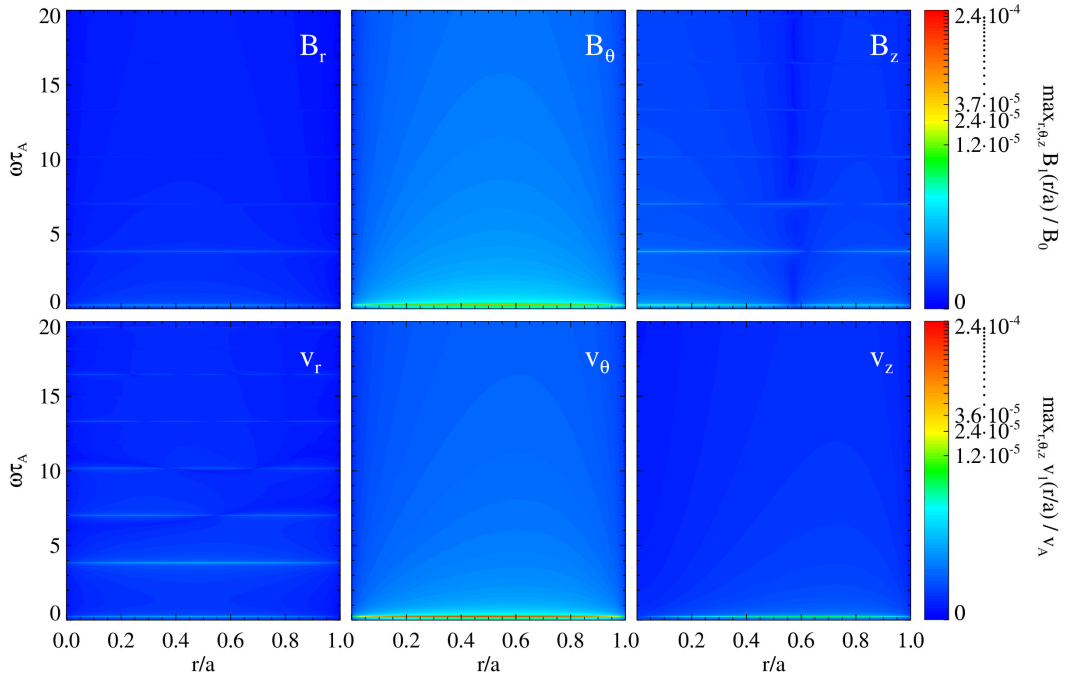

Figure 8.17: Simulation with Tokamak-like magnetic field and uniform density. $(m,n) = (0,1)$ mode with initial v_θ perturbation. The frequency spectra of $\mathbf{v}_1$ and $\mathbf{B}_1$ normalized fields components are shown as a function of radius, as computed for the time window $t \in [0, 500\tau_A]$.

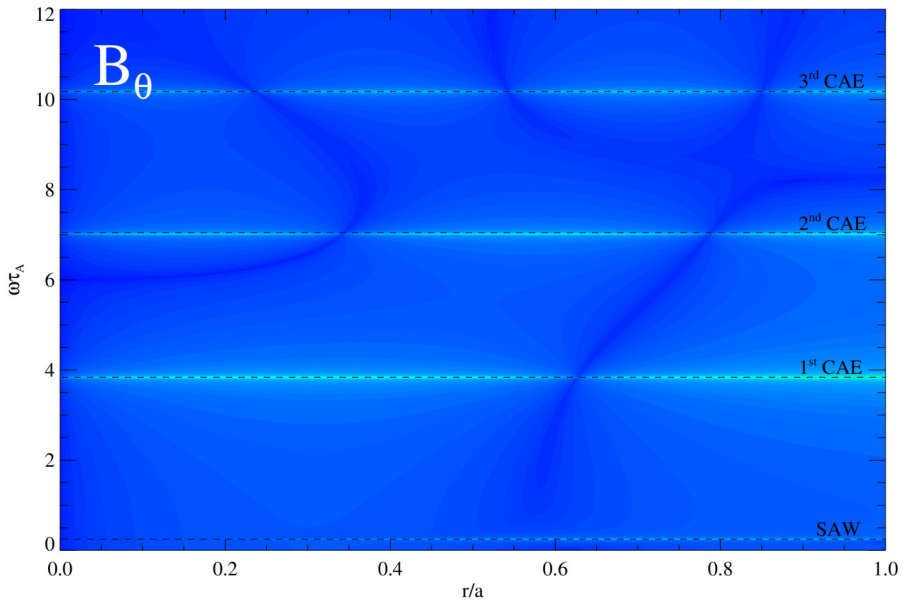

Figure 8.18: Simulation with Tokamak-like magnetic field and uniform density. $(m,n) = (0,1)$ mode with initial v_r perturbation. Verification of the frequency spectrum with the theoretical model for the $B_{1\theta}$ magnetic field component. The dotted line is used in this case (instead of a solid line) due to the rather low amplitude of the spectrum.

In Figure 8.18 we show the comparison between the numerical frequency spectrum resulting from the SpeCyl simulation with initial v_r perturbation and the expected theoretical one from Fig. 7.6. The agreement between the two is excellent, even with numerically calculated CAE frequencies as the WKB approximation in this case of weakly variable magnetic field is a very good approximation.

8.3 "Academic" RFP-like equilibrium configuration

We will now discuss the most interesting results of this Thesis considering the RFP-like configuration (Figure 7.7). The results discussed in this section and in the next one will allow us to obtain physical indications on the experimental observations of Alfvén Eigenmodes in the RFX-mod experiment.

8.3.1 Uniform density $\rho_0 = 1$

8.3.1.1 $(m,n) = (1,0)$ mode with initial v_r perturbation

From now on we will consider the $(m,n) = (1,0)$ mode (instead of the $(0,1)$ mode considered in previous cases), as experimentally it is the Fourier component with the strongest Alfvénic activity, and also because this mode is the most excited by Alfvén waves in "realistic" RFP simulations, as we will see in Section 8.5.1.1. The frequency spectrum in this case of uniform density ρ_0 is shown in Figure 8.19. Now all the components of $\mathbf{v}_1$ and $\mathbf{B}_1$ fields are affected by both continuous SAW and CAEs, with comparable amplitudes. Therefore, as anticipated before, in the RFP case with strongly variable fields we will analyse only the simulations with the initial v_r perturbation. Also now the SAW frequency range increases while the CAE frequencies are shifted down, so that a very peculiar condition occurs in which the SAW and the 1^{st} CAE intersect each other.

In Fig. 8.20 we show the comparison of the numerical spectrum resulting from SpeCyl simulations with the expected theoretical spectrum for this configuration (Fig. 7.8). A good qualitative agreement between the numerical and theoretical spectra is observed. As mentioned before the small discrepancy of the CAE spectrum is due to the fact that now the expected CAEs frequencies are obtained in the WKB approximation through numerical calculation from the condition (6.43) as the MHD equations are no longer analytically solvable in this configuration.

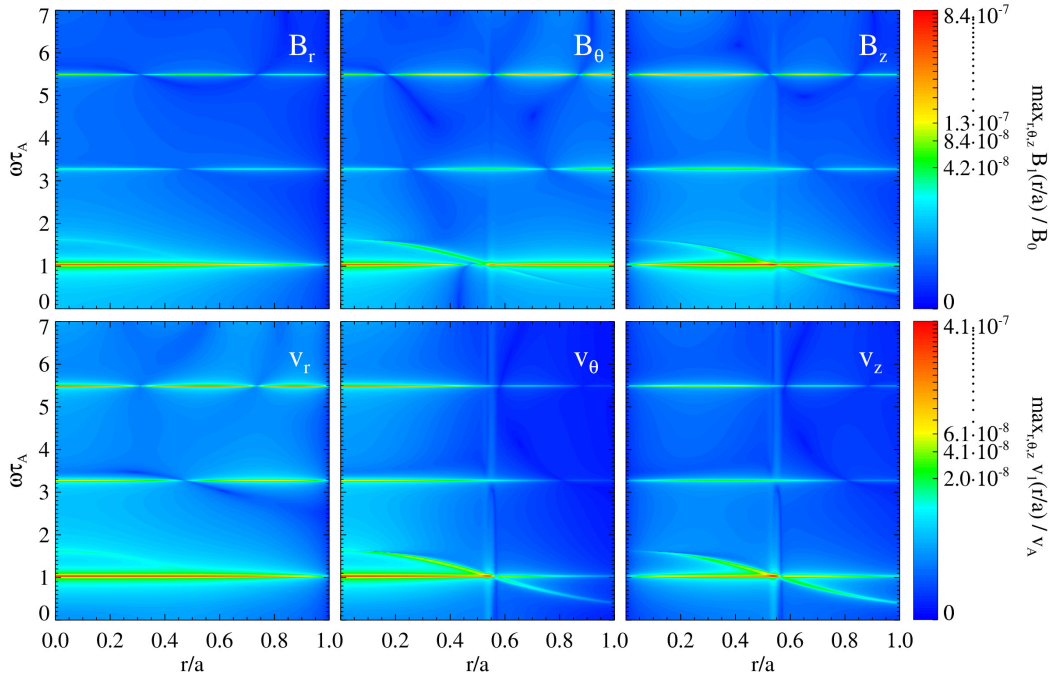

Figure 8.19: Simulation with RFP-like magnetic field and uniform density. $(m,n) = (1,0)$ mode with initial v_r perturbation. The frequency spectra of $\mathbf{v}_1$ and $\mathbf{B}_1$ normalized fields components are shown as a function of radius, as computed for the time window $t \in [0, 500\tau_A]$.

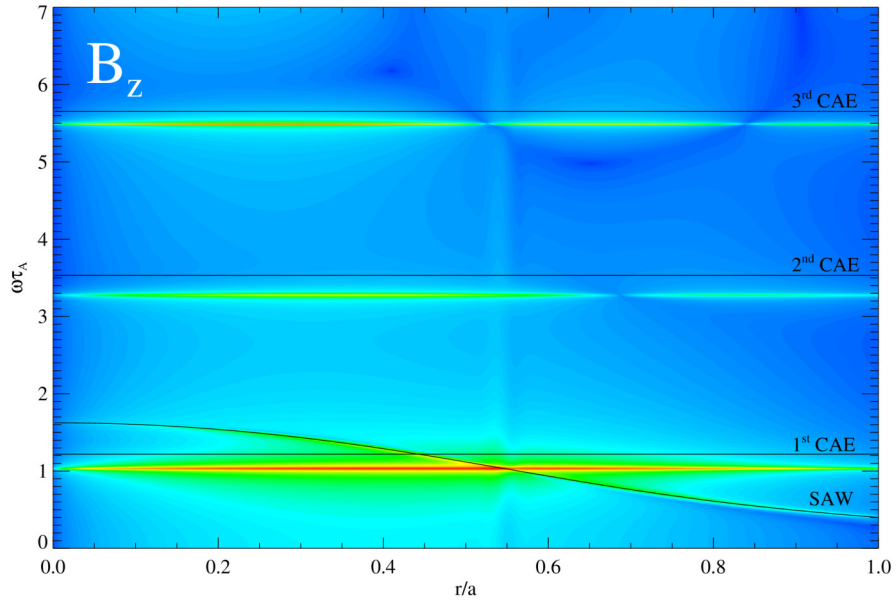

Figure 8.20: Simulation with RFP-like magnetic field and uniform density. $(m,n) = (1,0)$ mode with initial v_r perturbation. Verification of frequency spectrum with the theoretical model for B_{1z} magnetic field component.

We now look at the time evolution of the B_{1z} component, as shown in Figure 8.21. The SAW vanishes rather quickly, due to the phase mixing phenomenon already discussed in Section 6.2.1. On the other hand, the amplitudes of CAE modes just slightly decay in time, as damped by viscosity and resistivity, as we have seen for example in Figure 8.5. We would also have expected in this case to see the Alfvén resonance absorption of the 1^{st} CAE since its frequency is equal to that of the Alfvén resonance condition (6.32) in a radial location around $r/a = 0.5$. Such effect is not actually observed in this case, although it will be recovered in the case with non-uniform density profile, as will be discussed in Section 8.3.2.

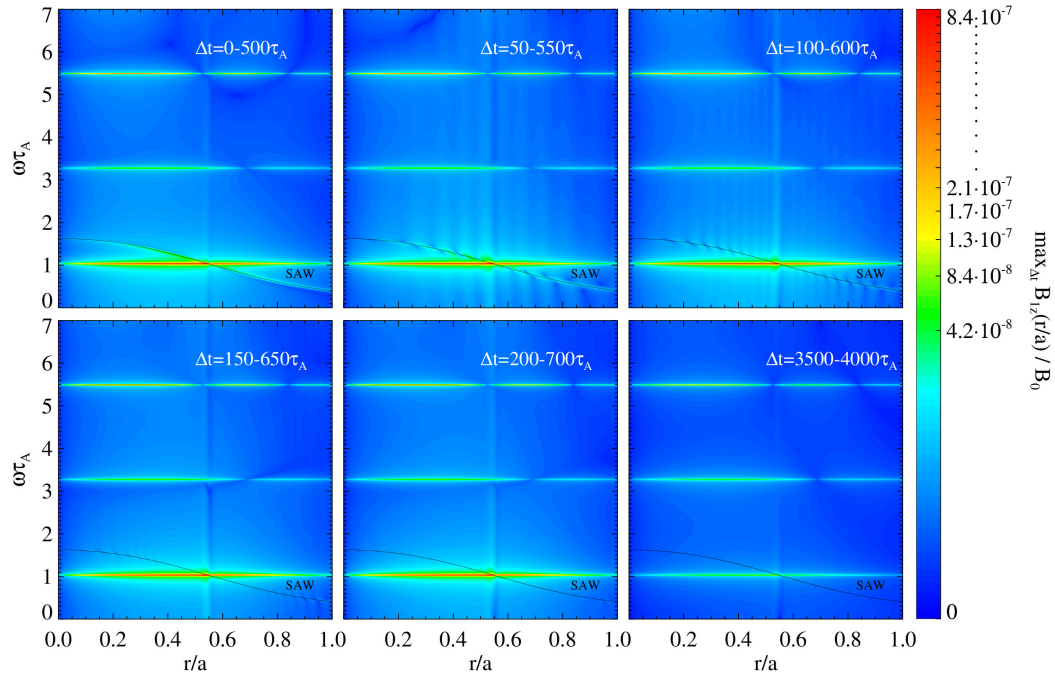

Figure 8.21: Simulation with RFP-like magnetic field and uniform density. $(m,n) = (1,0)$ mode with initial v_r perturbation. Time evolution of the frequency spectrum of the normalized magnetic field component B_{1z} at the beginning of the simulation (panels 1-5) and the end of the simulation (panel 6).[2]

To see the damping processes more clearly we can plot the frequency in function of time, as shown in Fig. 8.22 at a fixed radius r/a. In this case we plotted the evolution of the

[2]The corresponding movie can bee seen at the following link:
https://www.dropbox.com/s/dacwcppg047yzdg/Bz_Var_pertvr.mp4?dl=0.

frequency spectrum of B_{1z} component for two radius values $r/a = 0.3$ and $r/a = 0.9$. As we can see the CAE amplitudes remain slightly unchanged until the end of the simulation, while SAW is quickly and completely damped in the first 150 Alfvén times.

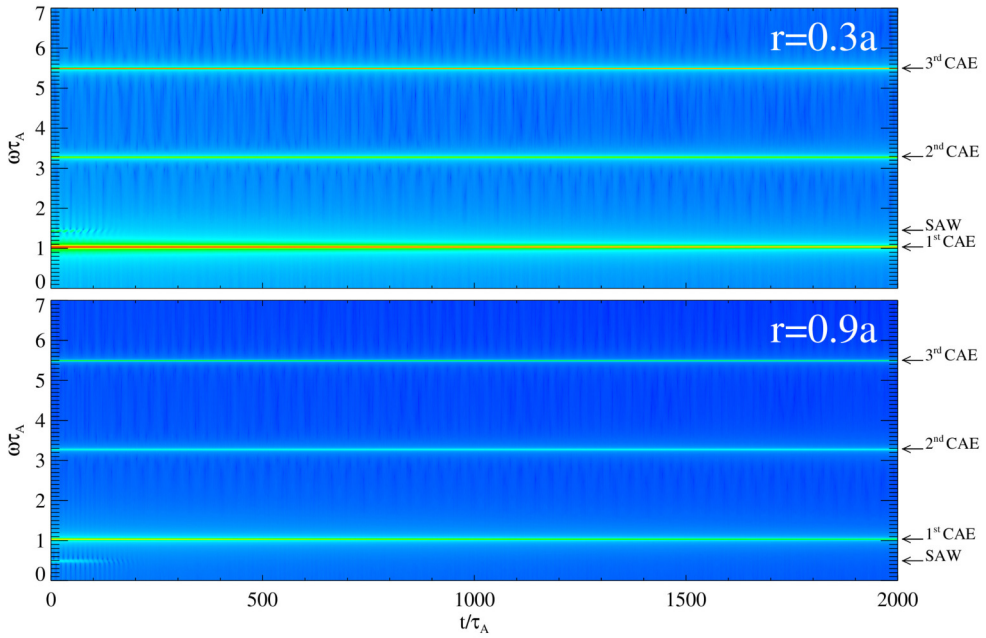

Figure 8.22: Simulation with RFP-like magnetic field and uniform density. $(m,n) = (1,0)$ mode with initial v_r perturbation. Time evolution of the frequency spectrum of the normalized magnetic field component B_{1z} at a fixed radius $r/a = 0.3$ and $r/a = 0.9$.

8.3.2 RFX-mod-like hollow density profile

8.3.2.1 $(m,n) = (1,0)$ mode with initial v_r perturbation

We now analyze the same mode $(m,n) = (1,0)$ but with an RFX-mod like density profile $\rho_0(r)$. The resulting frequency spectrum is shown in Figure 8.23. This spectrum is very similar to the one with uniform density (Fig. 8.19) except that now the Alfvén continuum has a minimum at around $r/a = 0.9$. In Fig. 8.24 we superimpose this spectrum with the expected theoretical one (Fig. 7.9) to identify the various frequencies. The qualitative agreement is good, again the quantitative differences can be ascribed to the WKB approximation used to compute the theoretical spectra. However, in this case we would also have expected to see the GAE solution, a global mode right below the Alfvén continuum minimum like in Fig. 7.9. In the following sections we will see that the GAE mode is actually observed in "academic" RFP simulations when a density profile peaked in the plasma center is used. The GAE solution will be also found in "realistic" RFP simulations discussed in Section 8.5.2.

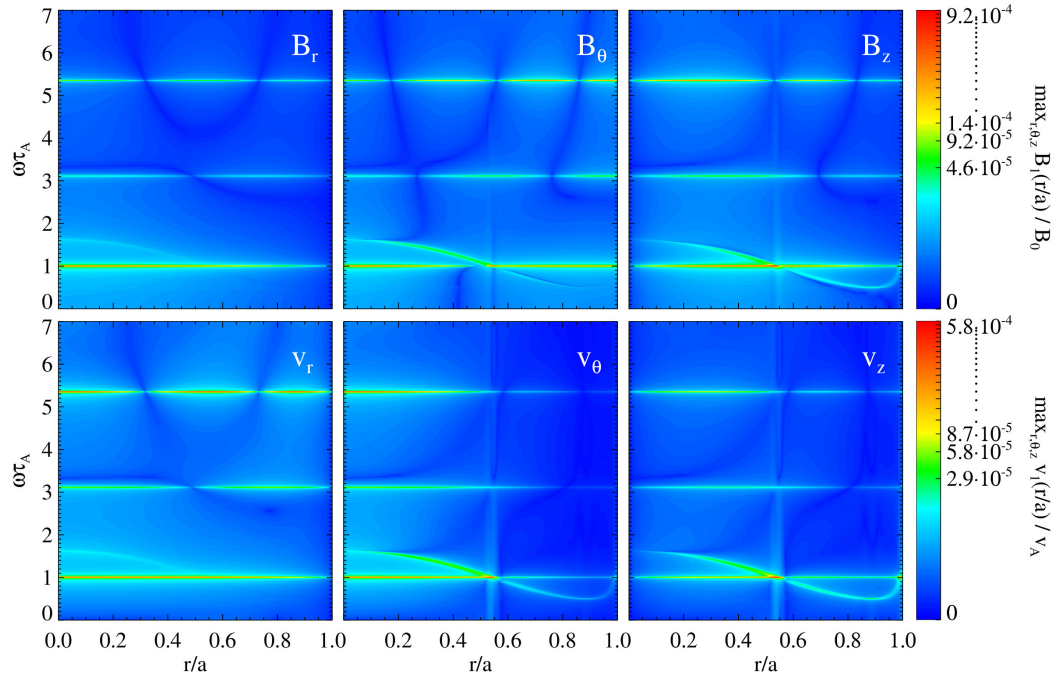

Figure 8.23: Simulation with RFP-like magnetic field and hollow density profile. $(m,n) = (1,0)$ mode with initial v_r perturbation. The frequency spectra of $\mathbf{v}_1$ and $\mathbf{B}_1$ normalized fields components are shown as a function of radius, as computed for the time window $t \in [0, 500\tau_A]$.

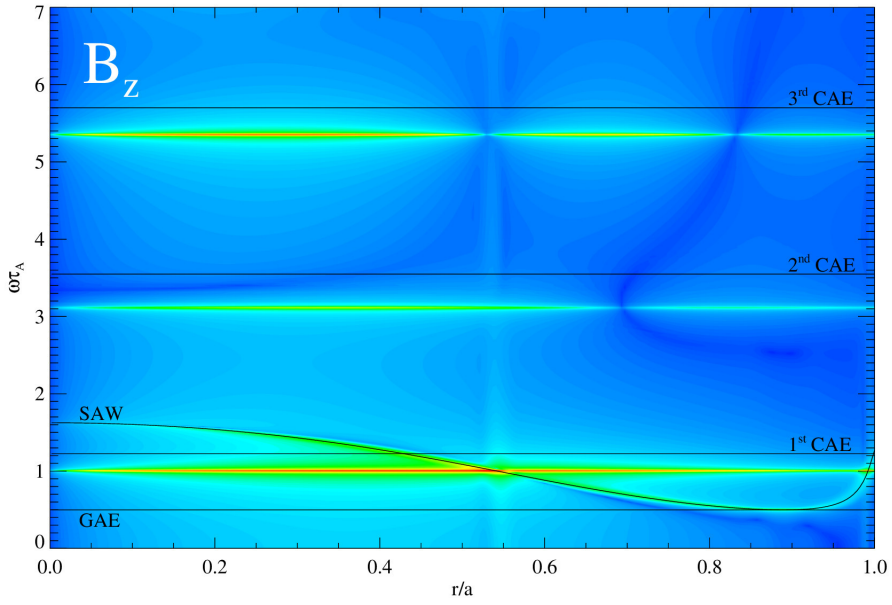

Figure 8.24: Simulation with RFP-like magnetic field and hollow density profile. $(m,n) = (1,0)$ mode with initial v_r perturbation. Verification of frequency spectrum with the theoretical model for B_{1z} magnetic field component.

We now look at the time evolution of the B_{1z} spectrum, as shown in Figure 8.25. As in the case with uniform density, we can observe again the phase mixing of the SAW, which completely disappears at the end of the simulation, even if now the SAW amplitude at the minimum of the Alfvén continuum survives for a longer time. This time, however, we also observe the expected resonance absorption of the 1^{st} CAE, which is indeed completely vanished at the end of the simulation. To better quantify the different damping processes, in Figure 8.26 the frequency spectrum is shown as a function of time for fixed radial locations. On the top panel, for $r/a = 0.3$, we can see that SAW is damped in the same time window as in the case of uniform density, but now, while the 2^{nd} and 3^{rd} CAE remain over time, the 1^{st} one is damped because of the resonance absorption. In particular the 1^{st} CAE completely vanishes before $t = 3000\tau_A$. On the bottom panel, for $r/a = 0.9$, we can see that Alfvén minimum survives for a longer time than the uniform density case (see Fig. 8.22) as it does not undergo the phase mixing.

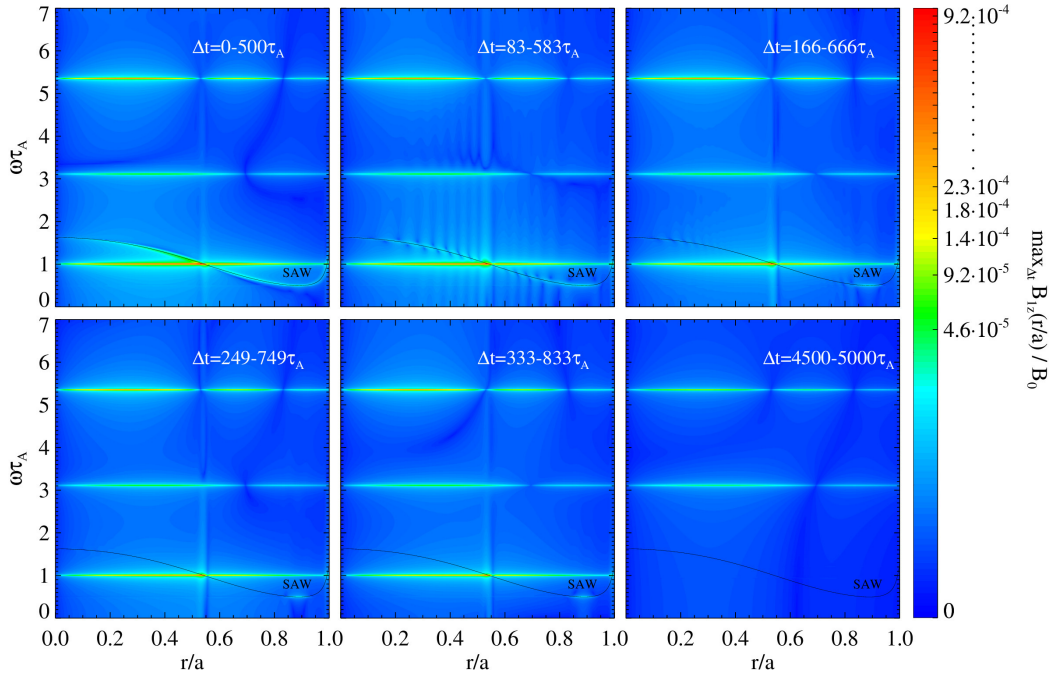

Figure 8.25: Simulation with RFP-like magnetic field and hollow density profile. $(m,n) = (1,0)$ mode with initial v_r perturbation. Time evolution of the frequency spectrum of the normalized magnetic field component B_{1z} at the beginning of the simulation (panels 1-5) and the end of the simulation (panel 6).[3]

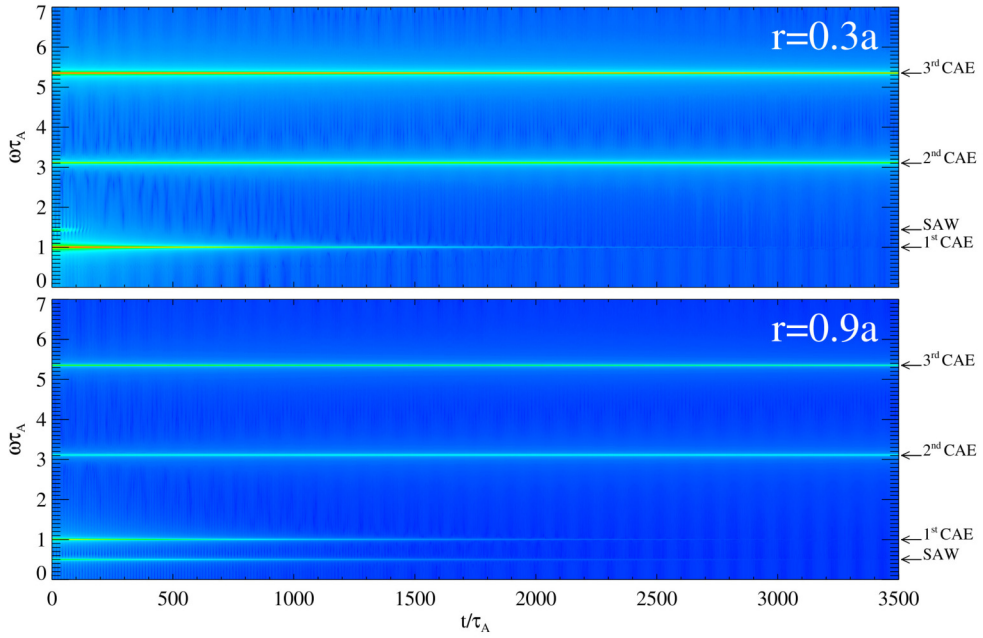

Figure 8.26: Simulation with RFP-like magnetic field and hollow density profile. (m,n) = $(1,0)$ mode with initial v_r perturbation. Time evolution of the frequency spectrum of the normalized magnetic field component B_{1z} at a fixed radius $r/a = 0.3$ and $r/a = 0.9$.

8.3.2.2 $(m,n) = (0,2)$ and $(m,n) = (4,4)$ modes with initial v_r perturbation

To further characterize the resonance absorption phenomenon, we investigated two additional cases to confirm that a necessary condition for resonance absorption to occur is the fact that the discrete frequency of a CAE mode falls into the Alfvén continuum. We analysed two cases with different periodicities of the initial applied perturbation. The first case, corresponding to the $(m,n) = (0,2)$ perturbed mode, is characterized by the Alfvén continuum everywhere below the 1^{st} CAE frequency. On the contrary, in the second case with $(m,n) = (4,4)$ perturbed mode, the Alfvén continuum crosses not only the first but also the second CAE. The temporal evolution of the two simulations is shown in Fig. 8.27 (first case) and in Fig. 8.28 (second case). As expected, we see that in the first case the CAEs are not damped, while in the second case both the 1^{st} and the 2^{nd} CAE are damped very quickly in time.

These numerical findings confirm that the a necessary condition for the resonance absorption of the CAEs is that their frequencies fall into the Alfvén continuum. This is indeed the reason why the resonance absorption phenomenon is also called continuum damping. In this Thesis, the only case where the resonance absorption of the first CAE was not observed, even if the necessary resonance condition was satisfied, was the case with

[3]The corresponding movie can bee seen at the following link:
https://www.dropbox.com/s/jqjir6v4z9nezc9/Bz_Var_denn_pertvr.mp4?dl=0.

uniform density discussed in Section 8.3.1. We have not yet found a proper explanation for this observation. Indeed, continuum damping is theoretically predicted even with uniform density [Chen and Hasegawa, 1974] as we also found in other cases. In particular, the simulation with the $(m,n) = (4,4)$ mode was also performed with uniform density[4], and again the continuum damping of the two first CAEs was observed as expected, quite similarly to the case discussed in this Section with hollow density profile.

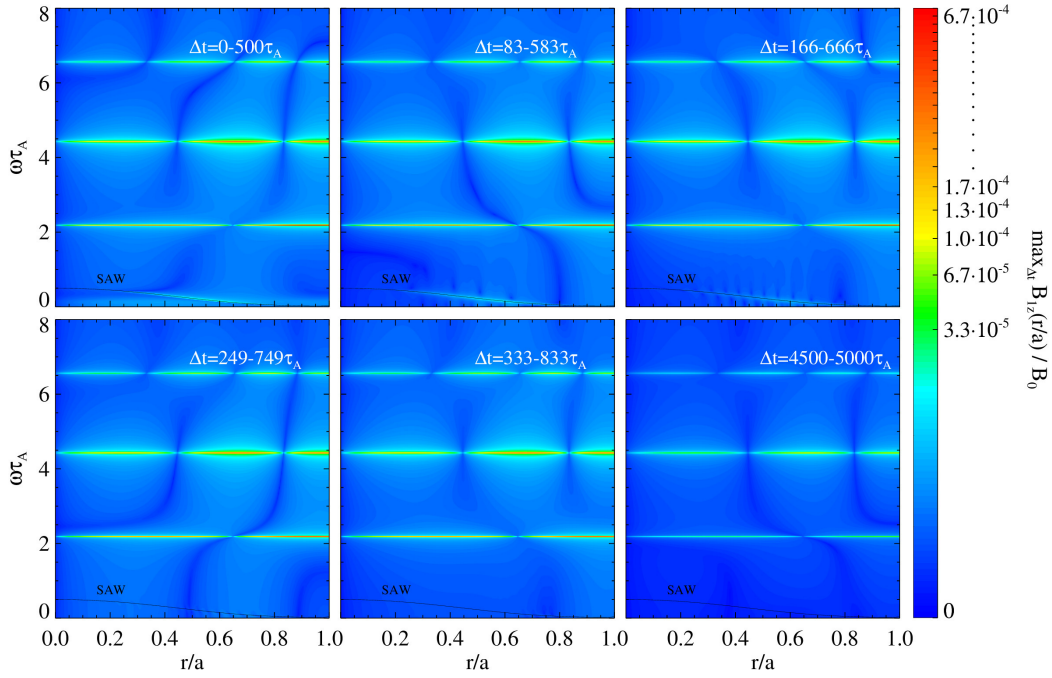

Figure 8.27: Simulation with RFP-like magnetic field and hollow density profile. $(m,n) = (0,2)$ mode with initial v_r perturbation. Time evolution of the frequency spectrum of the normalized magnetic field component B_{1z} at the beginning of the simulation (panels 1-5) and the end of the simulation (panel 6).[5]

[4]The movie of $(m,n) = (4,4)$ mode with uniform density profile can bee seen at the following link: https://www.dropbox.com/s/5i1vdw9mbja6l1k/Bz_var_pertvr_m4n4.mp4?dl=0

[5]The corresponding movie can bee seen at the following link: https://www.dropbox.com/s/zdb10ez0dic7sz1/Bz_var_denn_pertvr_m0n2.mp4?dl=0.

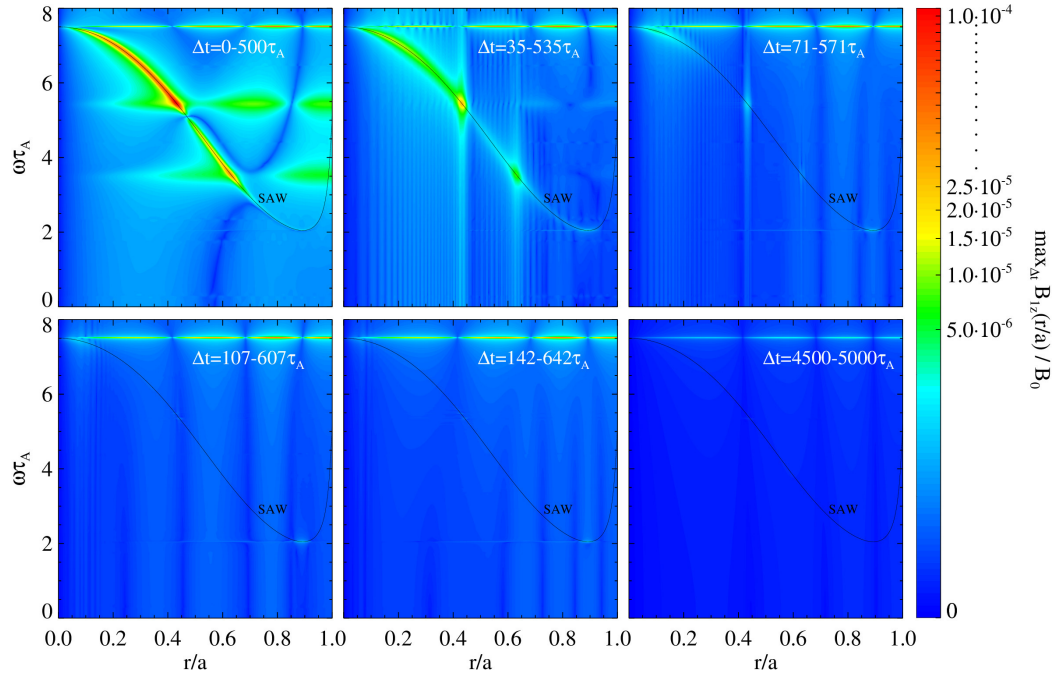

Figure 8.28: Simulation with RFP-like magnetic field and hollow density profile. $(m,n) = (4,4)$ mode with initial v_r perturbation. Time evolution of the frequency spectrum of the normalized magnetic field component B_{1z} at the beginning of the simulation (panels 1-5) and the end of the simulation (panels 6).[6]

8.3.3 Center-peaked density profile

We now come back to the characterization of the GAE, that is the discrete global mode that is expected to be found whenever the Alfvén continuum has a minimum inside the plasma, as discussed in Section 6.2.3. We have discussed the first case where this condition is satisfied, namely the academic RFP case with hollow density profile, in Section 8.3.2. In that case, however, a clear indication of the GAE solution was not found. In order to try to excite the GAE mode, we investigated the five equilibrium density profiles shown in Figure 7.12. In particular we considered density profiles with different position of their peak density, going from the wall to the plasma center. In the next Subsection, we will accurately examine the density profile that is most efficient to excite the GAE mode, namely the center-peaked density profile (a), afterwards we will show a summary graph with all density profiles.

[6]The corresponding movie can bee seen at the following link:
https://www.dropbox.com/s/yxr7r4t6y53vdbo/Bz_var_denn_pertvr_m4n4.mp4?dl=0.

8.3.3.1 $(m,n) = (1,0)$ mode with initial v_r perturbation

The frequency spectrum resulting from the SpeCyl simulation with perturbed (m,n)=(1,0) mode and center-peaked density profile is shown in Figure 8.29, while in Figure 8.30 we superimpose the resulting numerical spectrum with the expected theoretical one (Fig. 7.13) in order to identify the various frequencies. As we can see now we observe a new global mode near the Alfvén continuum minimum, that is the GAE. Indeed, by looking for instance at Figure 8.30 we see a global discrete mode (marked by the dashed horizontal line) at the minimum frequency of the continuum spectrum.

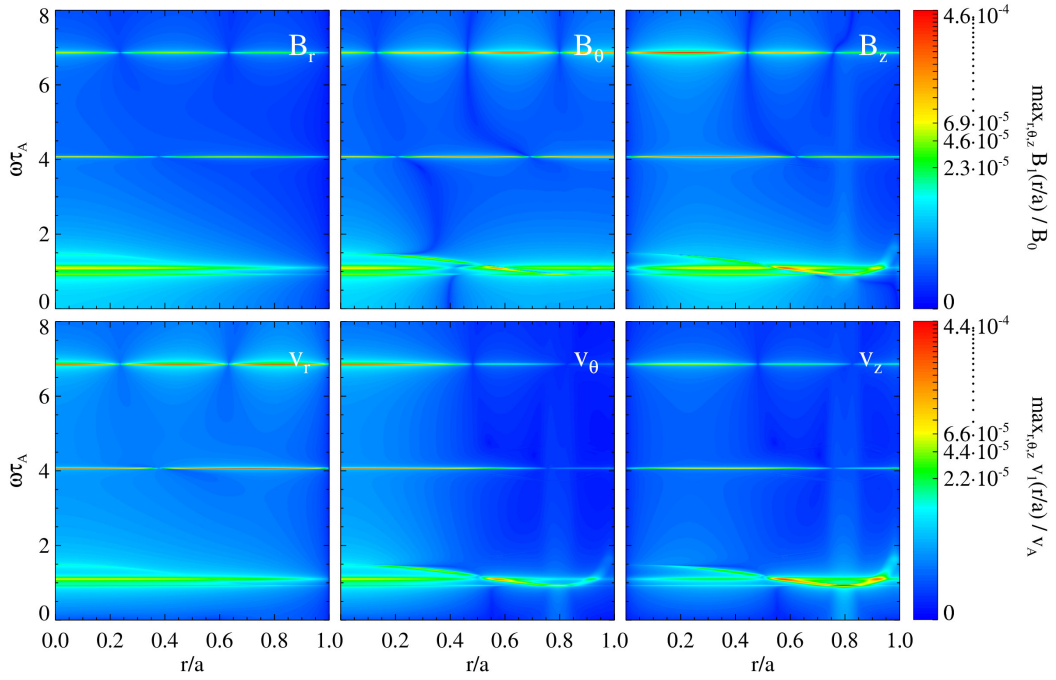

Figure 8.29: Simulation with RFP-like magnetic field and center-peaked density profile. $(m,n) = (1,0)$ mode with initial v_r perturbation. The frequency spectra of $\mathbf{v}_1$ and $\mathbf{B}_1$ normalized fields components are shown as a function of radius, as computed for the time window $t \in [0, 500\tau_A]$.

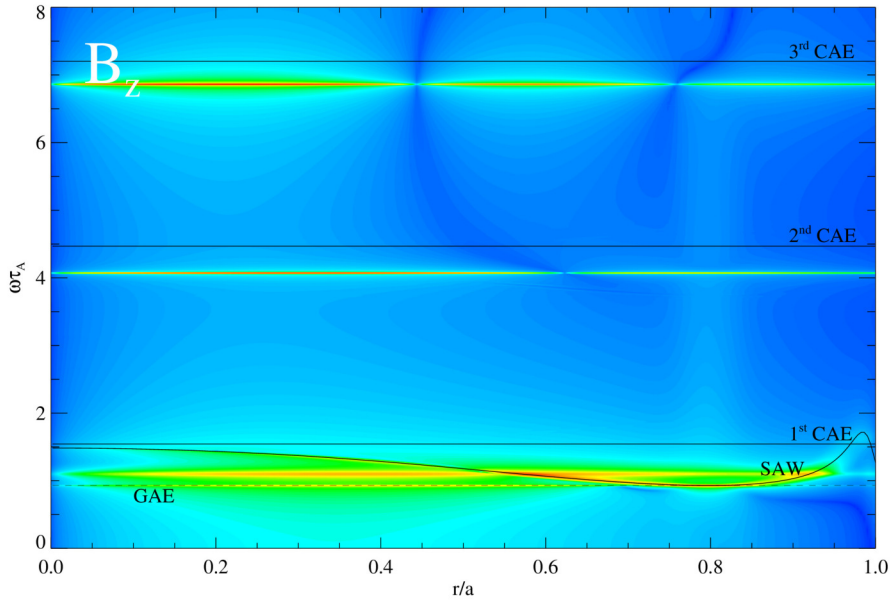

Figure 8.30: Simulation with RFP-like magnetic field and center-peaked density profile. $(m,n) = (1,0)$ mode with initial v_r perturbation. Verification of frequency spectrum with the theoretical model for B_{1z} magnetic field component. The analytical curve of the GAE is dashed to avoid covering its spectrum.

Lets now look at the time evolution of the B_{1z} component, as shown in Figure 8.31. We can observe, as in previous cases, the phase mixing of the SAW and the resonance absorption of the 1^{st} CAE. Both waves disappear as before, but now the GAE mode survives even after the SAW is gone, and it takes the whole simulation for the GAE to disappear as well.

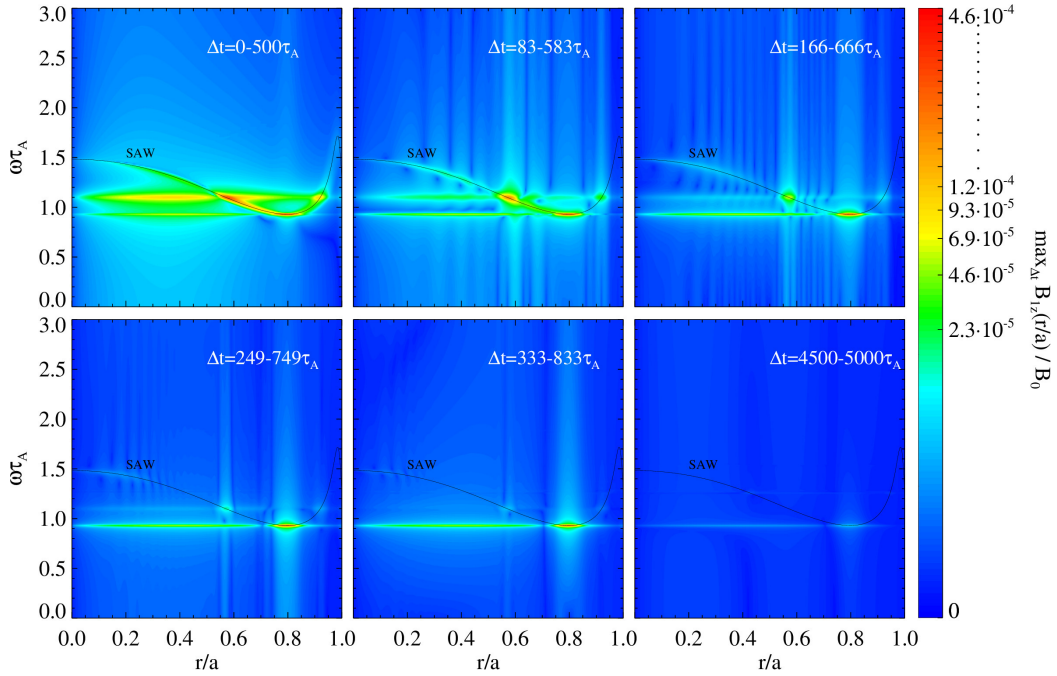

Figure 8.31: Simulation with RFP-like magnetic field and center-peaked density profile. $(m,n) = (1,0)$ mode with initial v_r perturbation. Time evolution of the frequency spectrum of the normalized magnetic field component B_{1z} at the beginning of the simulation (panels 1-5) and the end of the simulation (panel 6).[7]

Let’s also look at the time evolution at fixed radius, as reported in Figure 8.32. We can see that now, unlike the case with hollow density profile, the damping rate of the resonance absorption is very high since the 1^{st} CAE is completely damped in the same time as SAW, while the GAE is just weakly damped and remain over the entire simulation.

In Figure 8.33 we verify that the GAE is actually a global eigenmode. Solid dots indicate the absolute value of the amplitude of the normalized magnetic field component B_{1z} at the frequency corresponding to the GAE. We see that indeed the GAE takes a finite amplitude not just close to the edge radial position where the minimum of the Alfvén continuum is located, but also up to the plasma center.

[7]The corresponding movie can bee seen at the following link:
https://www.dropbox.com/s/ye33wigaisxc30j/Bz_var_center_denn_pertvr_m1n0.mp4?dl=0.

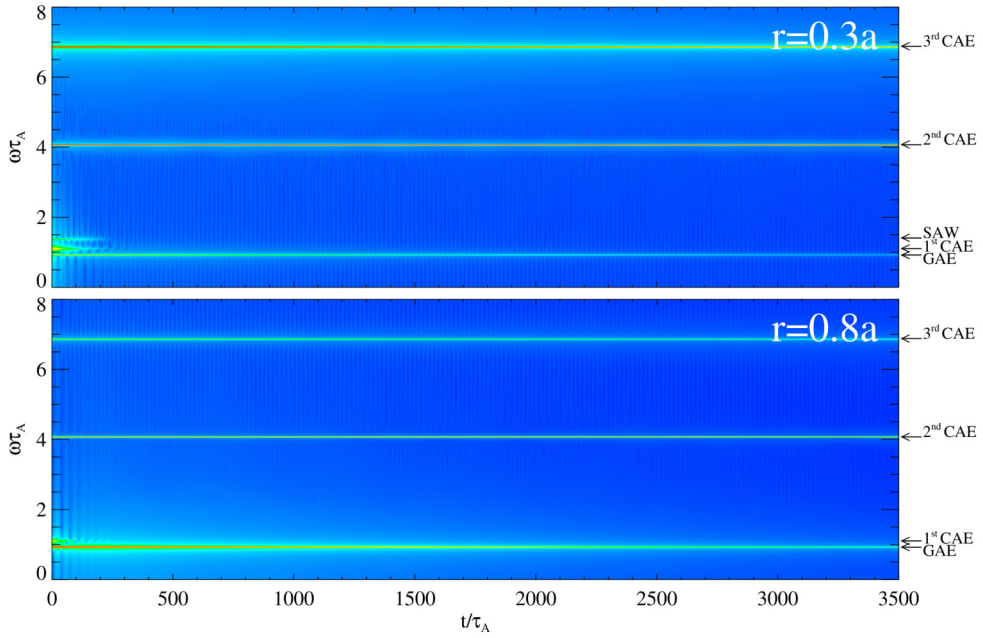

Figure 8.32: Simulation with RFP-like magnetic field and center-peaked density profile. $(m,n) = (1,0)$ mode with initial v_r perturbation. Time evolution of the frequency spectrum of the normalized magnetic field component B_{1z} at a fixed radius $r/a = 0.3$ and $r/a = 0.8$.

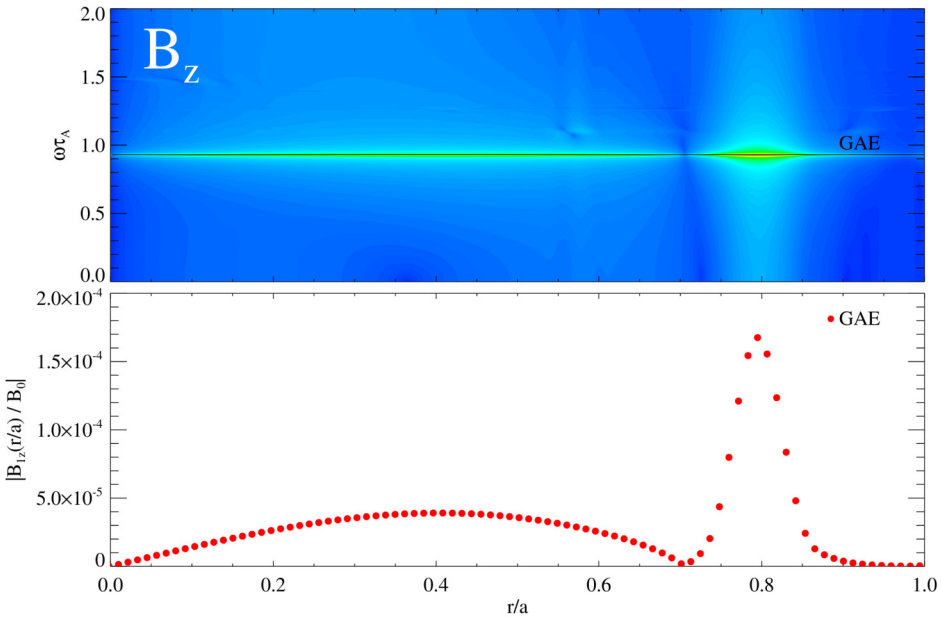

Figure 8.33: Simulation with RFP-like magnetic field and center-peaked density profile. $(m,n) = (1,0)$ mode with initial v_r perturbation. Verification of GAE being a global eigenmode. For the analysis was considered the time window $\Delta t = 400 - 900\tau_A$ in order to eliminate the contribution to the spectrum of the 1^{st} CAE and continuous SAW.

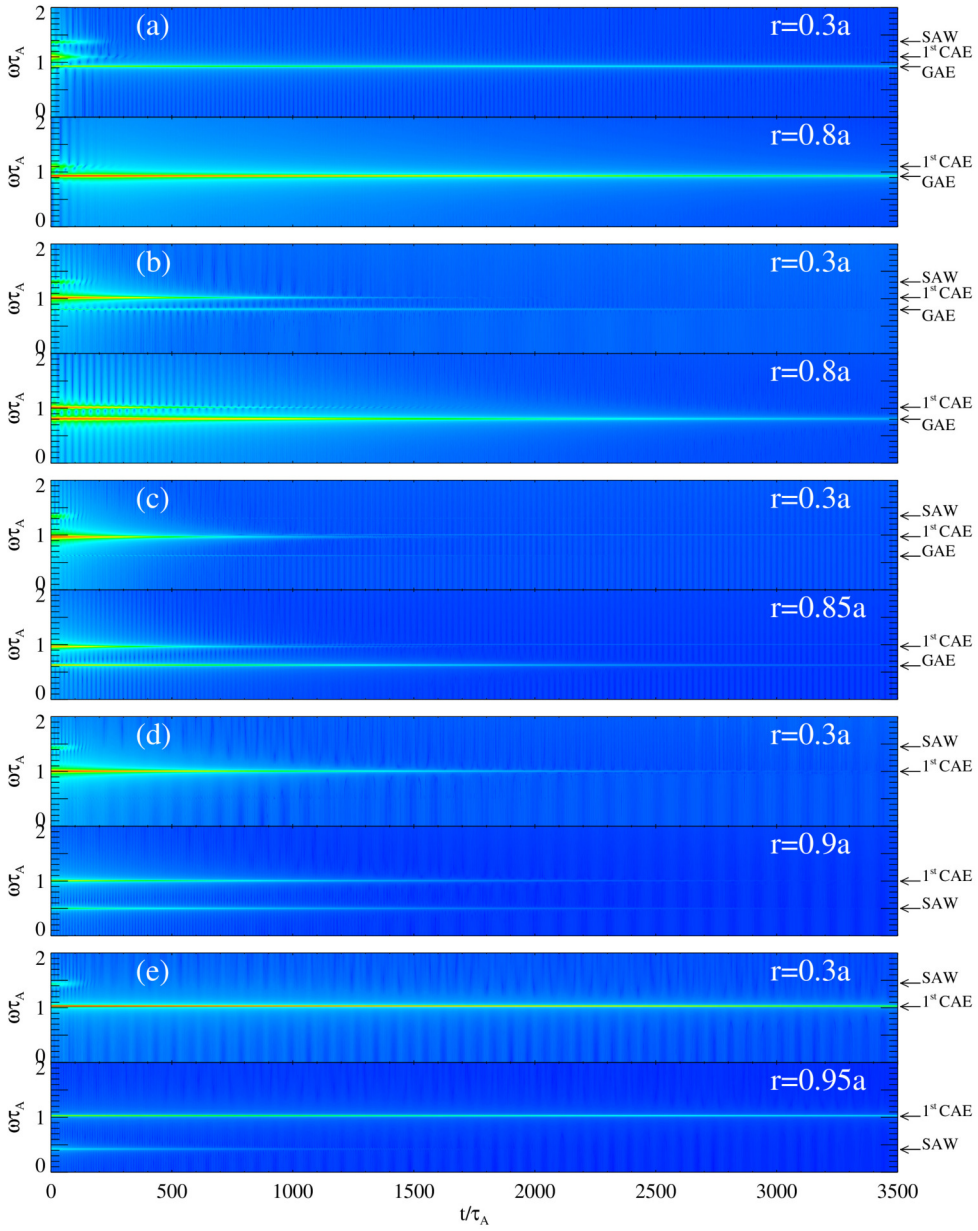

Figure 8.34: Simulations with RFP-like magnetic field and five different density profiles. $(m,n) = (1,0)$ mode with initial v_r perturbation. Time evolution of the frequency spectrum of the normalized magnetic field component B_{1z} at a fixed radius $r/a = 0.3$ and $r/a = 0.8 - 0.95$ for all the density profiles from Fig. (7.12).

The case we have just discussed, with density profile peaked in the center, is the one in which the GAE mode is most excited. In Figure 8.34 we show a summary plot for all density profiles from Figure 7.12. We can see that moving the peak density from the center, panel (a), to the wall of the cylinder, panel (e), the resonance absorption of the 1^{st} CAE is less and less effective, until it disappears for the (e) density profile, where the 1^{st} CAE survives over the entire simulation and is slightly damped only due to resistivity. We can also note an opposite trend for the GAE, which is less and less excited moving the density peak from the center to the edge. This confirms that the GAE mode is more easily excited with density profiles peaked near the plasma center. The SAW damping rate due to phase mixing seems to be independent of the density profile.

8.4 Effect of resistive dissipation

Before concluding this Section on "academic" RFP simulations, let's examine how the amplitude of the 1^{st} CAE, SAW and GAE evolve in time for different values of Lundquist number $S = \tau_R/\tau_A$, that it for different values of the dimensionless resistivity, while the dimensionless viscosity is kept constant at $M = \tau_V/\tau_A = 10^6$. In particular we analysed simulations with $(m,n) = (1,0)$ mode, RFX-mod like density profile and initial v_θ perturbation.

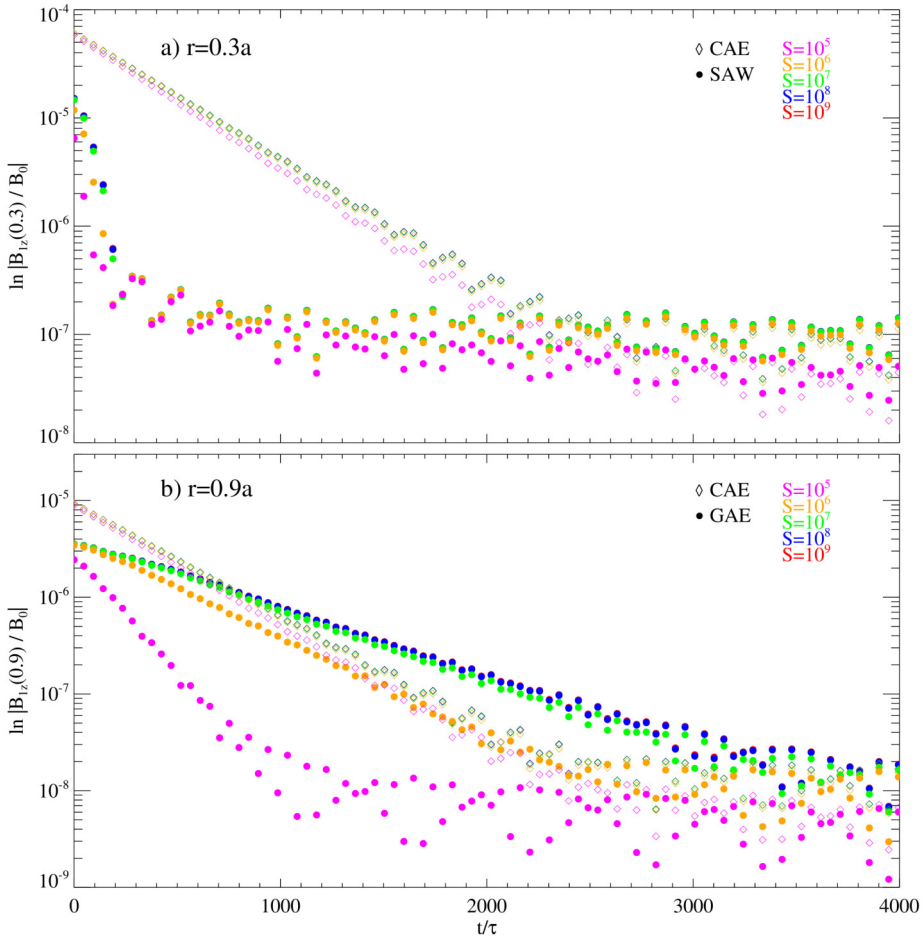

Figure 8.35: Simulations with RFP-like magnetic field and hollow density profile. $(m,n) = (1,0)$ mode with initial v_θ perturbation. Attenuation of CAE, SAW and GAE Alfvén modes due to the variation of the Lundquist number.

As we can see from Figure 8.35, the SAW and CAE modes do not seem to depend on resistivity, while on the contrary the GAE is less and less damped when increasing the Lundquist number , that is decreasing the resistive dissipation. In particular for $S \geq 10^7$ the GAE becomes the dominant mode after $\sim 700\tau_A$. Although in the following we will

return to consider only simulations with $S = 10^6$, this brief analysis shows the potential importance of the dissipative terms (resistivity and/or viscosity) for a correct qualitative and quantitative interpretation of the experimental observations.

8.5 "Realistic" time-evolving RFP configurations

Finally we consider the time-dependent mean magnetic field in a "realistic" RFP dynamical configuration, that is the closest to the experimental conditions we can presently achieve with the SpeCyl code, as exemplified in Figure 7.15. This is the highest sophistication level considered in this Thesis and will make possible a direct qualitative comparison with experimental observations in the RFX-mod device, as will be discussed in the next Section. In the following, we will first discuss a simulation case with uniform density and then a case with RFX-mod-like hollow density profile.
We will still focus on the $(m,n) = (1,0)$ mode as in the previous Section on the "academic" RFP case, but a fundamental difference is that now the nonlinear simulations include not just the $(1,0)$ mode as before, but a complete spectrum of modes as discussed in Section 5.2.
In this section we will consider simulations with a times step of $10^{-3}\tau_A$ and radial resolution of 100 points. The on-axis Lundquist and viscous Lundquist numbers are set to $S = 10^6$ and $M = 10^4$, respectively. This corresponds to Hartmann and Prandtl numbers $H = 10^5$ and $P = 100$, respectively. The on-axis resistivity and viscosity are the inverse Lundquist number $\eta_0 = \tau_A/\tau_R \equiv S^{-1}$ and the inverse viscous Lundquist number $\nu_0 = \tau_A/\tau_V \equiv M^{-1}$, respectively ($\tau_R$ and τ_V being the resistive and viscous time scales). ν is assumed to be uniform, while an increasing radial profile is assigned for η, of the form $\eta(r) = \eta_0[1 + 19(r/a)^{10}]$. In the simulations is used a wide spectrum of 225 modes with $0 \leq m \leq 4$. In particular for the $m = 0$ and $m = 1$ modes, which are the most important in the nonlinear RFP dynamics, we used $-25 \leq n \leq 1$ and $-55 \leq n \leq 10$, respectively. Furthermore we will consider a helical boundary condition on the edge B_r, opposed to ideal boundary conditions used in "academic" RFP simulations. Indeed, the addition of a helical perturbation of the edge radial magnetic field is considered in these simulations. This perturbation is chosen with $m = 1$, $n = -7$ periodicity and a constant in time amplitude around 2% of the mean edge field. Such boundary conditions provide a schematic representation of the plasma magnetic boundary during high current discharges in RFX-mod, as discussed in [Bonfiglio et al., 2013].

8.5.1 Uniform density $\rho_0 = 1$

8.5.1.1 $(m,n) = (1,0)$ mode

Up to now we have analyzed the simulations starting from the initial time in which was applied the velocity perturbation. Now instead we will consider a time window (away from the beginning of the simulation) centered around a typical magnetic reconnection event. In particular we first discuss the frequency spectrum corresponding to the time

window $\Delta t = 4500 - 5000\tau_A$[8], centered around the magnetic reconnection event shown in the bottom panel of the Figure 7.14 of Chapter 7. This spectrum is reported in Figure 8.36, and shows intense low-frequency fluctuations in all the magnetic field and velocity components, but also weaker discrete signals (horizontal lines) which can be recognized in particular in the radial components of both magnetic field and velocity. In this case the colorbar was calibrated with respect to v_{1r} component as it presents the most clear spectrum. The low-frequency fluctuations, which are stronger in θ and z components of the fields, are due to low-frequency tearing modes which dominate the dynamic of the system in this configuration. The discrete signals, on the other hand, can be identified as Alfvén modes as we now discuss.

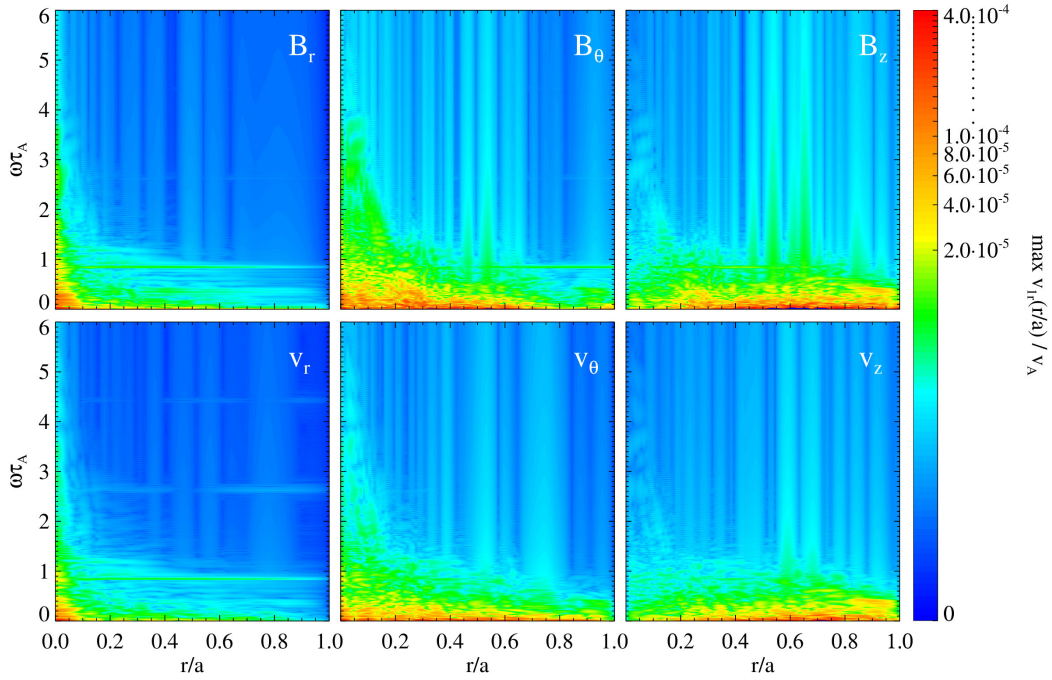

Figure 8.36: Simulation with "realistic" time-evolving RFP magnetic field and uniform density. $(m,n) = (1,0)$ mode. The frequency spectra of $\mathbf{v}_1$ and $\mathbf{B}_1$ normalized fields components are shown as a function of radius for a time window around the magnetic reconnection event.

In Figure 8.37 we superimpose the frequency spectrum of v_{1r} component with the expected one (Fig. 7.17) in order to identify the various Alfvénic frequencies. We can recognize the first three CAE frequencies, the first one being the most excited while the third being barely visible. We also note that we don't see the SAW frequency. This can

[8]The time intervals considered in this Section are rescaled to the beginning of the particular simulation centered around the magnetic reconnection event taken into consideration. In this case the time window $\Delta t = 4500 - 5000\tau_A$ corresponds to $\Delta t = 34500 - 35000\tau_A$ in Figure 7.14.

be explained by looking at the “academic” RFP simulations discussed before. Indeed the SAW spectrum was always very weak in the r component of the fields. Moreover in this case besides being weak it’s also covered up by the low-frequency fluctuations. In order to indirectly confirm the SAW presence in "realistic" RFP simulations, we will analyse in the following a similar "realistic" simulation but with RFX-mod-like hollow density profile, to try to detect the GAE, which derives from the SAW mininum as discussed in Section 6.2.3.

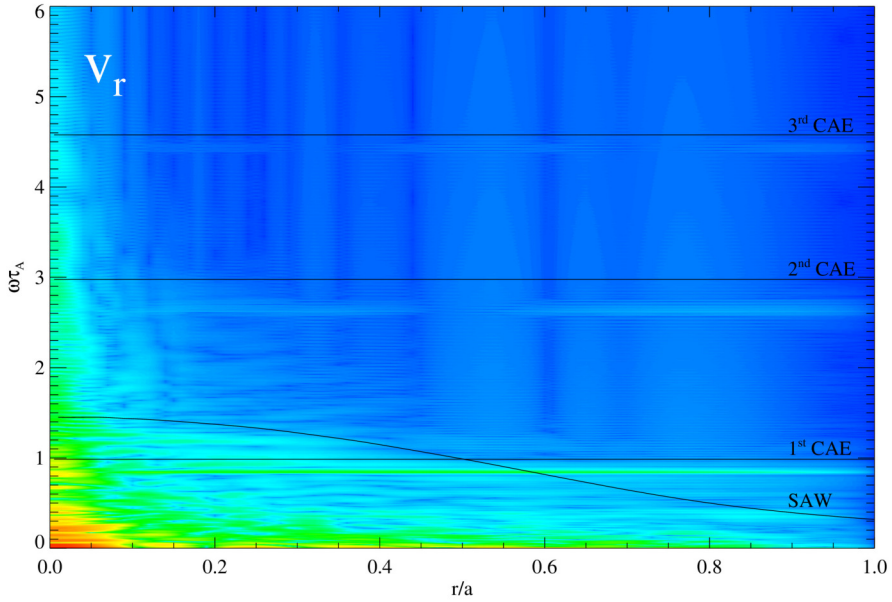

Figure 8.37: Simulation with “realistic” time-evolving RFP magnetic field and uniform density. $(m,n) = (1,0)$ mode. Verification of frequency spectrum in the middle of the magnetic reconnection event with the theoretical model for v_{1r} velocity field component.

We now discuss the time evolution of v_{1r} component, as shown in Figure 8.38. This figure confirms that the Alfvénic modes are excited by the magnetic reconnection event itself, in fact they are absent just before it (panel 1). The Alfvénic modes disappear again after some thousand Alfvén times after the magnetic reconnection event (panel 6), due to the various damping mechanisms already discussed for "academic" RFP simulations. The numerical result we have obtained, showing that Alfvén waves can be excited by magnetic reconnection events, is quite important because it provides a theoretical confirmation of experimental observations in the RFX-mod device, where the same qualitative phenomenology (with Alfvénic fluctuations excited after reconnection events) is found.

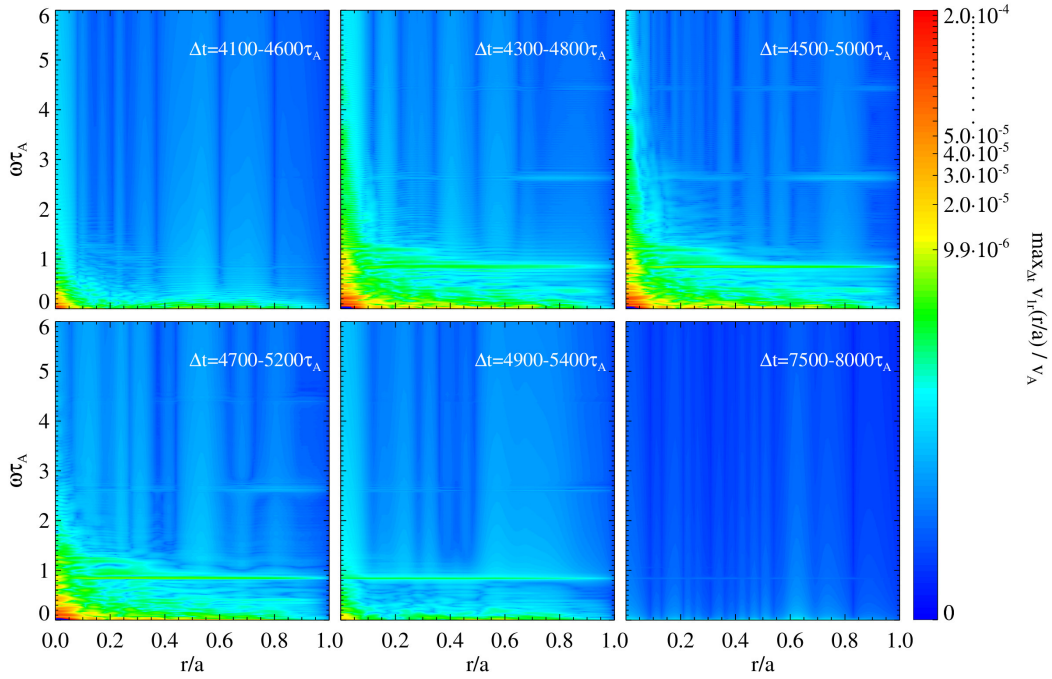

Figure 8.38: Simulation with "realistic" time-evolving RFP magnetic field and uniform density. $(m,n) = (1,0)$ mode. Time evolution of the frequency spectrum of the normalized velocity field component v_{1r} just before (panel 1) during (panels 2-5) and long after (panel 6) the magnetic reconnection event.[9]

Finally we look at the time evolution at fixed radius $r/a = 0.6$ of v_{1r} component as shown in Figure 8.39, where we also plot the time trace of B_{0z} normalized magnetic field component at the wall of the cylinder and the corresponding trend of kinetic and magnetic energy. As it is theoretically expected (see Section 4.1.4), during the magnetic reconnection event, starting around $t = 4000\tau_A$, we have a drop in magnetic energy while the kinetic one rises. In addition, clearly the excitation of the CAEs happens during the event, after which they are damped in time, with only the 1^{st} CAE being able to remain for some time after the event.

[9]The corresponding movie can bee seen at the following link:
https://www.dropbox.com/s/xyxpqlqjrnw4wzl/Vr_m1_n0_realistic_case.mp4?dl=0.

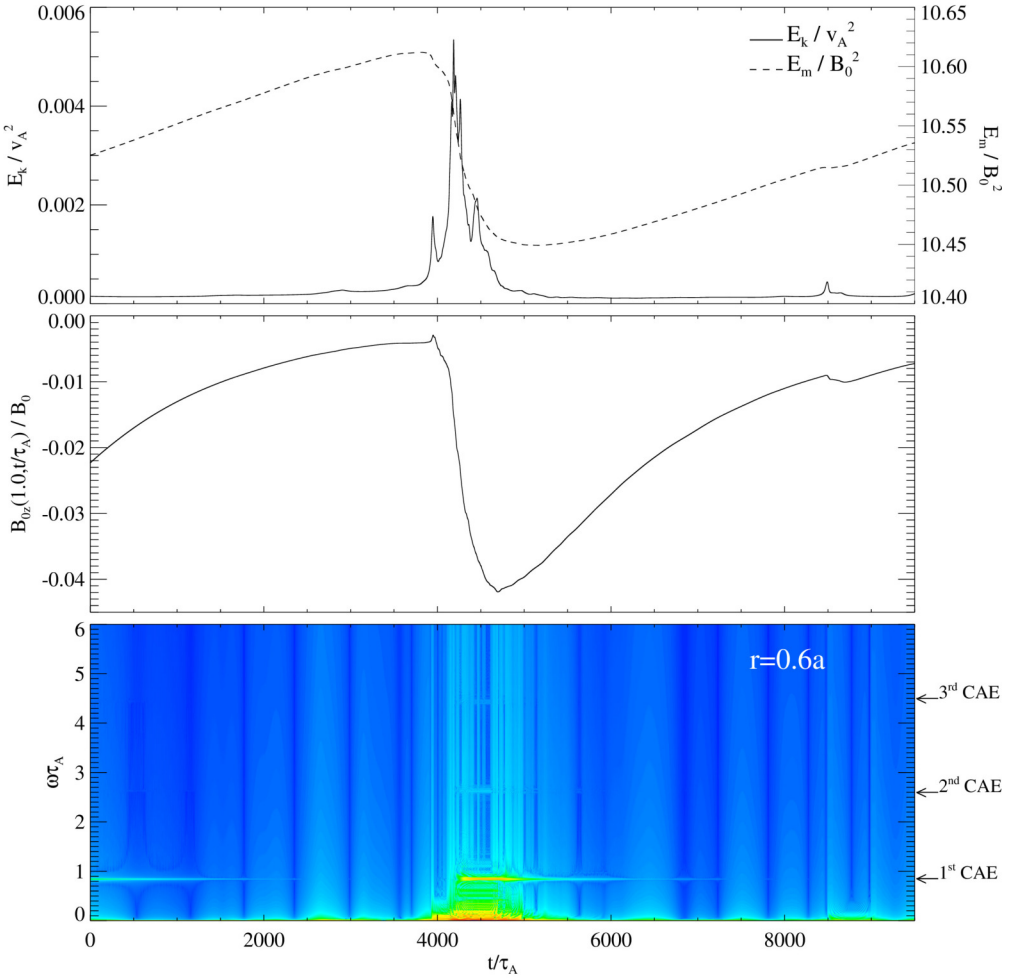

Figure 8.39: Simulation with "realistic" time-evolving RFP magnetic field and uniform density. $(m,n) = (1,0)$ mode. (Top) The time trace of the normalized kinetic energy E_k and normalized magnetic energy E_m. (Middle) The time trace of the normalized magnetic field component B_{0z} at a fixed radius $r/a = 1.0$. (Bottom) Time evolution of the frequency spectrum of the normalized velocity field component v_{1r} at a fixed radius $r/a = 0.6$. The color scale has been adjusted, compared to the Fig. 8.37, to better highlight the CAEs.

Excitation of Alfvénic modes for different Fourier harmonics (m,n)

As we mentioned before, we have chosen to analyse the $(m,n) = (1,0)$ harmonic because it is the one in which the Alfvénic modes are most excited. We can clearly see this from Figure 8.40 in which we plotted the 1^{st} CAE amplitude for a wide range of Fourier modes, in particular $-1 \leq m \leq 1$ and $-9 \leq n \leq 9$ (technically we analysed only half of those modes as the other half derives from the symmetry condition (5.6)). This numerical observation is also in agreement with experimental observations [Spagnolo et al., 2011]

in the RFX-mod experiment, where the poloidal and toroidal periodicities of the measured Alfvénic fluctuations can be reconstructed and appear to be consistent with a dominant $m = 1$, $n = 0$ component.

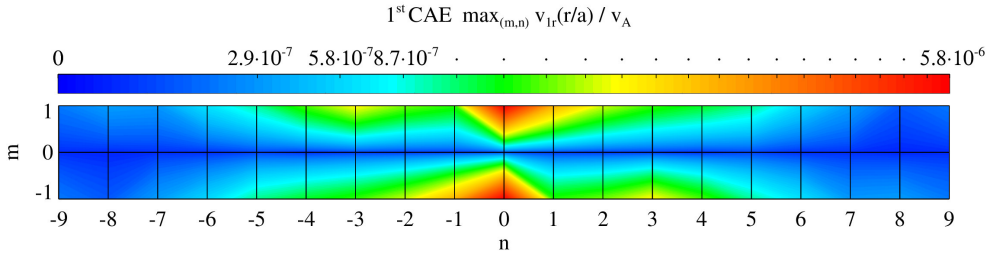

Figure 8.40: Simulations with "realistic" time-evolving RFP magnetic field and uniform density. The variation in the amplitude of the 1^{st} CAE for different harmonics (m,n).

8.5.2 RFX-mod-like hollow density profile

8.5.2.1 $(m,n) = (1,0)$ mode

The same analysis of the previous Section was made for a nonlinear MHD simulation with same setup and similar temporal evolution of the mean magnetic field, but with a hollow density profile typical of RFX-mod discharges at high plasma current. In particular the analysis was performed on the magnetic reconnection event centered around $t = 3.9 \times 10^4\ \tau_A$, shown in the bottom panel of the Figure 7.18 of Chapter 7. As before, in this Section the time intervals are rescaled to the beginning of the particular simulation centered around the magnetic reconnection event taken into consideration. In this case the beginning of the simulation corresponds to $t = 3.6 \times 10^4\ \tau_A$ in Figure 7.18.
Lets start by analysing the frequency spectrum corresponding to the time window $\Delta t = 2500 - 3000 \tau_A$, centered around the magnetic reconnection event. This spectrum is reported in Figure 8.41. Compared with the previous case with uniform density (Fig. 8.36), low-frequency fluctuations are slightly more intense, especially closer to the center. As before we note the discrete signals, in particular in the radial components of both magnetic field and velocity, which correspond to the CAE modes. In general the qualitative picture is similar to the previous case.

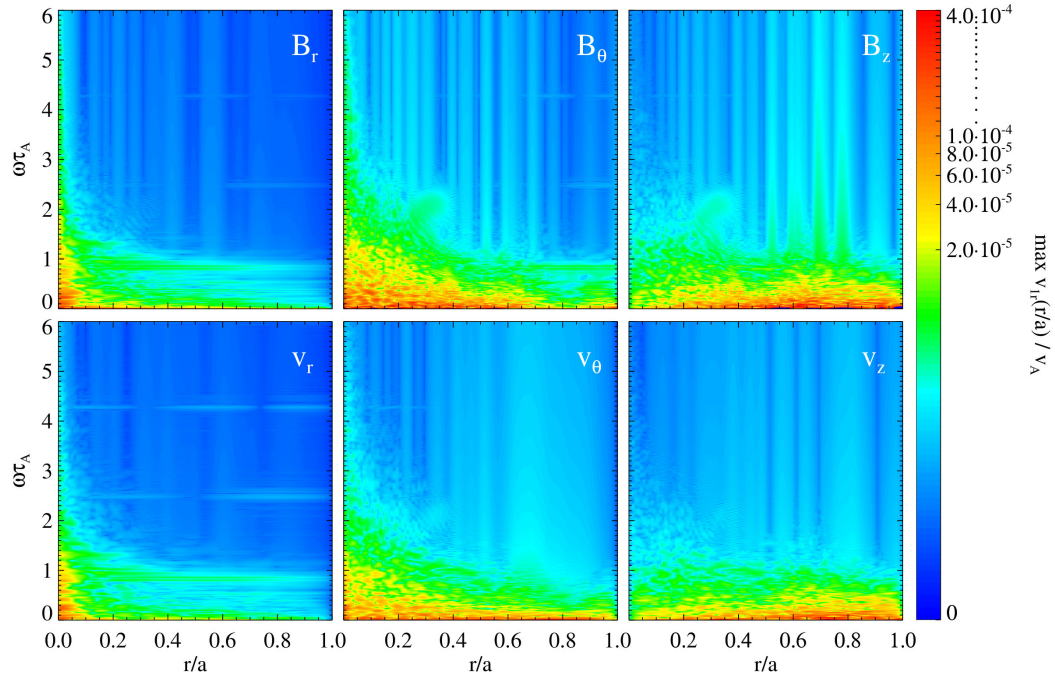

Figure 8.41: Simulation with "realistic" time-evolving RFP magnetic field and RFX-mod-like hollow density profile. $(m,n) = (1,0)$ mode. The frequency spectra of $\mathbf{v}_1$ and $\mathbf{B}_1$ normalized fields components are shown as a function of radius for a time window around the magnetic reconnection event.

In Figure 8.42 we show the time evolution of the v_{1r} component. As previously (Fig. 8.38) the Alfvénic modes are excited by the magnetic reconnection event itself, while before (panel 1) and after (panel 6) it there is no Alfvénic activity. Note that right after the reconnection event (panel 5), when the low-frequency fluctuations are gone, a faint discrete signal can be seen around $\omega\tau_A = 0.5$. As will be shown below this is the GAE mode, which is expected to be excited in this case of hollow density profile, as discussed in Chapter 7.

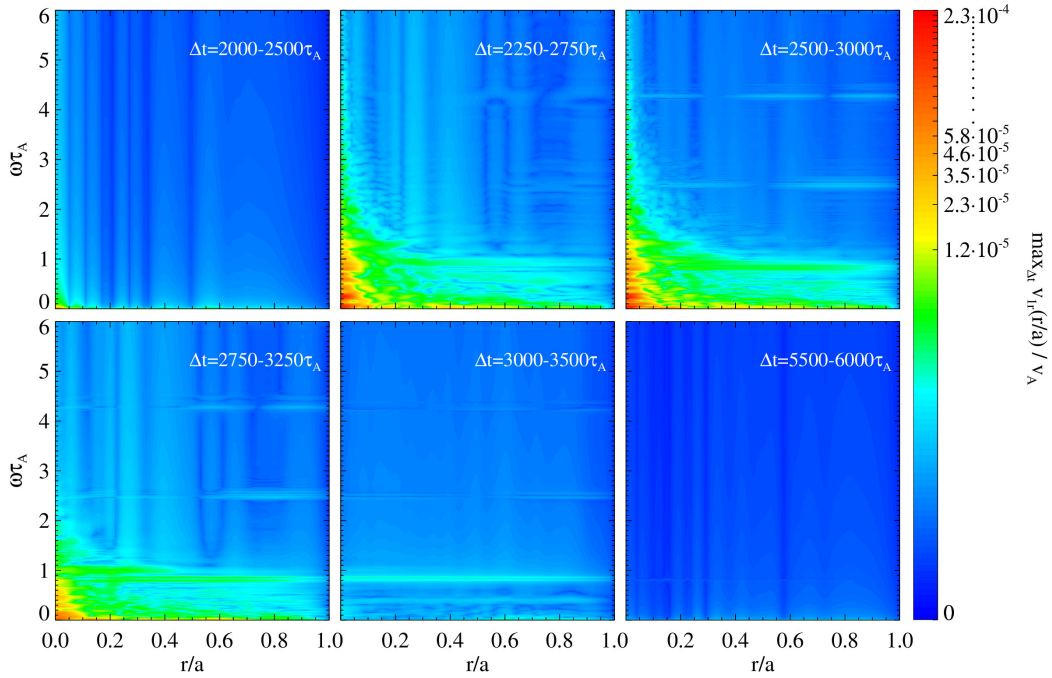

Figure 8.42: Simulation with "realistic" time-evolving RFP magnetic field and RFX-mod-like hollow density profile. $(m,n) = (1,0)$ mode. Time evolution of the frequency spectrum of the normalized velocity field component v_{1r} just before (panel 1) during (panels 2-5) and long after (panel 6) the magnetic reconnection event.[10]

In Figure 8.43 we superimpose the frequency spectrum of v_{1r} component with the expected one (Fig. 7.19) in order to identify the various Alfvénic frequencies (the color scale for this figure was saturated in order to better highlight the presence of the GAE). We recognize the first three CAE frequencies, with similar frequency values as in the previous uniform case (Fig. 8.37). Now however we also recognize the GAE mode, which also indirectly confirms the presence of the continuous SAW, which we were not able to check with the previous simulation due to the low frequency fluctuations covering its signal.

[10]The corresponding movie can bee seen at the following link:
https://www.dropbox.com/s/o182qaef77b8g6y/Vr_m1_n0_denn_realistic_case.mp4?dl=0.

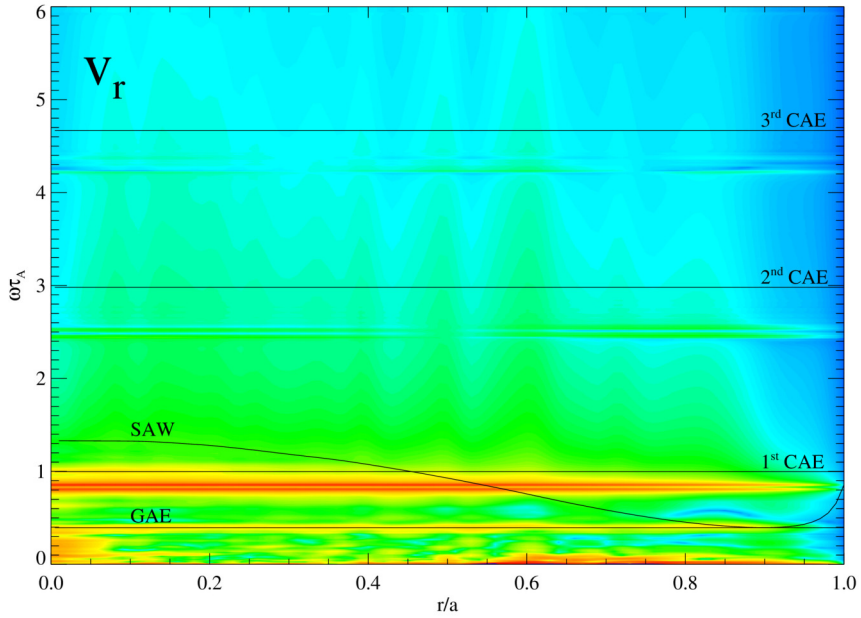

Figure 8.43: Simulation with "realistic" time-evolving RFP magnetic field and RFX-mod-like hollow density profile. $(m,n) = (1,0)$ mode. Frame with $\Delta t = 3000 - 3500\tau_A$ from the Fig. 8.42. Verification of frequency spectrum in the middle of a magnetic reconnection event with the theoretical model for v_{1r} velocity field component. The color scale has been adjusted, compared to the Fig. 8.42, to better highlight the presence of the GAE.

By looking at the time evolution at the fixed radius $r/a = 0.6$ of v_{1r} component, shown in Figure 8.44, we can see that the GAE is weak and is damped in time rather quickly, while the 1^{st} CAE is damped more quickly compared to the uniform density case (Fig. 8.39) due to resonance absorption process. Those observations are in agreement with the corresponding "academic" RFP configurations discussed before.

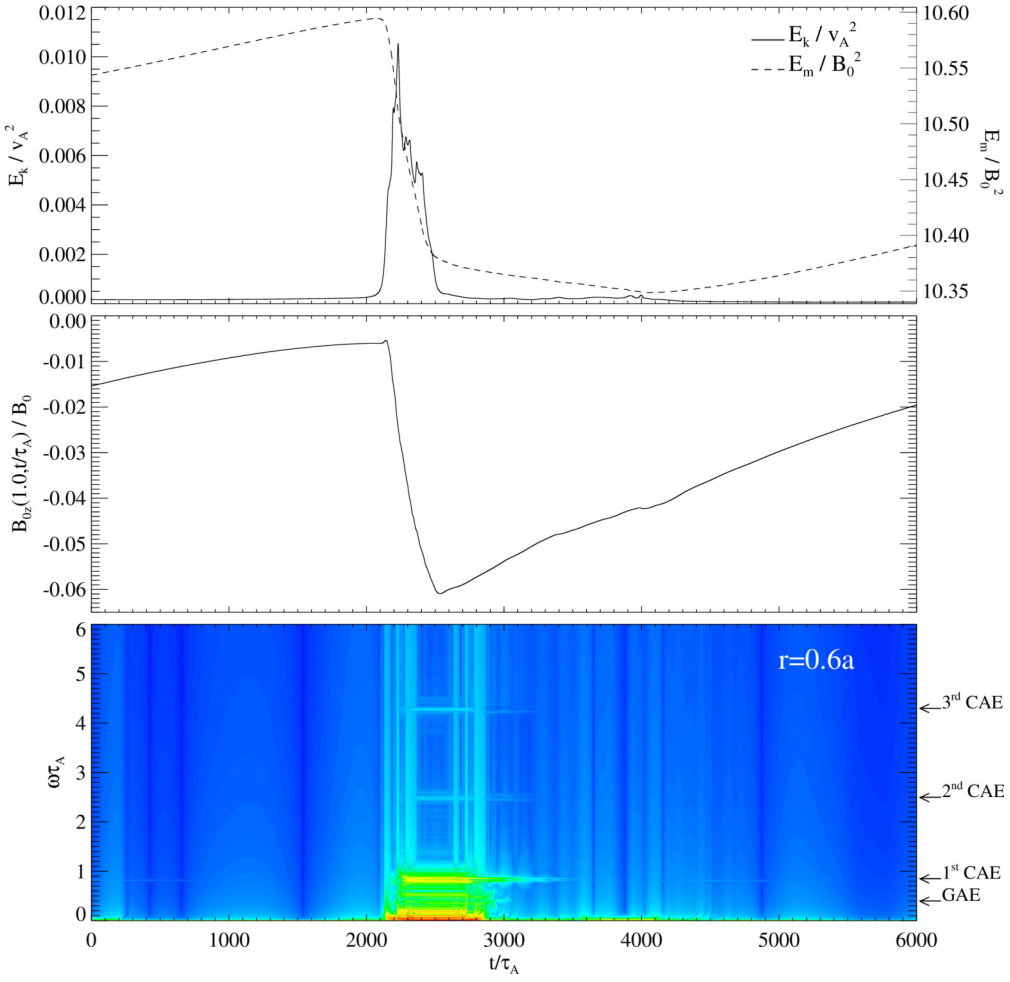

Figure 8.44: Simulation with "realistic" time-evolving RFP magnetic field and RFX-mod-like hollow density profile. $(m,n) = (1,0)$ mode. (Top) The time trace of the normalized kinetic energy E_k and normalized magnetic energy E_m. (Middle) The time trace of the normalized magnetic field component B_{0z} at a fixed radius $r/a = 1.0$. (Bottom) Time evolution of the frequency spectrum of the normalized velocity field component v_{1r} at a fixed radius $r/a = 0.6$. The color scale has been adjusted, compared to the Fig. 8.42, to better highlight the CAEs.

8.6 Comparison with experimental observations

We now conclude this Chapter, on numerical results from nonlinear MHD modelling, with a qualitative comparison of numerical RFP results with experimental observations on the RFX-mod device. As discussed in Section 3.3, five distinct peaks have been observed in the power spectrum of the magnetic fluctuation measured at the plasma edge of RFX-mod

device (Figure 3.5). These peaks have been named a, b, c, d and e following the increase of their frequency, from ~ 130 kHz to ~ 1 MHz. While the first three peaks (a,b,c) are present only during the SHAx state, in which the plasma is in an almost stationary equilibrium with helical symmetry with a single magnetic axis, as discussed in Section 3.2, the two highest frequency peaks, d and e, do not seem to be associated to any particular behavior of the dominant mode, being present during almost the full discharge duration. All of these peaks are interpreted as Alfvén waves because their frequencies scale linearly with the Alfvén velocity of the plasma, as shown in Figure 3.7.

We will give now an interpretation of those experimental observations, based on the results of the analysis carried out in this Thesis. In particular we want to compare the experimental findings with the analysis results of the most sophisticated and the closest to the experimental conditions simulation, that is the one with the "realistic" time-evolving RFP magnetic fields with hollow-like density profile, discussed in the previous section.

We start by comparing the frequencies of the experimentally observed Alfvén waves (the five peaks) with the frequency spectrum of the "realistic" simulation from Figure 8.43. In order to so we first need to plot the numerical frequency spectrum in physical units, as until now we have always considered dimensionless units. By tacking the RFX-mod minor radius $a = 0.459$ m and a reference Alfvén speed of $v_A = 2500$ km/s, we obtain the following Alfvén time $\tau_A = a/v_A \simeq 0.2\ \mu$s. The resulting frequency spectrum in physical units is shown in Figure 8.45, where we indicated the Alfvénic nature of the discrete signals, identified in the previous Sections. On the other hand, in Figure 8.46 we mark the frequencies of d and e peaks corresponding to the reference Alfvén speed.

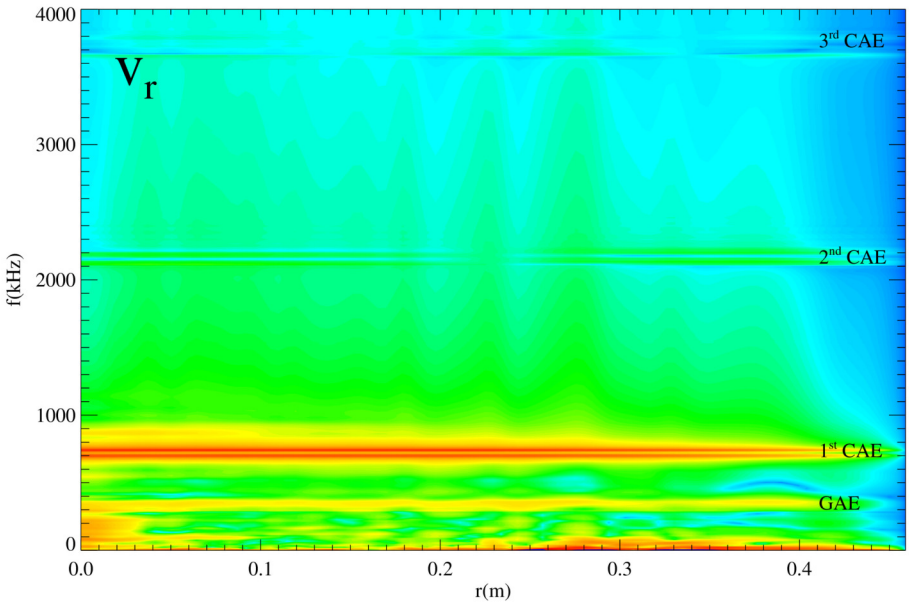

Figure 8.45: Simulation with "realistic" time-evolving RFP magnetic field and RFX-mod-like hollow density profile. $(m,n) = (1,0)$ mode. Frame with $\Delta t = 3000 - 3500\tau_A$ from the Fig. 8.42. Frequency spectrum, in the middle of a magnetic reconnection event, in physical units by tacking $v_A = 2500$ km/s and minor radius of RFX-mod $a = 0.459$ m.

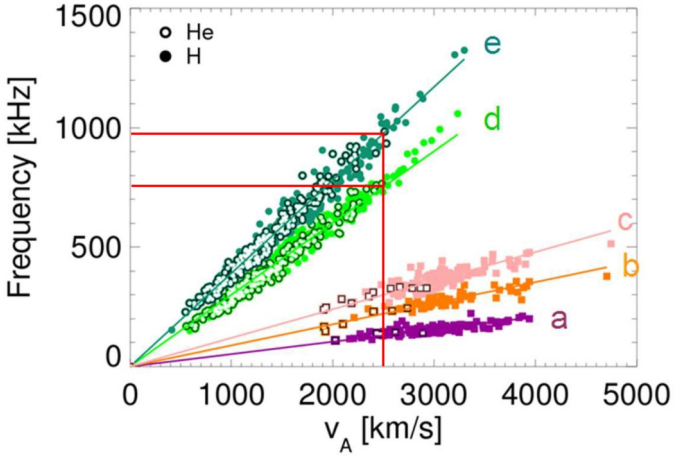

Figure 8.46: Relation between modes frequency and Alfvén velocity for a large database of H and He plasmas (from [Spagnolo et al., 2011]). In red is marked the frequency for peaks d and e corresponding to the Alfvén velocity $v_A = 2500$ km/s.

Comparing the two previous plots, we immediately notice that the GAE and the 1^{st} CAE frequencies values appear in the same frequency range of d and e peaks, with comparable separation between them. This brings us to formulate the following hypothesis on the Alfvénic nature of those peaks, namely that d corresponds to a GAE mode, while e corresponds to the 1^{st} CAE. Moreover this tells us the physical mechanism from which these Alfvén waves (d and e peaks) arise. Indeed from analysing the "realistic" simulations, we have found out that the Alfvén modes, such as CAE and GAE, are excited by the reconnection magnetic events. The phenomenon of periodic magnetic reconnection events is also found in the RFX-mod discharges from which the data in Figure 8.46 were taken. We can see the signature of those events in the power spectrum of the magnetic fluctuation in Figure 3.4. Thus we can conclude that the Alfvén waves corresponding to the d and e peaks are physically excited by the magnetic reconnection events taking place in the plasma. We also point out the resemblance of the experimental frequency spectrum in time during a magnetic reconnection event of Figure 3.4 and the numerical one in Figure 8.44. In particular similarly to the experimental spectrum, in the numerical one during a reconnection event we can also see the vertical bright lines, which are a global (i.e. at all frequencies) enhancement of the fluctuation level. As mentioned before, the d and e peaks are present during almost the full discharge duration, while the numerical one are excited only during the reconnection events, after which they decay more or less quickly in time, especially in case of the hollow-like density profile because of resonance absorption. This discrepancy can be explained by taking into account the kinetic effects,

which were not considered in the ideal MHD numerical simulations. In fact, as discussed in Section 4.1.4, we know that the reconnection magnetic events generate high energy particles which in turn are known ([Vlad, Zonca, and Briguglio, 2008]) to excite the Alfvén waves in the plasma. Thus physically the experimental Alfvén waves (d and e peaks) are excited by each reconnection event and sustained by the energetic particles in between them, allowing them to stay there during the full discharge duration. Kinetic effects are also most likely the reason why we didn't observed the three peaks (a, b and c) in our numerical simulations. In fact as we can see from Figure 3.4, in $130-500$ kHz range, these Alfvén waves are excited *after* the reconnection events, most likely by the energetic particles.

At last, to further validate the numerical findings with respect to the experimental ones, we show below in Figure 8.47 the experimental frequency spectrum in time, of the derivative of the poloidal magnetic field ($\dot{b}_\theta$) fluctuation at $r/a = 1$, in particular plasma conditions for which the d and e peaks are shifted in frequency from ~ 1 MHz to around 600 kHz, as can bee seen from the power spectrum in Figure 8.48. This shift allows us to see higher frequencies in the power spectrum, and as we can see a new faint signal (f peak) appears around $1,2$ MHz. By qualitatively comparing this spectrum with the numerical one in Figure 8.45, the natural conclusion is to identify this new peak with the 2^{nd} CAE, both for its frequency value in relation to the d and e peaks and its lower amplitude, being much less excited that the e peak, similarly to the excitation of the 2^{nd} CAE compared to the 1^{st} one in Figure 8.45.

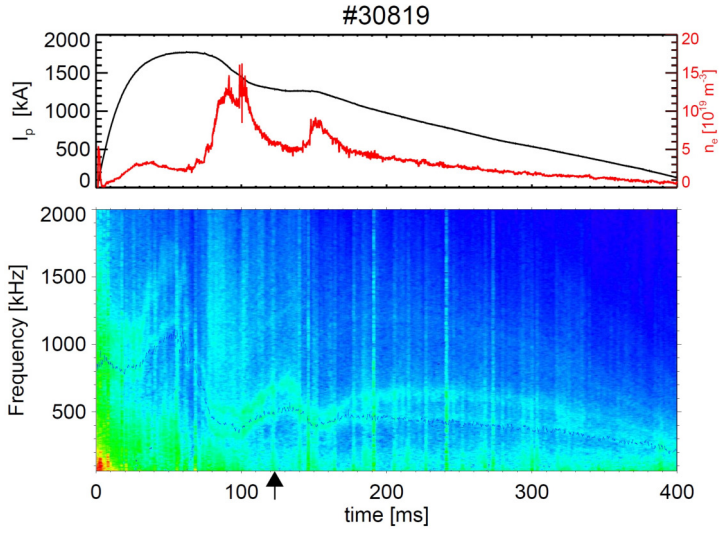

Figure 8.47: Top: plasma current I_p time trace; bottom: spectrogram of a $\dot{b}_\theta$ signal. The black arrows refer to the time instant for the analysis in Figure 8.48. [M. Zuin, private communication]

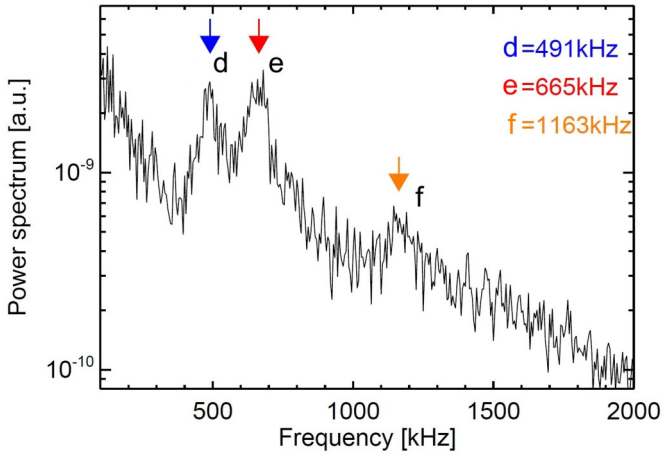

Figure 8.48: Power spectrum of a $\dot{b}_\theta$ signal evaluated during the time instant indicated by the arrow of Figure 8.47. [M. Zuin, private communication]

To conclude we have a qualitative agreement between the numerical simulations and the experimental observations of Alfvén waves in the RFX-mod device, and therefore we propose the following physical interpretation: in RFX-mod some Alfvén waves are excited directly by the magnetic reconnection events occurring during the plasma discharge in which high energy particles are also generated, and afterwards they are sustained by these energetic particles in between the reconnection events. In particular, we have identified the experimental peaks d, e and (when observed) f as a GAE, the 1^{st} CAE, and the 2^{nd} CAE, respectively.

Part IV

Summary and conclusions

Summary and conclusions

The subject of this Thesis is a systematic theoretical investigation of the physics of Alfvén waves in magnetically confined thermonuclear plasmas, by means of analytical theory and numerical simulations based on the nonlinear 3D MHD model. The main goal of this research was to theoretically characterize the Alfvén waves in the RFP magnetic configuration, as presently the scientific studies in the context of Alfvén waves in fusion plasmas are mainly focused on the tokamak configuration, being the most promising for a fusion reactor, and less attention is devoted to the RFP. However, a renewed interest has been shown for this configuration in recent years because of the discovery, first theoretically and then experimentally in the RFX-mod device, of improved confinement helical states, the QSH states. An experimental characterization of Alfvén waves in the RFX-mod device showed the presence of several coherent modes with Alfvénic nature, but a theoretical interpretation of such experimental findings was still missing. The specific aim of this Thesis was to fill this gap and provide a qualitative physical interpretation of experimental observations.

The theoretical characterization of Alfvén waves performed in this Thesis was based on the analysis of nonlinear 3D MHD simulations in cylindrical geometry for different configurations of increasing complexity, and the interpretation of resulting frequency spectra through the ideal MHD model. It's important to note that the numerical simulations were obtained from a non-linear code, SpeCyl, which can give the plasma temporal evolution, unlike the linear stability codes widely used in literature that can just provide the frequency spectrum and related linear growth rates for a given magnetic configuration. The analysis started with an equilibrium configuration with uniform axial magnetic field and uniform density profile. This was the only case for which an exact analytical solution for Alfvénic modes SAW and CAE can be obtained from the theoretical models. The verification of the numerical frequency spectra with the theoretical ones showed complete agreement, thus demonstrating the applicability of the SpeCyl code as a well suited simulation tool for the study of Alfvén waves. As a second step, more complex configurations were analysed, first with non-uniform RFX-mod-like hollow density and then with slightly non-uniform magnetic fields (Tokamak-like configuration). In these cases the comparison with the theoretical models was done employing the WKB approximation for the CAE mode, as this mode does not possess an analytic solution for non uniform plasmas. The good agreement between numerical and theoretical spectra in this cases allowed us to be confident on the interpretation of numerical spectra for non-uniform cases. Furthermore the theoretically predicted phenomena for those cases, namely the damping mechanism

of the continuous SAW, called phase mixing, and the coupling between SAW and CAE modes, were observed.

After having analysed the previous cases, used as a first basic assessment of Alfvén waves in our MHD simulations, as a further step we analysed a simplified RFP-like equilibrium configuration of the magnetic fields, first with uniform and then with different variable density profiles. This case provided a first look at a more realistic representation of Alfvénic activity in an RFP plasma and was used as a training before going to the realistic simulation regime with time-evolving mean magnetic field. In particular this case showed us that in the RFP configuration a peculiar condition occurs, that is the direct coupling between the SAW continuum and the 1^{st} CAE, unlike in the tokamak configuration in which the compressional modes are usually neglected, as they are much higher in frequency that the shear mode. Thus the observation of the CAE modes near the shear Alfvén frequency is a novelty for fusion plasmas. Besides modes coupling and phase mixing, a new phenomenon was observed in this case, the resonance absorption, which damps any compressional mode directly coupled to the continuous spectrum of the shear Alfvén wave. Moreover, a new discrete mode was observed, called the Global Alfvén Eigenmode (GAE), just below the Alfvén continuum. In particular, by analysing multiple configuration with different peak profiles of the density, we saw that moving the peak density from the center to the wall of the cylinder the resonance absorption of the 1^{st} CAE, which was coupled to the continuum, was less and less effective. We also noted an opposite trend for the GAE, which was less and less excited moving the density peak from the center to the edge. This established that the GAE mode is more easily excited with density profiles peaked near the plasma center. The SAW damping rate due to phase mixing seemed to be independent of the density profile.

The last step was the analysis of a time-dependent mean magnetic field in a "realistic" RFP dynamical configuration, with both uniform and RFX-mod-like hollow density profiles. These simulations display a self-consistent MHD dynamics and are characterised by periodic magnetic reconnection events, also observed in real RFX-mod discharges. This part of the Thesis was crucial for the determination of the triggering mechanism of Alfvén waves in RFP plasmas. Indeed we discovered that the Alfvén waves are excite by periodic magnetic reconnection events. In fact the Alfvén activity, composed of SAW, CAE and GAE modes, show clear bursts during these events. The excitation of Alfvén modes by magnetic reconnections is another novelty in the current modeling landscape of fusion plasmas, where the emphasis is focused rather on the study of the excitation of Alfvén modes by beams of neutral atoms or α particles produced by fusion reactions in burning plasmas.

Finally we used the "realistic" simulation case for the qualitative comparison and theoretical interpretation of the experimentally observed Alfvén waves in the RFX-mod device. First we showed that the most excited Fourier harmonic in numerical simulations was $(m,n) = (1,0)$, the same dominant component of Alfvénic fluctuations in the RFX-mod device, thus confirming the similarity of the "realistic" numerical simulations compared to the RFX-mod discharges. Then, we compared the numerical spectrum from the "realistic" RFP case, with hollow density profile, with the RFX-mod one, with good resulting qualitative agreement. This allowed us to propose the identification of the experimental

coherent Alfvén modes, named d, e and f in Section 8.6, as a GAE, the 1^{st} CAE, and the 2^{nd} CAE, respectively. The theoretical interpretation of experimental Alfvénic fluctuations in RFX-mod was the original goal of this Thesis and represents a further element of originality of this research study.

In conclusion, the results achieved in this Thesis and the employed theoretical methods contribute to the understanding of the physics of Alfvén waves in fusion plasmas, in particular in the RFP configuration, and form a solid basis for future more advanced modelling studies with the inclusion of kinetic and toroidal effects, with the final goal of contributing in making magnetic confinement fusion a viable and practical solution for thermonuclear power production.

Part V

Appendices

Appendix A

Induction equation and Alfvén theorem

In this appendix we derive the induction equation. The Ampère's law (4.1c) states

$$\nabla \times \mathbf{B} = \mu_0 \mathbf{J}. \tag{A.1}$$

We can write the Ohm's law (4.1d) as

$$\mathbf{J} = \frac{1}{\eta}(\mathbf{E} + \mathbf{v} \times \mathbf{B}). \tag{A.2}$$

Combining (A.1) and (A.2) we can write the electric field as

$$\mathbf{E} = \frac{\eta}{\mu_0} \nabla \times \mathbf{B} - \mathbf{v} \times \mathbf{B}. \tag{A.3}$$

Finally substituting from (A.3) into the Faraday's law (4.1b), and using the following identity

$$\nabla \times (\nabla \times \mathbf{B}) = \nabla(\nabla \cdot \mathbf{B}) - \nabla^2 \mathbf{B}, \tag{A.4}$$

where $\nabla \cdot \mathbf{B} = 0$, we obtain the *induction equation*

$$\frac{\partial \mathbf{B}}{\partial t} = \nabla \times (\mathbf{v} \times \mathbf{B}) + \frac{\eta}{\mu_0} \nabla^2 \mathbf{B}. \tag{A.5}$$

Now we will prove the Alfvén's theorem of flux freezing. In ideal MHD limit ($\eta = 0$), we can write

$$\frac{\partial \mathbf{B}}{\partial t} = \nabla \times (\mathbf{v} \times \mathbf{B}). \tag{A.6}$$

To continue we state a more general version of *Kelvin's vorticity theorem*: if any vector field $\mathbf{Q}$ in a fluid satisfies the equation

$$\frac{\partial \mathbf{Q}}{\partial t} = \nabla \times (\mathbf{v} \times \mathbf{Q}), \tag{A.7}$$

then

$$\frac{\mathrm{d}}{\mathrm{d}t}\int_S \mathbf{Q}\cdot\mathrm{d}\mathbf{S} = 0. \tag{A.8}$$

where **S** is a surface inside the fluid. The proof of this theorem can be found in [Choudhuri, 1998, p. 67]. Since (A.6) is of (A.7) form, we can directly apply this theorem and conclude that

$$\frac{\mathrm{d}}{\mathrm{d}t}\int_S \mathbf{B}\cdot\mathrm{d}\mathbf{S} = 0, \tag{A.9}$$

where the surface integral can be thought to be over a surface made up of definite fluid elements and the Lagrangian time derivative implies that we are considering the variation in time while following the surface as the fluid elements making it are moving. Physically we can say that the magnetic fields move with the fluid, i.e. the magnetic fields are completely "frozen" in the fluid. This result is called *Alfvén's theorem of flux-freezing*. A direct consequence of this theorem is that if two fluid elements are connected by a field line, they will always remain connected by a field line in the limit of ideal MHD. The preservation of such connectivities introduce some constrains on the dynamics of the system. In particular the magnetic topologies are exactly preserved in a magnetofluid with zero electrical resistivity.

Appendix B

Fourier Transforms

Both the fluid and kinetic descriptiopns of a plasma employ the theory of Fourier transforms, which we summarize here. If the equilibrium state of the plasma is assumed uniform, and the fluid equations are linearized, the coefficients in the resulting wave equatios are constants. A Fourier transform in space and time will then yield an algebraic equation in the Fourier amplitude of, for example, the perturbation velocity $\mathbf{v}_1$, which is a function of time t and space x. The Fourier transform of $\mathbf{v}_1$ is defined as

$$\mathbf{v}(\omega, \mathbf{k}) = \int \mathrm{d}t \; \mathrm{d}^3\mathbf{x} \;\; \exp\left(i\left(\omega t - \mathbf{k}\cdot\mathbf{x}\right)\right) \mathbf{v}_1(t, \mathbf{x}) \tag{B.1}$$

with the inverse transform

$$\mathbf{v}_1(t, \mathbf{x}) = \int \frac{\mathrm{d}\omega \; \mathrm{d}^3\mathbf{k}}{(2\pi)^4} \;\; \exp(-i(\omega t - \mathbf{k}\cdot\mathbf{x}))\mathbf{v}(\omega, \mathbf{k}). \tag{B.2}$$

Taking the Fourier transform in the uniform plasma case is simply equivalent to seeking plane wave solutions, that is, to assuming the form

$$\exp[i(k_x x + k_y y + k_z z - \omega t)] \tag{B.3}$$

for the wave fields, with k_x, k_y and k_z the constant wavenumbers in a Cartesian coordinate system.

Appendix C

Visco-resistive MHD equations in dimensionless units

The equations of the visco-resistive MHD model in dimensionless form can be obtained from those in SI units:

$$\rho\left[\frac{\partial \mathbf{v}}{\partial t}+(\mathbf{v}\cdot\nabla)\mathbf{v}\right]=\mathbf{J}\times\mathbf{B}+\rho\nu\nabla^2\mathbf{v} \tag{C.1a}$$

$$\frac{\partial \mathbf{B}}{\partial t}=-\nabla\times\mathbf{E} \tag{C.1b}$$

$$\nabla\times\mathbf{B}=\mu_0\mathbf{J} \tag{C.1c}$$

$$\mathbf{E}+\mathbf{v}\times\mathbf{B}=\eta\mathbf{J} \tag{C.1d}$$

$$\nabla\cdot\mathbf{B}=0. \tag{C.1e}$$

The physical variables will be normalized to the characteristic values of the system under examination and the density will be considered constant equal to ρ_0, in particular we have:

$$r=\tilde{r}a \tag{C.2a}$$

$$t=\tilde{t}\tau_A \tag{C.2b}$$

$$\rho=\rho_0 \tag{C.2c}$$

$$\mathbf{B}=\tilde{\mathbf{B}}B_0 \tag{C.2d}$$

$$\mathbf{J}=\tilde{\mathbf{J}}J_0 \tag{C.2e}$$

$$\mathbf{v}=\tilde{\mathbf{v}}v_A, \tag{C.2f}$$

with a plasma radius in cylindrical geometry, B_0 value of the axial component of the magnetic field at the axis of the cylinder at the initial instant, $v_A=\frac{B_0}{(\mu_0\rho_0)^{1/2}}$ Alfvén's speed and $\tau_A=\frac{a}{v_A}$ Alfven's time.

From the equation (C.1c) we obtain the normalization factor for the current:

$$\tilde{\mathbf{J}}J_0\frac{\mu_0 a}{B_0}=\tilde{\nabla}\times\tilde{\mathbf{B}}\Rightarrow J_0=\frac{B_0}{\mu_0 a}. \tag{C.3}$$

From the equation (C.1a) we obtain the normalization factor for the resistivity:

$$\frac{\mathrm{d}\tilde{\mathbf{v}}}{\mathrm{d}\tilde{t}} = \frac{\tau_A}{v_A}\left(\frac{J_0 B_0}{\rho_0}\tilde{\mathbf{J}}\times\tilde{\mathbf{B}} + \frac{\nu v_A}{a^2}\tilde{\nabla}^2\tilde{\mathbf{v}}\right) = \tilde{\mathbf{J}}\times\tilde{\mathbf{B}} + \frac{\nu}{v_A a}\tilde{\nabla}^2\tilde{\mathbf{v}} \Rightarrow \tilde{\nu} = \frac{\nu}{v_A a} = \frac{1}{M}, \tag{C.4}$$

where M is the viscous Lundquist number, which represents the inverse of viscosity in dimensionless units. The analysis of the equation (C.1c) makes it possible to find the normalization factor for the electric field $\mathbf{E}$:

$$\frac{\partial\tilde{\mathbf{B}}}{\partial\tilde{t}} = \frac{E_0}{v_A B_0}\tilde{\nabla}\times\tilde{\mathbf{E}} \Rightarrow E_0 = v_A B_0. \tag{C.5}$$

Considering the Ohm equation (C.1d) instead we obtain:

$$\tilde{\mathbf{E}} + \tilde{\mathbf{v}}\times\tilde{\mathbf{B}} = \frac{\eta}{\mu_0 v_A a}\tilde{\mathbf{J}} = \tilde{\eta}\tilde{\mathbf{J}}. \tag{C.6}$$

One notices in particular the identity:

$$\tilde{\eta} = \frac{\eta}{\mu_0 v_A a} = \frac{\eta a}{\mu_0 v_A a^2} = \frac{\tau_A}{\tau_R} = S^{-1}, \tag{C.7}$$

wherein $\tau_R = \frac{\mu_0 a^2}{\eta}$ represents the resistive diffusion time and S the Lundquist number.

With these normalizations, the visco-resistive MHD equations in dimensionless units are obtained (tildas have been omitted):

$$\frac{\partial\mathbf{v}}{\partial t} + (\mathbf{v}\cdot\nabla)\mathbf{v} = \mathbf{J}\times\mathbf{B} + \nu\nabla^2\mathbf{v} \tag{C.8a}$$

$$\frac{\partial\mathbf{B}}{\partial t} = -\nabla\times(\eta\mathbf{J} - \mathbf{v}\times\mathbf{B}) \tag{C.8b}$$

$$\mathbf{J} = \nabla\times\mathbf{B} \tag{C.8c}$$

$$\nabla\cdot\mathbf{B} = 0 \tag{C.8d}$$

Note that our model equations highlights only two dimensionless parameters η and ν that matter for the dynamics of the system. In other words, once the dimensionless values of η and ν have been chosen, SpeCyl provides a solution of the visco-resistive MHD equations in dimensionless units, which can be rescaled for different choices of the normalization factors.

Bibliography

Bonfiglio, D., L. Chacón, and S. Cappello (2010). "Nonlinear three-dimensional verification of the SPECYL and PIXIE3D magnetohydrodynamics codes for fusion plasmas". In: *Physics of Plasmas* **17**.8, p. 082501.

Bonfiglio, D., M. Veranda, S. Cappello, D. F. Escande, and L. Chacón (2013). "Experimental-like Helical Self-Organization in Reversed-Field Pinch Modeling". In: *Phys. Rev. Lett.* **111** (8), p. 085002.

Cappello, S. (2004). "Bifurcation in the MHD behaviour of a self-organizing system: the reversed field pinch (RFP)". In: *Plasma Physics and Controlled Fusion* **46**.12B, B313.

Cappello, S. and D. Biskamp (1996). "Reconnection processes and scaling laws in reversed field pinch magnetohydrodynamics". In: *Nuclear Fusion* **36**.5, p. 571.

Cappello, S. and R. Paccagnella (1992). "Nonlinear plasma evolution and sustainment in the reversed field pinch". In: *Physics of Fluids B: Plasma Physics* **4**.3, pp. 611–618.

Chen, F.F. (1984). *Introduction to Plasma Physics and Controlled Fusion*. Introduction to Plasma Physics and Controlled Fusion v. 1. Springer.

Chen, Liu and Akira Hasegawa (1974). "Plasma heating by spatial resonance of Alfvén wave". In: *The Physics of Fluids* **17**.7, pp. 1399–1403.

Choudhuri, A.R. (1998). *The Physics of Fluids and Plasmas: An Introduction for Astrophysicists*. Cambridge University Press.

Cramer, N.F. (2001). *The physics of Alfvén waves*. Wiley-VCH.

Escande, D. F., R. Paccagnella, S. Cappello, C. Marchetto, and F. D'Angelo (2000a). "Chaos Healing by Separatrix Disappearance and Quasisingle Helicity States of the Reversed Field Pinch". In: *Phys. Rev. Lett.* **85** (15), pp. 3169–3172.

Escande, D. F., S. Cappello, F. D'Angelo, P. Martin, S. Ortolani, and R. Paccagnella (2000b). "Single helicity: a new paradigm for the reversed field pinch". In: *Plasma Physics and Controlled Fusion* **42**.12B, B243.

Freidberg, Jeffrey P. (2014). *Ideal MHD*. Cambridge University Press.

Goldston, R.J. and P.H. Rutherford (1995). *Introduction to Plasma Physics*. Institute of Physics Pub.

Grad, H. and H. Rubin (1958). "Hydromagnetic equilibria and force-free fields". In: *Page 190 of: Proceedings of the Second United Nations International Conference on the Peaceful Uses of Atomic Energy, United Nations, Geneva* **31**.

Lorenzini, R. et al. (2009a). "Improvement of the magnetic configuration in the reversed field pinch through successive bifurcations". In: *Physics of Plasmas* **16**.5, p. 056109.

Lorenzini, R. et al. (Aug. 2009b). "Self-organized helical equilibria as a new paradigm for ohmically heated fusion plasmas". In: *Nature Physics* **5**, pp. 570–574.

Martin, P. et al. (2003). "Overview of quasi-single helicity experiments in reversed field pinches". In: *Nuclear Fusion* **43**.12, p. 1855.

Musielak, Z. E. and S. T. Suess (1989). "MHD surface waves in high- and low-beta plasmas. Part 1. Normal-mode solutions". In: *Journal of Plasma Physics* **42**.1, 75–89.

Ortolani, S. and D.D. Schnack (1993). *Magnetohydrodynamics of Plasma Relaxation*. World Scientific.

Piovesan, P., M. Zuin, A. Alfier, D. Bonfiglio, F. Bonomo, A. Canton, S. Cappello, L. Carraro, R. Cavazzana, D.F. Escande, A. Fassina, M. Gobbin, R. Lorenzini, L. Marrelli, P. Martin, E. Martines, R. Pasqualotto, M.E. Puiatti, M. Spolaore, M. Valisa, N. Vianello, P. Zanca, and the RFX-mod Team (2009). "Magnetic order and confinement improvement in high-current regimes of RFX-mod with MHD feedback control". In: *Nuclear Fusion* **49**.8, p. 085036.

Sonato, P., G. Chitarin, P. Zaccaria, F. Gnesotto, S. Ortolani, A. Buffa, M. Bagatin, W.R. Baker, S. Dal Bello, P. Fiorentin, L. Grando, G. Marchiori, D. Marcuzzi, A. Masiello, S. Peruzzo, N. Pomaro, and G. Serianni (2003). "Machine modification for active MHD control in RFX". In: *Fusion Engineering and Design* **66-68**. 22nd Symposium on Fusion Technology, pp. 161 –168.

Spagnolo, S., M. Zuin, F. Auriemma, R. Cavazzana, E. Martines, M. Spolaore, and N. Vianello (2011). "Alfvén eigenmodes in the RFX-mod reversed-field pinch plasma". In: *Nuclear Fusion* **51**.8, p. 083038.

Villard, L. and J. Vaclavik (1997). "Alfven frequency modes and global Alfven eigenmodes". In: *Nuclear Fusion* **37**.3, p. 351.

Vlad, G., F. Zonca, and S. Briguglio (2008). "Dynamics of Alfvén waves in tokamaks". In: *La Rivista del Nuovo Cimento (1978-1999)* **22**.7, p. 1.

Wesson, J. (2004). *Tokamaks*. International series of monographs on physics. Clarendon Press.